INFORMATION TO USERS

This manuscript has been reproduced from the microfilm master. UMI films the text directly from the original or copy submitted. Thus, some thesis and dissertation copies are in typewriter face, while others may be from any type of computer printer.

The quality of this reproduction is dependent upon the quality of the copy submitted. Broken or indistinct print, colored or poor quality illustrations and photographs, print bleedthrough, substandard margins, and improper alignment can adversely affect reproduction.

In the unlikely event that the author did not send UMI a complete manuscript and there are missing pages, these will be noted. Also, if unauthorized copyright material had to be removed, a note will indicate the deletion.

Oversize materials (e.g., maps, drawings, charts) are reproduced by sectioning the original, beginning at the upper left-hand corner and continuing from left to right in equal sections with small overlaps.

Photographs included in the original manuscript have been reproduced xerographically in this copy. Higher quality 6" x 9" black and white photographic prints are available for any photographs or illustrations appearing in this copy for an additional charge. Contact UMI directly to order.

Bell & Howell Information and Learning
300 North Zeeb Road, Ann Arbor, MI 48106-1346 USA
800-521-0600

Magnetic Resonance Imaging of Cerebral Oxygen Consumption and Perfusion

RICHARD D. HOGE, M.SC.

Department of Biomedical Engineering
McGill University, Montreal

A thesis submitted to the faculty of Graduate Studies and Research in partial fulfillment of the requirements of the degree of Doctor of Philosophy

Abstract

This dissertation describes both methodological developments in quantitative functional magnetic resonance imaging (fMRI) of cerebral oxygen consumption, and the results of experiments using these techniques to elucidate the mechanisms linking focal changes in blood flow and oxygen metabolism. Technical contributions presented include a novel MRI pulse sequence for simultaneously monitoring cerebral blood flow and tissue oxygenation with high signal-to-noise ratio, as well as an experiment automation system permitting complex multiparametric studies to be carried out efficiently in large numbers of subjects. These tools enabled us to make a number of significant neurophysiological discoveries with important implications for the design and interpretation of fMRI experiments. In particular, relative changes in cerebral perfusion and oxygen consumption were found to be coupled in a consistent linear ratio of approximately 2:1, respectively, in human visual cortex. A quantitative model predicting that oxygenation-sensitive MRI signals must be extremely sensitive to departures from this coupling ratio was also introduced, revealing that combined perfusion/oxygenation measurement during graded activation is a powerful tool for studying regulatory relationships between these parameters. Predictions based on this model were in excellent agreement with experimental results, supporting model-derived estimates of oxygen consumption and suggesting that the ~2:1 coupling discovered in visual cortex is likely to apply in most cortical systems. Finally, important non-linear characteristics of fMRI signal dynamics in human visual cortex were revealed, challenging current models of fMRI transient response.

Resumé

Ce dissertation décrit des développements méthodologiques quantitatifs concernant la consommation d'oxygène cérébrale, ainsi que les résultats d'expériences utilisant ces techniques pour élucider les mécanismes reliant les changements locaux du flux sanguin au métabolisme de l'oxygène. Les contributions techniques présentées comprennent une nouvelle séquence de pulses d'imagerie par résonance magnétique (IRM) permettant de mesurer simulatément le flux sanguin cérébral et l'oxygénation des tissus avec un haut rapport signal-bruit, ainsi qu'un système automatisé d'expérimentation permettant de mener des études multi-paramétriques complexes sur un grand nombre de sujets. Ces outils nous ont permis de faire un certain nombre de découvertes neurophysiologiques significatives chargées d'importantes implications pour la conception des expériences en imagerie fonctionelle par résonance magnétique (IfRM) et l'interprétation de leur résultats. En particulier, il a été découvert que les changements relatifs dans la perfusion cérébrale et la consommation d'oxygène sont liés de facon consistante dans le cortex visuel humain par un rapport linéaire approximatif de 2:1. Un modèle quantitatif prédisant que les signaux IfRM sensibles a l'oxygénation doivent être extrêmement sensibles aux déviations par rapport à cette dépendance linéaire à également été introduit, révélant que la mesure combinée perfusion/oxygénation s'avère un puissant outil pour l'étude des relations régulatoires entre ces deux paramètres lors d'activations graduées. Les prédictions s'appuyant sur ce modèle furent en excellent accord avec les résultats expérimentaux, supportant ainsi les estimations de la consommation d'oxygène basées sur le modèle et suggérant que la relation 2:1 observée dans le cortex visuel est probablement applicable à la plupart des systèmes corticaux. Finalement, d'importantes caractéristiques non linéaires de la dynamique du signal IfRM dans le cortex visuel humain ont été mises en lumière, remettant en question les modèles actuels de la reponse IfRM transitoire.

Preface

This thesis is written in the form of publications, an option provided in Section 3 of the *McGill University Guidelines Concerning Thesis Preparation*. The following text is a mandatory excerpt:

> Candidates have the option of including, as part of the thesis, the text of one or more papers submitted or to be submitted for publication, or the clearly-duplicated text of one or more published papers. These texts must be bound as an integral part of the thesis.
>
> If this option is chosen, connecting texts that provide logical bridges between the different papers are mandatory. The thesis must be written in such a way that it is more than a collection of manuscripts; in other words, results of a series of papers must be integrated.
>
> The thesis must still conform to all other requirements of the 'Guidelines for Thesis Preparation'. The thesis must include: A table of Contents, an abstract in English and French, an introduction which clearly states the rationale and objectives of the study, a review of the literature, a final conclusion and summary, and a thorough bibliography or reference list.
>
> Additional material must be provided where appropriate (*e.g.* in appendices) and in sufficient detail to allow a clear and precise judgment to be made of the importance and originality of the research reported in the thesis.
>
> In the case of manuscripts co-authored by the candidate and others, the candidate is required to make an explicit statement in the thesis as to who contributed to such work and to what extent. Supervisors must attest to the accuracy of such statements at the doctoral oral defense. Since the task of the examiners is made more difficult in these cases, it is in the candidates interest to make perfectly clear the responsibilities of all authors of the co-authored papers.

The body of this thesis contains three journal articles of which I am the first author and which were written entirely by me. The first was submitted to *Proceedings of the National Academy of Sciences*, and the other two to the *Journal of Magnetic Resonance in Medicine* and *NeuroImage*, respectively. A fourth paper, which I also wrote in the course of my Ph.D. work, was published in the *Journal of Magnetic Resonance in Medicine* and is included as an appendix. The latter publication was excluded from the body of the thesis because its subject matter, while important in the field of functional MR brain imaging, did not fit cohesively into the theme maintained by the other articles.

The three papers included in the thesis body describe a series of multi-subject functional MRI experiments aimed at understanding the physiology of brain activation and its effects on magnetic resonance imaging signals. Each article focuses on a specific question, and includes a different sub-set of the experimental data that I acquired in the course of my Ph.D. work.

The articles are included exactly as submitted to the respective journals, with minor reformatting for consistency and clarity. All references have been collected together in a single Bibliography at the end of the dissertation, and the numbering of figures and tables has been modified to include a chapter number prefix. Chapters 4–6, which contain the articles, include prefaces to provide logical links between the papers. A separate section, entitled *Contribution to Multi-Author Papers*, outlines my role in the articles included in this thesis.

Because significant methodological development was necessary to carry out the studies described in the journal articles, a chapter has been included to describe new software and hardware that I designed and built for this research.

Acknowledgements

I would like to thank my supervisor, Dr. G. Bruce Pike, whose unfailing guidance and encouragement have made this project an enjoyable and stimulating pursuit.

My gratitude is also extended to my fellow students at the MNI and elsewhere who have helped me throughout the course of this work. I would especially like to thank John Sled, Brad Gill, Dr. Jeff Atkinson, Jennifer Campbell, Andreas Lazda, Roch Comeau, Colin Holmes, Joel Ginsburg, Sean Marrett, Patrice Munger, Sridar Narayanan, Dr. Atsushi Takahashi, Valentina Petre, Serge Dumoulin, Dr. Gareth Barnes, Manou Vafaee, Dr. Tanya Kanigan, Reza Kasrai, Michel Audet, and Mark Wolforth for their shared knowledge and inspiration. I would also like to thank Dr. Alan Evans for providing an open and stimulating environment in the McConnel Brain Imaging Centre.

The interest and help of the following members of the local neuroscience community has helped this work along greatly: Drs. Curtis Baker, Robert Hess, Ernst Meyer, Davis Reutens, Tomáš Paus, Denise Klein, Cathy Bushnell, and Gary Duncan.

The many individuals who kindly volunteered (again and again) to be subjects in my often grueling experiments must be recognized for their patience and generosity, without which this project would have been impossible. For their help in administrative and logistical matters, I thank Pina Sorrini and Belinda Preziosi. Jean-François Malouin also deserves to be thanked for keeping our heavily loaded computer network running smoothly. I am also grateful to Eric Johnstone for teaching me how to run the equipment in our machine shop, and to Pammela Rabbitz and other respiratory therapy staff their help in setting up systems for gas inhalation and physiological monitoring. Finally, I would like to thank my family and Marta Małgorzata Majdan for their encouragement during this project. Financial support provided by the Medical Research Council of Canada, the U.S. National Institute of Mental Health, FCAR (Quebec), and the Whitaker Foundation is gratefully acknowledged.

Contents

Glossary

ATP :	adenosine triphosphate
BOLD:	blood oxygenation level dependent
CBF:	cerebral brain flow
CBV:	cerebral blood volume
CMR_{glu}:	cerebral metabolic rate of glucose
CMR_{O_2}:	cerebral metabolic rate of oxygen
dHb :	deoxyhemoglobin
EPI :	echo planar imaging
FAIR :	flow alternating inversion recovery
fMRI :	functional magnetic resonance imaging
FWHM :	full width at half maximum
GHC :	graded hypercapnia
GRASE :	gradient and spin echo
GVS :	graded visual stimulation
IR :	inversion recovery
IVIM :	intra-voxel incoherent motion
LCD :	liquid crystal display
MR :	magnetic resonance
MRI :	magnetic resonance imaging
NSA :	number of signal averages
PET :	positron emission tomography
R_2^* :	transverse relaxation rate constant ($1/T_2^*$)
RARE :	rapid acquisition with relaxation enhancement
RF :	radio frequency
ROI :	region of interest
SE :	spin echo
SNR :	signal-to-noise ratio
SPECT :	single photon emission tomography
T :	Tesla
T_1 :	spin lattice relaxation time constant
T_2 :	spin-spin relaxation time constant
T_2^* :	transverse relaxation time constant ($1/R_2^*$)
TE :	echo time
TR :	repetition time
TTL :	transistor-transistor logic
V1 :	primary visual cortex

List of Figures

List of Tables

Statement of Originality

The original contributions of this thesis are:

- The development of an interleaved perfusion and oxygenation-sensitive MRI pulse sequence permitting simultaneous measurement of these quantities with high SNR.
- Derivation of a robust analytic density compensation function for spiral MRI.
- Design of hardware and software for fMRI experiment automation and stimulus generation.
- Design and construction of apparatus for subject immobilization, gas inhalation, and visual stimulus presentation during MRI scanning.
- Design of novel experimental protocols such as perfusion matching using inhaled CO_2 for isolation of metabolic effects in oxygenation-sensitive fMRI.
- Discovery of a stimulus-independent linear 2:1 CBF/CMR_{O_2} coupling relationship in human visual cortex during neuronal activation.
- Development and experimental validation of a quantitative predictive model of the BOLD/CBF relationship in human brain.
- Introduction of a novel formalism for interpreting simultaneous perfusion and oxygenation-sensitive MRI measurements in terms of iso-CMR_{O_2} contours.
- Observation that, even in experiments with constant mean luminance and equal steady-state perfusion levels, over and undershoot in the oxygenation-dependent MRI signal arising from a specific cortical region is highly stimulus-dependent.
- Finding of a perfusion over and undershoot during certain types of visual stimulation.

- Observation of highly stimulus-specific relationships describing sensitivity of oxygenation-sensitive MRI responses in V1 to the contrast of a visual pattern.
- Revelation of non-linear oxygenation-sensitive MRI signal dynamics in human V1, in which transient amplitudes are uncorrelated with steady-state responses.

Contribution to Multi-Author Papers

I am the primary author of all papers included in this dissertation, and performed over 90% of the work described in each article. This included: development of all novel theoretical concepts introduced in the various papers; design of all experimental procedures and apparatus; all data collection and analysis; and writing of all manuscripts.

All papers in the thesis body had the same author list. For the benefit of examiners, contributions of co-authors (which were the same in all papers) are listed briefly here:

- **Jeff Atkinson, M.D.** Provided assistance in physiological monitoring of subjects, medical safety aspects of hypercapnia studies, and general physiological interpretation of results.
- **Brad Gill, B.Sc.** Assisted in development of MRI pulse sequences for simultaneous monitoring of blood flow and oxygenation.
- **Gérard R. Crelier, Ph.D.** Assisted in general development of perfusion-sensitive MRI pulse sequences.
- **Sean Marrett, M.Sc.** Assistance and advice on stimulus design and physiological interpretation of results.
- **G. Bruce Pike, Ph.D.** Overall supervision of Ph.D. project.

I was also the primary author of a fourth paper, included as an appendix to the thesis, that describes image reconstruction filters and associated theory that I derived for spiral magnetic resonance imaging. This manuscript was also written entirely by me. Remi Kwan, the second author, wrote some of the software that I used for numerical simulations included in the study. The third and senior author was G. Bruce Pike, the supervisor of the project.

Other Publications

The following are additional peer-reviewed contributions that arose from the work described in this dissertation:

Journal Papers:

- Gérard R. Crelier, Richard D. Hoge, Patrice Munger, and G. Bruce Pike. Perfusion-based functional magnetic resonance imaging with single-shot RARE and GRASE acquisitions. Magnetic Resonance in Medicine, *in press*, 1998.

- Colin J. Holmes, Richard Hoge, Louis Collins, Roger Woods, Arthur W. Toga, and Alan C. Evans. Enhancement of magnetic resonance images using registration for signal averaging. Journal of Computer Assisted Tomography, 22(2):324-333, 1998.

Conference Abstracts:

- Richard D. Hoge, Brad Gill, Jeff D. Atkinson, Gérard R. Crelier, Sean Marrett, and G. Bruce Pike. Investigation of $CMRO_2$/CBF coupling in human V1 using fMRI. In Proceedings of the Fourth International Conference on Functional Mapping of the Human Brain, p. 262, 1998.

- Jeff D. Atkinson, Richard D. Hoge, Abas F. Sadikot, and G. Bruce Pike. FMRI Demonstration of Laterality of Supplementary Motor Area and Deep Nuclear Activation in Subjects of Different Handedness. In Proceedings of the Fourth International Conference on Functional Mapping of the Human Brain, p. 958, 1998.

- Pascal Belin, Robert J. Zatorre, Richard D. Hoge, G. Bruce Pike, and Alan C. Evans. Event-related fMRI of the auditory cortex. In Proceedings of the Fourth International Conference on Functional Mapping of the Human Brain, p. 369, 1998.

- Gérard R. Crelier, Brad Gill, Richard D. Hoge, Patrice Munger, A. Valavanis, and G. Bruce Pike. Perfusion-based functional magnetic resonance imaging without magnetic susceptibility artifacts. In Proceedings of the Fourth International Conference on Functional Mapping of the Human Brain, p. 531, 1998.

- Richard D. Hoge, Brad Gill, Gérard R. Crelier, and G. Bruce Pike. Comparison of Perfusion and BOLD Responses in Human Visual Cortex to Blob-Selective Stimuli, Inter-Blob-Selective Stimuli, and Hypercapnia. In Proceedings of the 5th Annual Meeting of the International Society of Magnetic Resonance in Medicine, p. 1537, 1998.

- Gérard R. Crelier, Brad Gill, Richard D. Hoge, Patrice Munger, and G. Bruce Pike. Perfusion-Based Functional Magnetic Resonance Imaging with Single-Shot GRASE Acquisitions. In Proceedings of the 5th Annual Meeting of the International Society of Magnetic Resonance in Medicine, p. 1470, 1998.

- Richard D. Hoge, G. R. Crelier, Manouchehr Vafaee, Ernst Meyer, Sean Marrett, A.C. Evans, and G. Bruce Pike. Frequency-Dependent Changes in Oxidative Metabolism in Human Striate Cortex: Implications for BOLD fMRI. in Proceedings of the Third International Conference on Functional Mapping of the Human Brain, p. S363, 1998.

- Richard D. Hoge, Remi K.S. Kwan, Gérard R. Crelier, and G. Bruce Pike. Density Compensation Functions for Non-Ideal Spirals. In Proceedings of the 4th Annual Meeting of the International Society of Magnetic Resonance in Medicine, p. 2006, 1997.

- Gérard R. Crelier, Richard D. Hoge, and G. Bruce Pike. Quantitative Relative Perfusion Measurement Using an Inversion Recovery Fast Spin Echo Arterial Water Labeling Technique. In Proceedings of the 4th Annual Meeting of the International Society of Magnetic

Resonance in Medicine, p. 374, 1997.

- T. Paus, G. Leonard, M. Wolforth, R. Visca, R. Comeau, R. Hoge, B. Pike, T. Peters, C.J. Thompson, A.C. Evans. Cortico-cerebellar connectivity revealed by transcranial magnetic stimulation of the human motor cortex during positron emission tomography. In Proceedings of the Society for Neuroscience, p. 1276, 1997.

- Richard D. Hoge and G. Bruce Pike. Whole Brain BOLD FMRI with reduced inflow sensitivity using interleaved 3D acquisitions. In Proceedings of the Second International Conference on Functional Mapping of the Human Brain, p. S27, 1996.

- Colin J. Holmes, Richard D. Hoge, Louis Collins, and Alan C. Evans. Enhancement of T1 MR images using registration for signal averaging. In Proceedings of the Second International Conference on Functional Mapping of the Human Brain, p. S28, 1996.

- Colin J. Holmes, Richard D. Hoge, Roger P. Woods, Alan C. Evans, and Arthur W. Toga. Enhancement of T2 and proton density MR images using registration for signal averaging. In Proceedings of the Second International Conference on Functional Mapping of the Human Brain, p. S29, 1996.

- R.D. Hoge, R. Kwan, and G.B. Pike. Density compensation functions for Fourier inversion of data sampled along interleaved spiral trajectories. In Proceedings of the 4th Annual Meeting of the International Society of Magnetic Resonance in Medicine, p. 358, 1996.

- R.D. Hoge, M. Wolforth, A.C. Evans, and G.B. Pike. Acquisition and processing strategies for fMRI. In Proceedings of the 41st Annual Meeting of the Canadian Organization of Medical Physicists, p. 95, 1995.

Chapter 1: Introduction

The functional magnetic resonance imaging (fMRI) techniques most commonly employed for brain activation studies detect blood oxygenation level dependent (BOLD) changes in cortical tissue signals. These methods are based on the hypothesis that neuronal activation is associated with a significant increase in tissue perfusion with much smaller changes in the amount of oxygen extracted from the blood. Initial positron emission tomography (PET) studies of a small number of specific brain systems yielded results consistent with this model [1], but the extent to which such behavior is ubiquitous in human cerebral cortex has not been thoroughly investigated. Indeed, more recent PET results from our center suggest that the postulated decoupling between perfusion and oxygen utilization does not occur under all activation conditions [2, 3]. However, the detailed and repeated study of subjects using PET is complicated by radiation dose limits as well as limited temporal and spatial resolution.

The specific aims of this thesis were therefore:

1. to establish the necessary methodology to simultaneously and continuously measure cerebral perfusion and BOLD signals during controlled stimulation of human subjects.
2. to combine these data with calibration measurements and a biophysical model to calculate cerebral oxygen uptake and to compare these measurements to ones made using PET.
3. to assess the stimulus-dependence and dynamic aspects of cerebral oxygen consumption and blood flow coupling within human visual cortex.

Chapter 2: Literature Review

Functional MRI

Since its inception in the early 1970's [4] MRI has evolved to be the modality of choice for neuroradiological examination due to its superb soft tissue contrast and exquisite anatomical detail. While dominant in the anatomical arena, MRI has only recently been exploited to image brain function. That information has traditionally been obtained using radioactive tracer techniques, such as positron emission tomography (PET), to measure changes in cerebral blood flow (CBF) in response to functional activations. However, the past five years have witnessed the birth of functional MRI (fMRI) which now holds the promise of advancing functional imaging as it has anatomical.

fMRI does not image brain activity directly but is based on the detection of changes in various physiological correlates of neuronal activation. To date these include cerebral blood volume, flow and oxygenation. The first human fMRI brain maps were obtained by Belliveau *et al.* in 1991 [5] using a cerebral blood volume technique. Their approach consisted of the rapid imaging of the passage through the brain, during resting and activated states, of a bolus of paramagnetic contrast agent (gadolinium-DTPA) using T2 or T2* weighted acquisitions [5–7]. The major shortcomings of this fMRI technique are the poor temporal resolution and the requirement for an exogenous

contrast agent, which limits the number of functional measurements that can be performed.

To be useful for fMRI, blood flow needs to be measured at the microvascular scale (perfusion) since macrovascular flow changes can be quite remote from the activated region [8]. LeBihan *et al.* pioneered one approach to imaging perfusion using an intravoxel incoherent motion (IVIM) technique [9–13] that models capillary flow as a rapid diffusion process. Practically, however, the motion of other tissue and cerebrospinal fluid severely contaminates perfusion measurements and the technique has been shown to require unachievably high signal-to-noise ratios (SNR) [14]. The more promising approach to perfusion imaging is via the detection of magnetically labeled (saturated or inverted) arterial water spins that have been tagged upstream and allowed to flow into the region of interest and exchange with tissue water [15, 16]. The first application of this approach to detect activation induced flow changes was by Kwong *et al.* who used an inversion pulse in the imaging plane to effectively tag in-flowing blood as fully relaxed magnetization [17]. Notable variations on this method include EPI-STAR (echo planar imaging with signal targeting and alternating RF) [18], PICORE (proximal inversion with a control for off-resonance effects) [19], QUIPPS (quantitative imaging of perfusion with a single subtraction) [20], and FAIR (flow alternating inversion recovery) [21].

The third and most widely employed method of fMRI, introduced by Ogawa *et al.* [22–25], detects blood oxygenation level dependent (BOLD) signal changes secondary to neuronal activation. The physical basis of this technique is that the magnetic susceptibility of blood is a function of oxygen saturation [26–28]. Thus, T2* weighted imaging, which is very sensitive to magnetic susceptibility variations, provides a direct window on blood oxygenation. The physiological mechanism for BOLD contrast is not fully understood but is generally believed to be the result of activation-induced CBF changes significantly exceeding increases in oxygen extraction [29, 30], thereby resulting in a decrease in paramagnetic deoxyhemoglobin and an increase in T2* weighted

signal intensity. The primary reasons for BOLD's popularity over perfusion based fMRI, despite unclear mechanisms, is its greater sensitivity and ability to acquire a large number of slices. While the first reported applications of BOLD fMRI were in the primary visual [17, 25] and motor cortex [17, 31], the technique has since been demonstrated in wide range of applications including word generation, mental imagery, speech perception, and working memory (see [32–36] for reviews).

Functional Activation Physiology

Increasing the electrical activity of neurons raises the burden of ATP-dependent ion pumps found on the neuronal cell membrane, resulting in a greater demand for glucose and oxygen, the basic substrates of ATP production in brain. This increase in demand is met through acceleration of tissue perfusion rates [37–39].

The relationship between perfusion and brain electrical activity has formed the basis for brain activation studies using PET and SPECT (single photon emission computed tomography), in which a radioactive tracer is introduced into the arterial blood and tomographic imaging performed to determine the distribution of the tracer in brain tissue during rest and activation. Different labeled compounds may be used to directly measure regional CBF, CBV (cerebral blood volume), and the cerebral metabolic rates of glucose and O_2 consumption (CMR_{glu} and CMR_{O_2}).

Under baseline steady-state conditions, measurements of CBF, CMR_{O_2} and CMR_{glu} are related in a manner that suggests the almost complete oxidative metabolism of glucose [40]. However, the extent to which focal increases in ATP demand are met through oxidative versus anaerobic metabolism of glucose, an issue of critical relevance in the emerging field of fMRI, has been the subject of considerable debate. A number of studies carried out on both humans and other mammals have generally supported one of two competing views: 1) the 'decoupling' hypothesis, which

proposes that increased energy requirements during transient focal activation are met anaerobically and that CMR_{O_2} therefore does not increase significantly in spite of large increases in CBF; and 2) the 'coupling' hypothesis, which postulates that even brief surges in energy demand are met aerobically, leading to increases in both CMR_{O_2} and CBF, although the relative magnitudes of the changes may differ.

The decoupling hypothesis has been supported by PET studies of the response to vibrotactile and visual stimulation [29, 30], and is consistent with reported observations of activation-induced lactate increases during visual stimulation [41], and fMRI observations of decreases in brain deoxyhemoglobin concentration (the BOLD effect) during presentation of a variety of stimuli [42, 43]. The coupling hypothesis, on the other hand, has been supported by PET studies of mental imagery [44] and the response to more complex visual patterns [45, 46], optical imaging studies of visual activation [47], ^{13}C NMR studies of aerobic pathway activity during electrical fore-paw stimulation in rats [48], and is consistent with recently developed theoretical models of oxygen delivery [49]. It is also not inconsistent with the BOLD effect in general and is supported by short-lived increases in tissue deoxyhemoglobin concentration immediately following the onset of activation (*i.e.* negative BOLD effect) [50] and extrapolated comparisons between BOLD signal increases induced by hypercapnia and neuronal activation [51].

Given the divergence of the results, and the fact that the different techniques used in the above studies have been indirect and based on sometimes questionable assumptions, the possibility of method-specific inaccuracies systematically exaggerating or underestimating CMR_{O_2} changes can not be ruled out. Another possibility is that both scenarios occur in the brain, with the balance between aerobic and anaerobic glycolysis depending on the metabolic characteristics of the tissues that are being stimulated. There is considerable anatomical and biochemical evidence for such heterogeneity in the mammalian brain, including regional variations in vascular anatomy, mito-

chondrial density, and in the activity of various metabolic enzymes such as cytochrome oxidase and lactate dehydrogenase [52–59].

Enzymatic Heterogeneity in Primary Visual Cortex

The investigation of stimulus-specific CBF/CMR_{O_2} coupling described in this thesis focuses on the so-called *blob* and *inter-blob* systems in primary visual cortex (V1). These tissue domains are good candidates for this study due to biochemical evidence of different capacities for anaerobic and aerobic metabolism [52, 54, 55], profound and well characterized differences in their response characteristics under visual stimulation [60, 61], and their confinement to a specific and identifiable region of the cortex [52].

The blobs are columnar regions, occurring only in primary visual cortex of human and non-human primates, about 0.4 mm in diameter spaced 0.5 mm apart [52]. Studies using histochemical staining techniques have shown that these regions contain significantly higher levels of the enzyme cytochrome oxidase than the intervening (inter-blob) areas (Fig. 2.1a). Staining for the glycolytic (anaerobic) enzyme lactate dehydrogenase is only slightly enhanced in the blob regions [52], suggesting differential rates of anaerobic and aerobic metabolism in the two groups of cells.

In spite of this enzymatic heterogeneity, autoradiographic studies of primary visual cortex in the macaque monkey [60, 61] have demonstrated clearly that, during baseline conditions (e.g. presentation of a spatially uniform and temporally constant grey field), uptake of the radioactively labeled glucose analog ^{14}C-2-deoxyglucose (DG) occurs uniformly throughout the visual cortex (Fig. 2.1b). These studies have also shown that it is possible to selectively stimulate either the blob or inter-blob regions, raising DG uptake in the target areas significantly above baseline levels (Fig. 2.1c). In the monkey studies cited above, highly blob-specific activation was produced

Figure 2.1: a) Cytochrome oxidase staining in primary visual cortex of a macaque monkey, showing blobs (dark areas); b) Deoxyglucose (DG) autoradiograph of monkey visual cortex, showing uniform DG uptake in unstimulated area (light) and increased but homogeneous accumulation in the adjacent region activated using a non-specific visual pattern; c) DG autoradiograph showing localized uptake in blob regions evoked by a spatially diffuse chromatic stimulus (from [61]). Regions shown represent $\sim$1 cm^2 of cortex, corresponding to four (2x2) voxels of the fMRI acquisitions used in all experiments.

by presenting low-spatial-frequency chromatic patterns to the animals, while inter-blob-specific stimulation was achieved using very high spatial frequency black and white gratings that were systematically varied in orientation. Although these studies were done in macaques, there is considerable psychophysical evidence in humans suggesting that the same segregation of color and spatial frequency information occurs, in a fashion that is remarkably consistent with the anatomy and physiology observed in non-human primates [52, 53, 62–64].

The blob/inter-blob matrix occurs on a scale that is too small to be resolved by functional MR imaging. The net image signal observed in V1 is the additive sum of the contributions from the blob and inter-blob regions, however, and a change in the relative activity levels of the two tissue domains should produce a measurable variation in the BOLD signal observed at a given perfusion level if there is indeed a shift between aerobic and anaerobic metabolism. Although there is no way to verify that the stimuli described above selectively activate blob or inter-blob regions in humans, the two types of stimulus constitute profoundly different types of visual information and, based on

current knowledge of primate and human vision, they appear to be the best available candidates for variably biasing activation towards tissues of high mitochondrial activity.

fMRI Signal Dynamics

Temporal characteristics of the BOLD signal have attracted considerable interest recently, due to their physiological importance and implications for experimental design in fMRI. Several early studies suggested that the BOLD response was a transient phenomenon. Hathout *et al.* found that visually-evoked BOLD responses decayed back to baseline within approximately ten minutes [65], while Frahm *et al.* noted an even more rapid decline within three minutes [66]. If such behavior, especially the more rapid decline observed by Frahm, were pervasive in human cortex, it would imply important limitations for experimental design in fMRI. In particular, protocols seeking to detect steady-state changes in neuronal activation would be ruled out.

Fortunately, subsequent studies have demonstrated that increases in neuronal activity produce positive changes in the steady-state BOLD signal that can be sustained for arbitrarily long periods [67–70]. While this finding supports experimental design based on detection of steady-state changes, current 'event-related' fMRI techniques [71] require a detailed understanding of dynamic aspects of the BOLD signal.

Two transient features are commonly observed in activation-induced BOLD responses: a large, positive post-onset overshoot and a post-cessation negative undershoot of similar amplitude. Both events are followed by an exponential-like decay to a new steady-state level within approximately one minute. A small and brief ($\sim$1s) negative dip immediately following onset of stimulation is also occasionally observed [50, 72, 73], but this feature is much less prominent. All of these responses have attracted intense interest as evidence for various physiological phenomena, and

several biophysical models incorporating them have recently been introduced. These theories are generally based on temporal lag between perfusion adjustment (which is assumed to occur within several seconds) and the more gradual onset of attenuating responses such as increased oxygen consumption [66, 74] and/or blood volume [75, 76].

The role of blood volume has emerged as a particularly likely candidate for a source of delayed attenuation, due to observations of a surprisingly gradual onset of blood volume increases. In a recent paper, Mandeville *et al.* describe the temporal evolution of CBV as a rapid elastic response of capillaries and veins followed by a slow venous stress relaxation, which they suggest corresponds to the slow phase of CBV increase that they observe with a time constant of approximately 14 seconds [76]. This model, termed the windkessel model, incorporates information about the resistive properties of brain vasculature and the capacitive behavior of capillaries and veins (the windkessel was a leather bag connected to firehoses in 19th century Germany to smooth pulsatile water flow, a term adopted by Otto Frank to describe vascular capacitance [77–79]).

Buxton *et al.* have proposed a more general model, based solely on conservation of mass, to describe changes in blood volume in terms of the difference between arterial and venous flux of blood [75]. This model is also consistent with over and undershoots in the BOLD fMRI signal.

The *linearity* of the BOLD response has been examined in a number of recent studies. Boynton *et al.* found that an empirically measured impulse response function could be used to predict the signal produced by longer stimulation intervals with reasonable accuracy, and that the response functions evoked by presenting a particular visual stimulus at different contrast levels were scaled copies of one another [80]. This is an important claim because, if it is correct, BOLD signal time-courses could be predicted based only on knowledge of the impulse response function and the waveform describing variations in experimental input parameters over time. Linearity would also simplify extraction of specific components from fMRI signals containing superimposed responses,

a capability that is essential for recently proposed 'event-related' fMRI techniques.

In event-related fMRI [71, 81–86], brief stimuli are repeatedly presented at random intervals. The event-related response is isolated by computing the average signal over some constant interval following every time point containing an event. The effects of overlapping responses are removed by computing the average of signal intervals following all non-event time segments, which contain a similar distribution of overlapping events, and subtracting this from the event-locked average. It is generally desired that the event-related response recovered in this way be identical to the response that would have been observed in a much longer experiment with no overlap. This is only the case when the responses behave linearly, however, and this has only been verified under a restricted range of conditions. Furthermore, such approaches constitute a major departure from the steady-state experimental paradigms traditionally used for human brain mapping with modalities such as PET, and relationships between transient and steady-state responses have not been extensively studied. Nevertheless, application of event-related averaging methods to fMRI has the potential to revolutionize experimental design with this modality and it appears likely that, in spite of the cautionary statements made above regarding linearity, the technique will prove useful in a wide variety of areas.

Chapter 3: Methodological Development

MRI Measurement of CBF and CMR_{O_2}

An important requirement of this project was the need to achieve simultaneous, dynamic monitoring of cerebral blood flow and oxygenation *in vivo* using MRI. To do so, the interleaved BOLD and perfusion sequence illustrated in Figure 3.2 was developed. The BOLD acquisitions were based on a gradient echo (GE) EPI data acquisition window in which the TE (echo time from excitation) was ~50 ms. This sequence, which is sensitive to changes in blood oxygenation, [87, 88], was used to acquire a single slice in a 3 s TR (repetition time). A 64×64 acquisition matrix was used with a 320×320 mm field-of-view to produce a nominal in-plane resolution of 5 mm. The data acquisition duration (EPI readout window) for these parameters was ~30 ms. To avoid EPI chemical shift artifacts each slice-selective excitation was preceded by a fat saturation pulse (not shown in Fig. 3.2).

Every second repetition consisted of an IR (inversion recovery) sequence, constituting one half of a FAIR measurement [21], with an inversion time (TI) of ~1 s, selected to simultaneously optimize signal strength and microvascular specificity [16, 17]. Spin inversion was achieved using a 10.24 ms hyperbolic secant pulse [89] with (the first block in Fig. 3.2) and without (the third block) a slice selection gradient. This gradient was adjusted to invert a region extending beyond

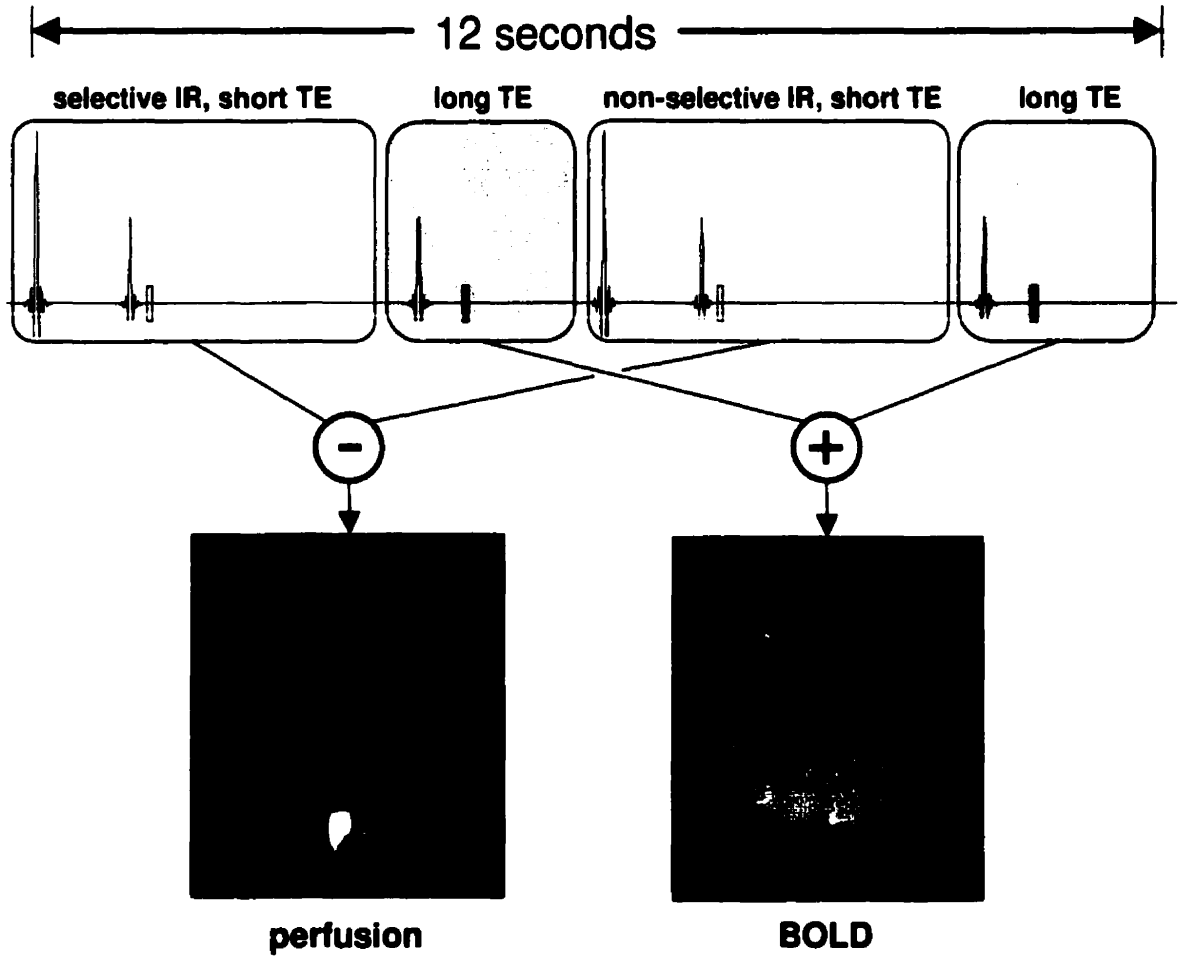

Figure 3.2: Interleaved gradient echo BOLD and FAIR sequence. This sequence was used to provide simultaneous and continuous monitoring of blood flow and oxygenation.

the bounds of the imaging slices by approximately 25% on each side. This setting minimized signal differences between the selective and non-selective IR images due to non-ideal inversion slice profiles. An EPI readout identical to that used in the BOLD repetitions was used, but the echo time was decreased to 20 ms in order to increase signal-to-noise ratio and minimize BOLD effects. The FAIR labelling scheme was selected because it does not require designation of proximal and distal sides of the imaging slice, which would have been difficult given the slice geometry used (oblique axial through the calcarine sulcus).

Images of relative CBF were calculated by subtracting each non-selective inversion image from the preceding selective inversion one. The intervening non-inversion-recovery images were added in a pairwise fashion to produce a corresponding series of BOLD images. The use of identical EPI readouts in the BOLD and FAIR images ensured that both modalities were in precise spatial register with one another, in spite of distortions and variations in point-spread function which can occur in echo-planar imaging. Previous schemes for the simultaneous acquisition of CBF and blood oxygenation information have used images from the non-selective phase of long TE FAIR sequences to provide a BOLD signal [19, 51]. The new sequence described here offers a significant gain in signal-to-noise ratio, however, due to the lack of an inversion prepulse preceding the BOLD acquisitions, and the use of a minimal echo-time in the FAIR phases. BOLD contamination of FAIR data and inflow effects in BOLD images, assessed by examination of non-selective IR images (Fig. 3.3) and comparison of BOLD images following selective vs. non-selective IR acquisitions (Fig. 3.4), were found to be slight. BOLD contamination of the short-TE IR acquisitions was not detectable above noise, while the inflow contribution to the BOLD signal at maximal perfusion levels was less than 0.1%.

Parallel projects to develop multi-slice versions of this sequence with asymmetric spin-echo readouts for the BOLD phases and single-shot RARE, GRASE, and spiral readouts for FAIR imag-

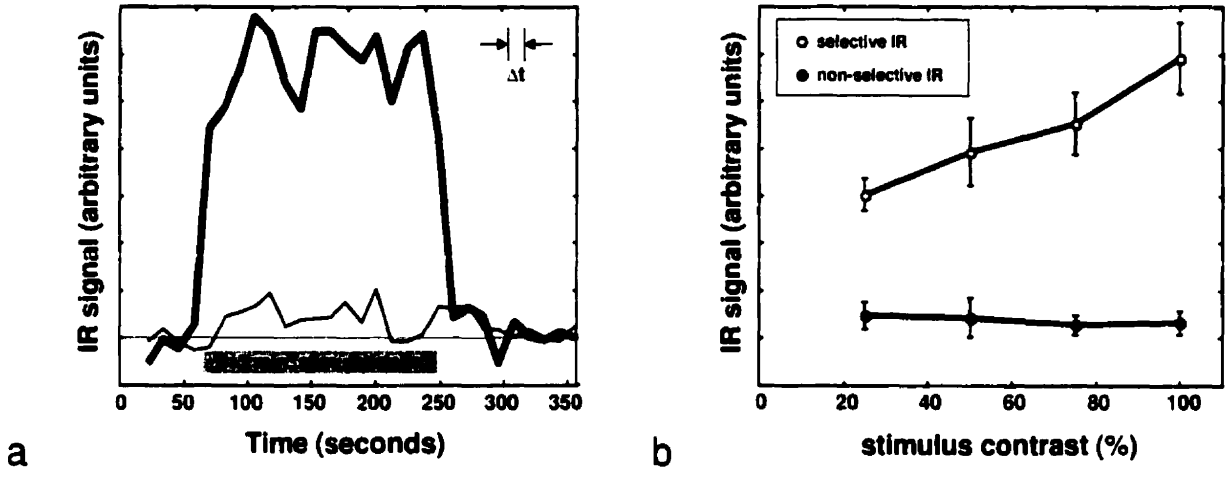

Figure 3.3: Assessment of BOLD contamination in perfusion data. (a) Time-course data in V1 from selective (heavy line) and non-selective (thin line) inversion recovery acquisition during three minutes of radial checkerboard stimulation (single subject, NSA=6). BOLD contributions, which are isolated in the non-selective signal, are negligible compared to the inflow component. (b) Response as a function of stimulus contrast for selective and non-selective IR signals. The flow-sensitive response is seen to decrease at lower contrast levels, while the non-selective signal does not change significantly with contrast. Temporal sampling interval, Δt, is indicated in (a).

ing [90, 91] were also in progress during this work, and these enhancements will be incorporated as they become available. The objectives of this dissertation were met with the basic single slice gradient-echo EPI version of the sequence, however, so the studies proceeded with the basic implementation described above. As part of this pulse sequence development initiative, I wrote a paper on density compensation functions for spiral MRI [91], included in reprint form in Appendix A of this dissertation.

To convert BOLD and perfusion data, acquired with the interleaved sequences described above, into measures of CMR_{O_2}, a biophysical model of cerebral blood flow, volume, deoxyhemoglobin concentration and T_2^* relaxation was combined with a hypercapnia calibration methodology based

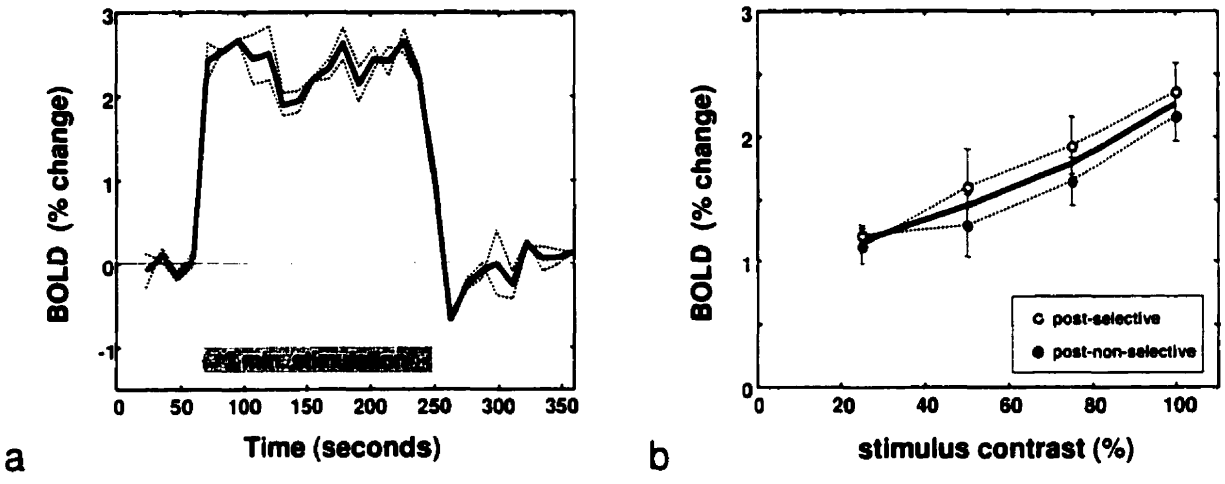

Figure 3.4: Assessment of inflow contamination in BOLD data (signals shown here were acquired simultaneously with data in Fig. 3.3). (a) Time-course data in V1 from individual BOLD acquisitions performed 4 seconds after selective or non-selective inversion prepulses (thin dotted lines), with average signal used in physiology studies (heavy solid line). The BOLD signal measured after the non-selective IR pulse is slightly attenuated, due to incomplete recovery of flowing spins inverted throughout the head. The difference between the two dotted lines, which is small relative to the total response, represents an upper bound on inflow contamination. (b) Response as a function of stimulus contrast for BOLD signals measured following selective and non-selective IR prepulses, with average signal (heavy line). Inflow contamination does not significantly change the average contrast sensitivity function.

partly on the methods of Davis *et al.* [51]. The hypercapnic calibration protocol (described in detail in Chapter 5) usually consisted of a series of 6 minute experiments during which a baseline functional condition was maintained during graded hypercapnia and interleaved BOLD and perfusion measurements acquired using the methods outlined above.

Apparatus and Software

Another important body of methodological development that was needed to carry out the physiology experiments described in the following chapters involved the design and implementation of apparatus and software. An additional contribution of this thesis was the development of the implements described below:

- **Visual stimulation:** Flexible software for the generation of visual stimuli and control and logging of randomized parametric psychophysical experiments, in synchronization with dynamic fMRI data acquisition, was developed. The program, called *GLstim*, was implemented in C/OpenGL on a Silicon Graphics O_2 workstation. The software is intended to be portable across multiple platforms and operating systems, including SGI/Unix, PC/Linux, and PC/Windows NT. The system includes a scripting language which permits flexible specification of experimental paradigms using a simple syntax. Complicated randomization schedules, including 'single-trial' type protocols, can be generated. These are automatically executed upon receipt of synchronization information (TTL trigger pulses) from the scanner. Detailed logging of experiments is performed, and the implementation provides robust backup measures for recovery from interruptions of experimental schedules which can occur. The stimulus generation software is capable of producing sine and square-wave gratings, drifting or stationary, of constant or variable orientation, uniform fields, square and radial checkerboard patterns (Fig. 3.6), text strings, bitmap images from user-supplied GIF files, and patterns for phase-encoded retinotopic mapping. Independent temporal modulation of red, green, and blue components of these patterns with sinusoidal and square waveforms with rendering at the screen refresh rate of 60 Hz is supported. Psychophysical calibration procedures, such as flicker photometry for determination of isoluminance, can be performed

using input from the subject while in the scanner via MR-compatible feedback hardware.

A hardware interface for synchronization of the system with the scanner was also constructed. The device connects to the stimulus delivery computer via a standard PC mouse interface, allowing stimulus delivery software to be tested and debugged using a commonly available PC mouse rather than specialized serial port hardware. This was intended to simplify development of stimulus presentation software by the many researchers from outside laboratories who collaborate with our MRI group and need to synchronize their experiments with data acquisition.

Optics for stimulus delivery consist of a mirror built into a special head immobilization device (Fig. 3.5b) using a novel geometry in which an LCD device is used to project the video display onto a screen placed directly above the subjects head (other centres have projected over the subject's body). This arrangement provides an exceptionally large field of view (up to $\sim 35°$) without requiring expensive collimating optics. The use of a Unix workstation, which can be remotely controlled via internet, allows the computer to be placed as close as possible to the LCD projector while operating and monitoring the stimulus control software from the MRI control room, minimizing problems due to interference and cable capacitance. The display system is MRI compatible and can be transferred to the PET scanner suite in order to exactly replicate visual stimulation conditions for PET/fMRI cross-validation studies.

- **V1 ROI mask generation:** Phase-encoded retinotopic mapping procedures, adapted from [92], were used to delineate primary visual cortex on interleaved BOLD/CBF image pairs. In separate, preliminary sessions, cyclically dilating or rotating stimuli (Fig. 3.7a,c) were presented to subjects and Fourier analysis performed on the time varying signal in each image voxel in multi-slice BOLD acquisitions. The phase values of the Fourier transform

at the dilation/rotation frequency provided information about the retinal projection of voxels in visual cortex (Fig. 3.7b,d), while the magnitude yielded extremely high SNR maps of retinotopically organized areas in all subjects (Fig. 3.8). The V1 masks were resampled onto the voxel grids used in subsequent experiments according to the computed transformation required to align high resolution anatomic images acquired at the beginning of each session [93]. Primary visual cortex was defined as being the retinotopically organized region within the left or right calcarine sulcus containing a mirror-image representation of the contralateral visual hemifield. The ability to automatically register and resample the 3D masks onto the 2D slice data acquired in later sessions meant the retinotopic mapping procedure only had to be performed once per subject.

- **Subject attention monitoring:** Many of the fMRI studies in this project were of relatively long duration ($\sim$2 hours). In pilot studies it was not uncommon for subjects to experience problems attending to stimuli and even fall asleep during protracted sessions. Because it is difficult to observe subjects directly while they are inside of the scanner, it was necessary to monitor constantly some form of feedback from them to ensure that they were awake, alert, and were fixating on the appropriate region of visual stimulation patterns. To meet this need, MRI compatible (*i.e.* non-magnetic) hardware for subject feedback registration was constructed (G in Fig. 3.5a), and interfaced with the stimulus delivery system in conjunction with a simple attention task that was incorporated into all experiments. Subjects were required to continually report the (randomly varied) left-right orientation of a triangular fixation marker during both baseline and activation conditions, in order to ensure alert fixation at all times while excluding activation associated with this task from stimulation/baseline comparisons.

  Use of this system revealed that during long studies, subjects frequently fall asleep. The

ability to detect this and intervene helped prevent loss of data. Subjects reported that this scheme greatly aids in maintaining alertness and gaze stability. Nystagmus associated with presentation of stimuli at low temporal modulation frequencies was greatly reduced (based on subjective reports).

- **Gas delivery:** A system for the delivery of either medical air or graded mixtures of 5:21:74 percent CO_2:O_2:N_2 and medical air to subjects while they are inside the MRI scanner was constructed and tested in over 40 experimental sessions. Switching is performed manually, but an automatic prompting system was implemented using the stimulus delivery system, in order to facilitate changing gas supplies at the appropriate point during fMRI studies. Highly reproducible elevations of end-tidal CO_2 (see below) were achieved, producing consistent increases in CBF. Concentration of CO_2 was controlled by combining the pre-mixed CO_2/air preparation with medical air in a Y-connector and adjusting respective flow rates to achieve the desired proportions while maintaining a constant total flow rate.

- **Physiological monitoring:** During hypercapnia studies it was of interest to monitor physiological parameters such as end-tidal CO_2, pulse rate, arterial O_2 saturation, blood pressure, and respiratory rate. MRI compatible facilities for doing this were assembled using equipment obtained from the department of anesthesiology at the MNI. In hypercapnia experiments, a double lumen nasal cannula (Baxter Healthcare Corporation) was fitted beneath the gas delivery mask, and one lumen connected to an end tidal CO_2 ($ETCO_2$) monitoring aspirator (Normocap 200, Datex Inc., Helsinki). This device provided continuous $ETCO_2$ measurements, as an approximate measure of P_{CO_2}, as well as a continuous respiratory rate monitor. In addition, a percutaneous infrared oxygen saturation monitor (Oxygen/Pulse Monitor, Nonin Medical Inc., Minneapolis) was used to provide continuous heart rate and

oxygen saturation readings. Finally, an automated blood pressure cuff (Dinamap Vital Signs Monitor 8100, Critikos, Tampa) was available to provide blood pressure readings at 2 minute intervals throughout the experiment.

- **Head immobilization:** Because of the long duration of the studies in this project and fMRI's extreme sensitivity to motion, an apparatus for head immobilization that is highly rigid yet comfortable was required. It was also necessary to accommodate gas masks worn by subjects during hypercapnia studies, without interfering with the presentation of visual stimuli with a wide field of view. A system providing very firm but comfortable head immobilization was designed and constructed from magnetically compatible materials (Fig. 3.5b). A subject's head and neck receive distributed support from a contoured foam head rest that is securely mounted on an assembly incorporating a quadrature receive-only surface coil for reception of MRI signals. Lateral head movements are restricted by rigidly mounted, padded, hearing protection cups which can be pressed very firmly against the head without discomfort. Pitch and yaw-type movements are prevented through the use of a hard plastic nose-bridge that is machined into a saddle-shape and pressed firmly down over the bridge of the nose to provide effective immobilization with minimal irritation.

  The assembly also includes a large mirror held above the subjects face for presentation of visual stimuli. The height and angulation of the mirror can be adjusted for different viewing conditions and to accommodate gas-masks worn during hypercapnia studies. Rigid plexiglas 'bite-bars' supporting molded dental impressions, offering highly effective immobilization, can be mounted on the apparatus, although this means of restricting movement is not available during gas inhalation studies. The bite bars developed for this system employ a very strong but simple one-piece construction which improves safety by reducing the risk of breakage and eliminating the need for re-use and attendant sterilization problems that existed

with more elaborate and therefore expensive designs. Before this apparatus was introduced, subject discomfort and head/neck pain during long studies was a serious and common problem, and the degree of immobilization provided by the original manufacturers head rest was unsatisfactory. The new assembly has been tested on over 50 individuals, including volunteers and patients, without mishap, and complaints of discomfort and problems with subject movement have been greatly reduced. A modified version for use with the Siemens Vision head coil was also designed and constructed.

- **Data analysis:** A variety of software tools for post-processing and analysis of fMRI data were developed for this project. These include programs for spatial filtering of fMRI raw data, image alignment for motion correction, generation of statistical parametric maps, analysis of phase-encoded retinotopic data, and group averaging of fMRI time-series data. Detailed online documentation in HTML format is available for many routines [94].

Many of the above methods, apparatus, and software tools are currently being employed in collaborative studies of simple and complex motor tasks, visual activation, language localization, pre-surgical mapping, audition, pain, Parkinson's disease, working memory and epileptic lesion localization [95–98].

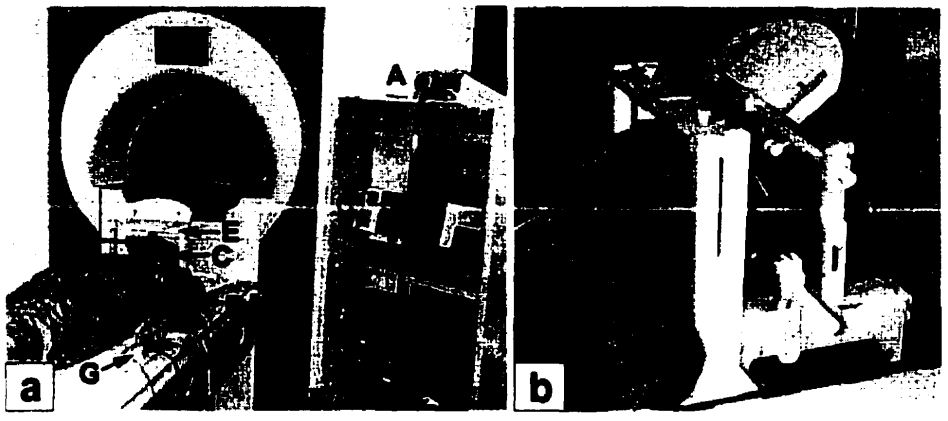

Figure 3.5: Experimental setup for fMRI studies. (a) Subject prepared for hypercapnia study with monitoring equipment for oxygen saturation (A), blood pressure (B), end tidal CO_2 (C), and face mask (D), head fixation device (E), back-projection screen (F), and mouse (G). (b) Close up of head fixation device showing ear-phones, nose bridge, mirror and quadrature surface coil.

Figure 3.6: Examples of visual stimuli used in fMRI studies. (a) High spatial frequency squarewave luminance grating. The grating was drifted across the visual field at one degree per second with the orientation varied three times per second. (b) Red uniform field. The display was alternated to isoluminant grey at 3Hz. (c) Yellow/blue radial checkerboard pattern. The grey arrowhead at the center of images is used to verify subject fixation and attention (see text for explanation).

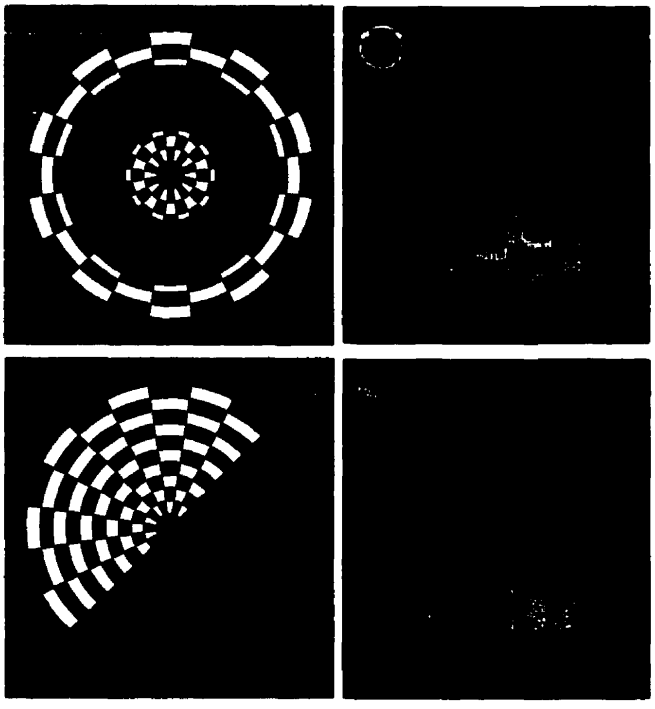

Figure 3.7: Patterns used for retinotopic mapping, with corresponding polar coordinate images. (a) Radial checkerboard pattern with cyclically dilating grey annulus (green arrows indicate dilation). (b) Resultant map of visual field eccentricity resampled and overlaid on BOLD image from interleaved sequence. (c) Radial checkerboard pattern with rotating grey hemifield (green arrows denote rotation). (d) Corresponding polar angle map.

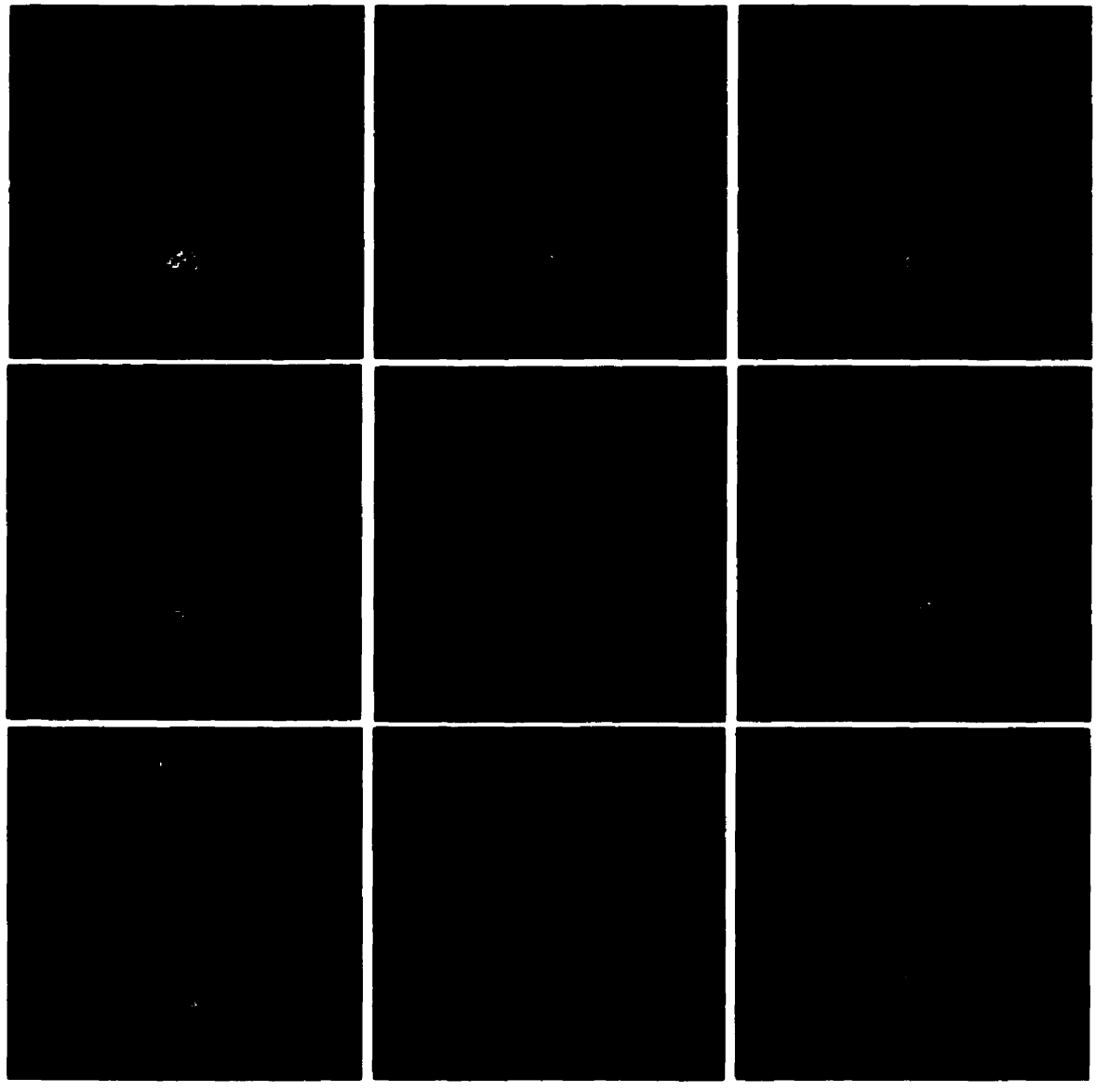

Figure 3.8: Examples of FFT modulus maps from phase-encoded retinotopic mapping sessions in different subjects, used for slice targeting and ROI delineation. The maps shown here have been resampled onto slices imaged in different sessions using the interleaved sequence. Images are shown unthresholded to show the exceptionally high SNR achievable using this approach.

Chapter 4:

Linear Coupling Between Cerebral Blood Flow and Oxygen Consumption in Activated Human Cortex

Preface

In this article, the first of the three presented in this dissertation, we report our finding that relative changes in cerebral blood flow and oxygen consumption are coupled in a consistent ~2:1 ratio. The role of oxidative metabolism in meeting focal energy demands during brain activation, an issue with critical implications for magnetic resonance-based functional brain imaging (fMRI) technology, is currently the subject of intense interest and debate in the neuroimaging community. While blood oxygenation-sensitive fMRI is rapidly becoming a tool of revolutionary importance in cognitive and clinical neuroscience, the relationship between oxygen utilization and perfusion regulation in activated human cortex has never been rigorously characterized. The study described in this article does so, revealing surprisingly strong oxidative metabolic effects in fMRI and helping to integrate prior observations into a coherent physiological framework.

The current paper unequivocally answers fundamental questions concerning the metabolic physiology of the human central nervous system, and has the potential to change the way that MRI-based brain activation data are interpreted. For these reasons, the paper was submitted as a concise report to *Proceedings of the National Academy of Sciences*, which offers the possibility of rapid publication in a journal aimed at a general biomedical audience.

Linear coupling between cerebral blood flow and oxygen consumption in activated human cortex

RICHARD D. HOGE, JEFF ATKINSON, BRAD GILL, GÉRARD R. CRELIER,

SEAN MARRETT*, AND G. BRUCE PIKE

Room WB325, McConnell Brain Imaging Centre, Montreal Neurological Institute, 3801 University St., McGill University, Montreal, Quebec, Canada H3A 2B4

**Nuclear Magnetic Resonance Center, Massachusetts General Hospital, Building 149, 13th St., Charlestown, Massachusetts, USA 02129*

Submitted to PNAS: Nov. 1998

Abstract

A quantitative model describing the relationship between hemodynamic and energetic events during increased neuronal activity is essential for the proper interpretation of functional brain images acquired using non-invasive methods such as functional magnetic resonance imaging and positron emission tomography. This requires data on the relationship between perfusion and oxygen consumption during graded activation in specific cortical tissue samples, however, and such information has not previously been available. In the present study, we measured cerebral blood flow and oxygen consumption in human primary visual cortex (V1) using magnetic resonance imaging during graded stimulation of different visual pathways. Fractional changes in blood flow and oxygen uptake were linearly coupled in a consistent ~2:1 ratio over a broad range of activation levels, with no evidence of an upper limit on oxygen consumption. These findings represent the first direct experimental evidence in humans of a specific regulatory relationship between cerebral blood flow and oxygen consumption, demonstrate that increased energy demands during brain activation are met almost entirely through oxidative metabolism, and reveal that the blood oxygenation level-dependent (BOLD) magnetic resonance signal is a linear index of neuronal energy consumption.

Introduction

The increasing importance in neuroscience of non-invasive functional imaging techniques has spurred intense interest in the metabolic physiology of human brain [99]; in particular, lack of a detailed understanding of the relationship between cerebral blood flow (CBF) and oxygen consumption (CMR_{O_2}) in activated brain has impeded rigorous physiological interpretation of images produced using methods such as blood oxygenation level-dependent functional magnetic resonance imaging (BOLD fMRI). Moreover, an improved understanding of cerebral metabolic requirements may aid in management of diseases such as stroke.

Previous studies of brain activation physiology, which examined specific neuronal systems during maximal stimulation [2, 3, 30, 42, 47, 100, 101], have consistently found oxygen consumption to increase significantly less than blood flow. It was originally believed that this arose because aerobic glycolysis reached maximal capacity near baseline levels, and observations of elevated tissue lactate during brain activation were felt to indicate that the resultant energy shortfalls were met anaerobically [41]. More recent theories suggest that oxidative metabolism may play a more important role in brain activation, however, and propose that the excess flow is needed to accelerate diffusion-limited delivery of oxygen by increasing blood-brain O_2 gradients [49, 102]. While CBF/CMR_{O_2} disparity at a single level of activation can be explained by either hypothesis, the two theories predict different relationships during graded activation. If aerobic metabolic capacity is limited, then CMR_{O_2} should plateau during intense stimulation. On the other hand, if the diffusion limitation hypothesis is correct, then CMR_{O_2} should rise monotonically with increasing blood flow. Due to the technical difficulty of measuring multiple physiological quantities during many activation conditions, however, there is almost no data tracking CBF/CMR_{O_2} coupling across graded activation states. The goal of the present study was therefore to determine the steady-state relationship between CBF and CMR_{O_2} in human primary visual cortex (V1) over a broad continuum

of flow rates.

Methods

In this section we first describe general procedures used in this study, followed by specific methodological information regarding MRI data acquisition, region of interest definition, visual stimulation, hypercapnic modulation of CBF, and CMR_{O_2} calculation.

The following approach was used to determine CMR_{O_2} at different perfusion levels: In one set of measurements, we determined the average blood oxygenation level-dependent (BOLD) MRI signal in peripheral V1 at various perfusion rates while oxygen consumption was held at a fixed baseline level. This was achieved using inhalation of different CO_2/air mixtures to induce graded hypercapnia in human subjects, resulting in direct vasodilatory stimulation with negligible effect on tissue metabolic rates [103, 104]. In a second set of measurements, randomly interleaved with the first, we presented a visual stimulus (a 4 cycle/degree black and white drifting squarewave grating) at contrast levels adjusted (based on pilot studies) to match the perfusion increases caused by hypercapnia while measuring the resultant BOLD signals.

Increasing tissue deoxyhemoglobin levels attenuates the BOLD MRI signal [25], but this effect includes contributions from flow-induced venous engorgement (cerebral blood volume effects), complicating determination of oxygen extraction at different flow rates. By comparing BOLD signals at matched perfusion levels, we were able to isolate the effect of metabolic deoxyhemoglobin production, providing a direct demonstration of increased oxygen consumption by activated neurons. Quantification of the corresponding CMR_{O_2} increases was performed using a biophysical model, described below [51, 105].

In addition to the above procedure, we performed identical experiments with other visual stim-

uli including radial checkerboards at different temporal frequencies and diffuse chromatic stimuli. In some cases, the patterns were chosen to produce preferential activation in V1 cell populations with different levels of the aerobic metabolic enzyme cytochrome oxidase [61, 106]; in others, stimulus parameters were adjusted to increase blood flow well above the range seen in hypercapnia.

A standardized experimental protocol (Fig. 4.1), in which BOLD and CBF responses were simultaneously measured and the different stimulation conditions interleaved in random order, was used for all experiments. Data were averaged over 12 subjects with different randomization orders, and baseline signal levels were sampled before and after each stimulation interval. The response to a given condition, for both CBF and BOLD signals, was defined as the mean value during a stimulation interval minus the average level during the adjacent baseline periods, expressed as a percentage of baseline. To ensure that only physiological steady-state responses were included in percent change calculations, data acquired less than one minute after changes in stimulation state were excluded. All relative signal changes for all conditions were referenced to the same baseline state, and spatial averages were restricted to V1 according to retinotopic maps acquired in preliminary scanning sessions. Subjects gave informed consent and the experimental protocol was approved by the Research Ethics Committee at the Montreal Neurological Institute.

MRI Data Acquisition

The BOLD signal and relative CBF were simultaneously recorded using an interleaved MRI pulse sequence consisting of a standard FAIR (flow sensitive alternating inversion recovery) acquisition [21] with a T_2^*-weighted (BOLD) echo-planar acquisition added after each of the two inversion-recovery acquisitions used in the basic FAIR technique (see Fig. 4.1c). The inversion time used in the FAIR acquisitions was 900ms, with an echo time of 20ms. A longer echo time of 50ms was

used in the T_2^*-weighted BOLD acquisitions. Single-slice images were acquired on a 64x64 matrix with 5x5mm^2 in-plane voxel dimensions and 7mm slice thickness, along an oblique axial plane parallel to the calcarine sulcus. Both FAIR and BOLD images used identical echo-planar imaging readouts, resulting in exact spatial correspondence between voxels in the two modalities. Excitation pulses were separated by a 3 second repetition time, and audible gradient activity associated with the inversion prepulses of the FAIR acquisition was duplicated before the BOLD acquisitions, making the different phases of the sequence indistinguishable to the subjects. BOLD contamination of FAIR data and inflow effects in BOLD images, assessed by examination of non-selective inversion recovery images and comparison of BOLD images following selective vs. non-selective acquisitions, were found to be negligible.

Head immobilization was achieved using an assembly incorporating a bite bar, rigidly mounted ear cups which could be tightly clamped against the head, and a small saddle-shaped fixture pressed firmly into the subject's nose bridge. Subject motion was negligible using this apparatus. A receive-only circularly polarized surface coil was built into the head immobilization apparatus, providing high signal-to-noise ratio MRI signals from the occipital lobe. All experiments were performed on a 1.5T Siemens Magnetom Vision MRI system.

Region of Interest Definition

To ensure a homogeneous and uniformly responding tissue sample, all measurements in this study included only tissue in primary visual cortex from 5–10° eccentricity. Region of interest masks for this portion of V1 were generated for each subject in separate preliminary scanning sessions, using phase-encoded retinotopic mapping [92], and then resampled onto the voxel grids used in subsequent experiments according to the computed transformation required to align high resolution anatomic images acquired at the beginning of each session [93]. Primary visual cortex was defined

as being the retinotopically organized region within the left or right calcarine sulcus containing a mirror-image representation of the contralateral visual hemifield. The 5–10° eccentricity range was chosen because it lay within the region stimulated by the test patterns used in our experiments while avoiding sagittal sinus interference and confluence of multiple visual areas which can occur near the fovea. Because all stimuli used in the present study encompassed this portion of the visual field, every voxel within the retinotopically defined region of interest was guaranteed to contain activated neurons during stimulation. Examples of images used for this procedure are shown in Fig. 4.2.

Visual Stimulation

Visual stimuli were generated in real time using a Silicon Graphics O_2 computer with OpenGL-based software. The RGB output was used to drive a NEC MT820 LCD projector operating in 640x480 mode at 60Hz. Subjects viewed stimuli projected onto a screen mounted above their heads via a mirror while they lay prone in the scanner. Stimulus presentation was automatically synchronized to data acquisition, and alertness and fixation were continually verified and logged in all subjects by requiring them to report, at three second intervals throughout all experiments, the orientation of a small, low contrast triangular fixation marker which was present at the center of the display in a left-right orientation (◀ or ▶) that was varied at random intervals. Feedback was given via an MRI compatible two-button mouse.

The 4 cycle per degree black and white squarewave grating stimulus used to match hypercapnia-induced perfusion increases drifted across the visual field at one degree per second at systematically varied orientations. This stimulus has been found, in previous autoradiographic studies [61, 106], to selectively activate inter-blob regions in primate V1. A red uniform field changed to isoluminant grey and back at 3 Hz was used in subsequent experiments to bias activation towards V1

blob domains, which contain higher levels of cytochrome oxidase. Radial checkerboard patterns were employed as non-specific stimuli. These contained both color (yellow/blue) and luminance contrast, with 30 spokes and 6.5 rings (counting from 0.5–10° eccentricity) of equal radial thickness, modulated in a temporal squarewave at various frequencies. The same baseline condition, consisting of a uniform grey field at the mean luminance of the stimulus patterns, was presented at the beginning and end of all scanning runs in this study, as indicated in Fig. 4.1b. Potency of the various stimuli was varied by changing their luminance contrast and, where applicable, color saturation (by dilution with variable amounts of white). All stimuli converged in appearance to the uniform grey field as contrast/saturation approached zero.

Hypercapnic Modulation of CBF

We induced graded hypercapnia by administering different concentrations of a CO_2/air mixture through a non-rebreathing face mask (Hudson RCI Model 1069) worn by subjects. The baseline condition was always inhalation of atmospheric composition medical air ([CO_2] < 300ppm) delivered at 16L/min while attending to a standard baseline visual display (uniform grey field with attention/fixation task). Hypercapnic episodes were initiated during scanning runs by switching the breathing gas to a mixture of 5:21:74% CO_2:O_2:N_2 (BOC Canada Ltd.) and medical air. Different levels of hypercapnia (inhaled CO_2 concentrations of 1.25%, 2.5%, 3.75%, and 5%) were achieved by combining the pre-mixed CO_2/air preparation with medical air in a Y-connector and adjusting respective flow rates to achieve the desired proportions while maintaining a total flow rate of 16 L/min. End-tidal CO_2, which was measured via a nasal cannula with monitoring aspirator (Normocap 200, Datex Inc.), increased by 5±1 mmHg on average during inhalation of the highest concentration CO_2 mixture. Subjects were instructed to breathe at a constant rate, which was easily maintained to within ± one breath per minute. Pulse rate and arterial oxygen saturation

were also monitored (Oxygen/Pulse Monitor, Nonin Medical Inc.) and these remained constant throughout hypercapnia experiments.

CMR_{O_2} Calculation

The method of Davis *et al.* [51] was extended to incorporate our graded hypercapnia measurements and a novel formalism for interpreting simultaneously acquired BOLD and CBF data in terms of iso-CMR_{O_2} contours in the BOLD-CBF plane. All raw BOLD and perfusion measurements were spatially averaged within peripheral V1 and then pooled across subjects prior to subsequent display and processing, although averaging of multiple sessions performed on a single subject confirmed that individual responses resembled group averages. BOLD vs. perfusion data measured during graded hypercapnia (Fig. 4.4a) were fit with the function

$$\frac{\Delta \mathrm{BOLD}}{\mathrm{BOLD}_0} = M\left(1 - \left(\frac{\mathrm{CMR}_{O_2}}{\mathrm{CMR}_{O_2|0}}\right)^{\beta}\left(\frac{\mathrm{CBF}}{\mathrm{CBF}_0}\right)^{\alpha-\beta}\right) \tag{4.1}$$

by setting $\frac{\mathrm{CMR}_{O_2}}{\mathrm{CMR}_{O_2|0}}$ to one and adjusting the parameter M (zero subscripts denote baseline values). The constants α and β, which respectively reflect the influences of blood volume and deoxyhemoglobin concentration, were assigned values of $\alpha = 0.38$ and $\beta = 1.5$ [51, 107, 108]. Pulse sequence-specific iso-CMR_{O_2} contours in the BOLD vs. perfusion plane were then calculated at 10% intervals using the fitted M value of 0.22. Solution of the fitted equation for $\frac{\mathrm{CMR}_{O_2}}{\mathrm{CMR}_{O_2|0}}$ permitted calculation of fractional CMR_{O_2} changes from the measured BOLD and perfusion data. These measurements are likely to be accurate and robust, since our data lie within the linear regime of the BOLD-CBF-CMR_{O_2} relationship. $CMRO_2$ estimates in this domain depend primarily on the slope of the BOLD vs. perfusion relationship for hypercapnia, and are only weakly influenced by the model parameters α and β. It can be shown that iso-CMR_{O_2} contours must be close to parallel in this region, and that the spacing between them for a given $CMRO_2$ step size is approximately

constant and proportional to $|\vec{\nabla}(\frac{CMRO_2}{CMRO_2|_0})|^{-1} \simeq \frac{m}{(1-\frac{\alpha}{\beta})}$ where m is the slope of the BOLD vs. perfusion relationship for hypercapnia. This function is only weakly sensitive to changes in the ratio $\frac{\alpha}{\beta}$, which are likely to be small in our experiments.

Results

Figure 4.3a shows perfusion as a function of time, averaged over twelve subjects, for four levels of hypercapnia (black) and for visual stimulation with the high spatial frequency squarewave grating (red) at contrast levels adjusted to match the hypercapnia-induced perfusion increases. The corresponding BOLD signals (Fig. 4.3b) reveal significant attenuation of the visually evoked responses compared with those produced by hypercapnia. The degree of attenuation increased with perfusion, indicating that CBF and CMR_{O_2} underwent coupled increases.

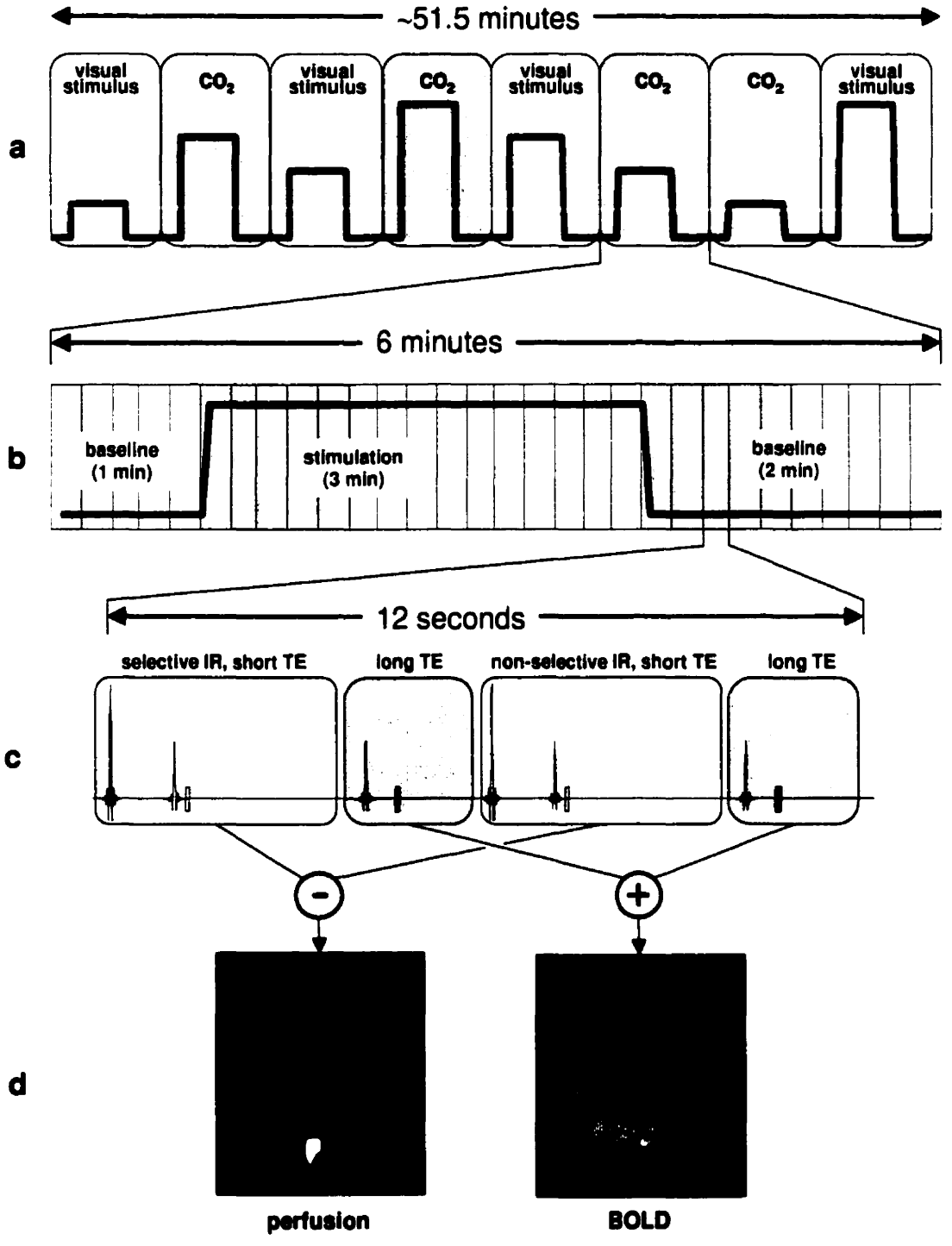

Figure 4.1: See caption next page

Fig. 4.1 (previous page). Outline of approach used for simultaneous measurement of BOLD and perfusion signals during graded visual stimulation and hypercapnia. **(a)** Timeline of experimental session, comprising eight scanning runs. Randomly graded stimulus levels in different runs are indicated by the variable-height square pulses. **(b)** Timeline of a single scanning run within a session. A single cycle of stimulation was performed in each run, denoted by the square pulse. Each run resulted in the acquisition of 30 BOLD/perfusion image pairs (rectangular blocks). Image pairs shaded in grey were excluded from calculations of steady-state percent change. **(c)** Interleaved MRI pulse sequence used to acquire BOLD/perfusion image pairs. Scans 1 and 3 (white blocks) constitute a FAIR acquisition, while scans 2 and 4 (grey blocks) are T_2^*-weighted (long echo time) acquisitions which are added to produce a single BOLD image overlapping in time with the perfusion image. **(d)** Examples of perfusion and BOLD images for a single subject acquired simultaneously using the interleaved pulse sequence.

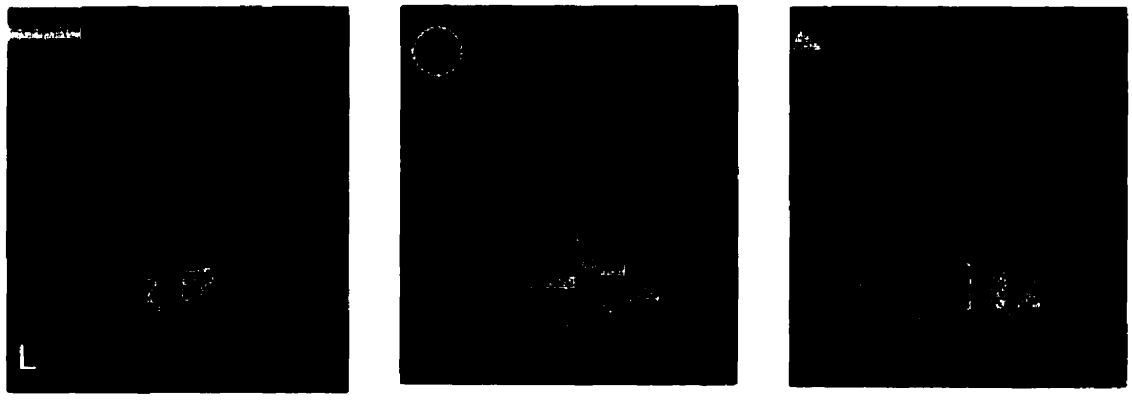

Figure 4.2: Example of resampled retinotopic mapping data, used for restriction of spatial averages, from a single subject. **(a)** Normalized FFT modulus map showing retinotopic responses at the fundamental frequency of a cyclically dilated visual stimulus. **(b)** Map of visual field eccentricity in retinotopically organized areas, overlaid on BOLD image acquired with interleaved sequence. Only the region receiving input from 5 to 10° (~green→yellow, inclusive, in eccentricity map) in each subject was included in percent change calculations. **(c)** Polar angle map for the same subject overlaid on BOLD image. Retinotopic representation of the contralateral visual hemifield within the left and right calcarine sulci was a criterion for V1 identification.

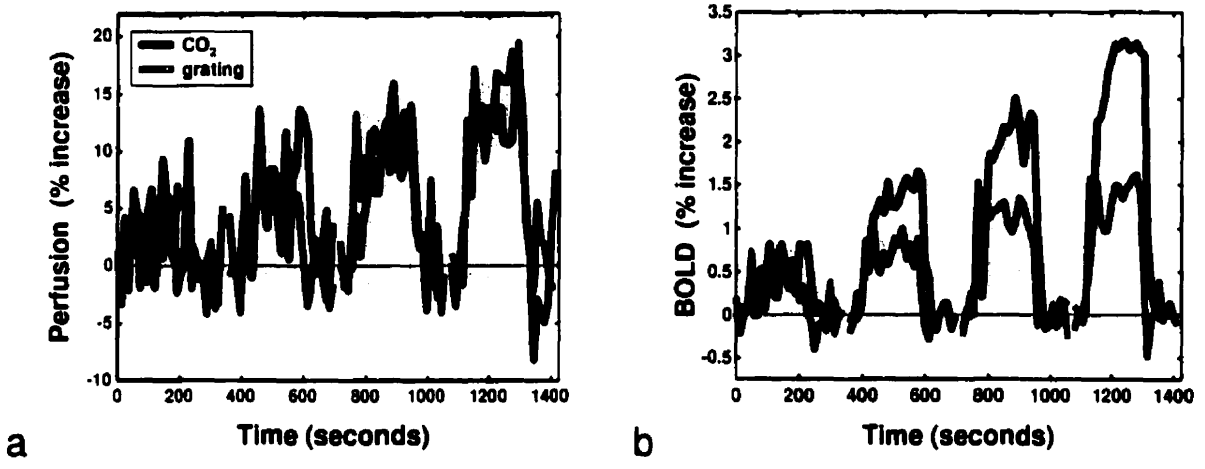

Figure 4.3: Perfusion and BOLD signals as a function of time during graded hypercapnia and visual stimulation (n = 12; stimulation intervals indicated by grey background). **(a)** Relative perfusion as a function of time during graded hypercapnia (black curve) and graded visual stimulation (red curve) with contrasts adjusted to match hypercapnia-induced CBF increases. **(b)** BOLD signal as a function of time during perfusion increases shown in (a). BOLD signals during visual stimulation are significantly lower than those observed during hypercapnia at matched perfusion levels, revealing graded increases in oxygen consumption.

The other visual stimuli also produced strong attenuation of the BOLD signal within the range of perfusion levels attained with hypercapnia, and the trend of systematic BOLD attenuation (compared to the extrapolated hypercapnia relationship) was maintained at higher perfusion levels. Figure 4.4a shows average increases in the oxygenation-dependent MRI signal plotted as a function of perfusion increase for all of the visual stimuli used in this study, as well as hypercapnia. Every combination of BOLD and perfusion values corresponds to a specific rate of oxygen consumption, with the hypercapnia data points tracing out a baseline iso-CMR_{O_2} contour. Non-baseline contours, calculated by fitting Eqn. 1 to the hypercapnia data, are shown at 10% intervals.

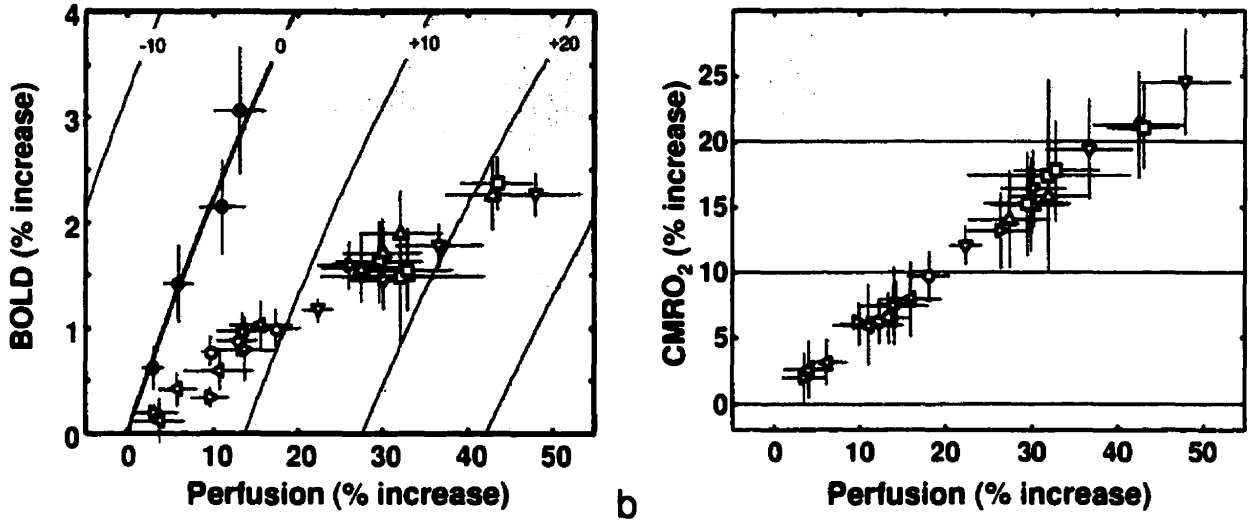

a b

c

Symbol	Stimulus	$\frac{\Delta CMR_{O_2}}{\Delta CBF}$	subjects
•	hypercapnia (4 CO_2 concentrations)	0	12
◁	high spatial frequency black/white grating (4 contrast levels)	0.5±0.1	12
▷	3Hz red uniform field to isoluminant grey (4 color saturations)	0.51±0.08	12
○	4Hz yellow/blue radial checkerboard (4 low contrast levels)	0.52±0.06	12
▽	4Hz yellow/blue radial checkerboard (4 high contrast levels)	0.52±0.04	1
△	8Hz yellow/blue radial checkerboard (4 intermediate contrast levels)	0.50±0.02	6
□	yellow/blue radial checkerboard (4 frequencies: 2, 4, 6, 8 Hz)	0.51±0.08	6

Figure 4.4: Coupling relationships between CBF and CMR_{O_2} during graded visual stimulation. **(a)** Plot of BOLD vs. perfusion increases (±SE) during different types of stimulation, with iso-CMR_{O_2} contours at 10% intervals. **(b)** Relative CMR_{O_2} responses to different stimuli, calculated using the BOLD-CBF data in (a). The data reveal a coupling Δ%CBF : Δ%CMR_{O_2} ratio of ~2:1.

Figure 4.4b shows CMR_{O_2}, computed by inverting the fitted model at measured BOLD and CBF values, plotted as a function of CBF. All visual stimuli produced linearly ($r > 0.98$) coupled CBF and CMR_{O_2} responses with an average slope of 0.51 ± 0.02 (slopes for different stimulus types are tabulated in Fig. 4.4c). This value, which represents the fraction of additionally delivered oxygen that is consumed by tissues, is similar to the baseline oxygen extraction fraction for brain (40–60% [109]). The CMR_{O_2} value measured at maximal stimulation (4Hz radial checkerboard at full contrast) using the MRI-based approach described above was in exact agreement with a reference point established under identical conditions using positron emission tomography [2].

Discussion

The above data support a simple view of the metabolic and circulatory events accompanying brain activation. Because oxidative metabolism of glucose accounts for over 99% of ATP production in brain tissue [40], increases in steady-state CMR_{O_2} signify proportional changes in energy expenditure. We can therefore conclude that during maximal visual stimulation, energy consumption in V1 rose by approximately 25%. This was sustained through an equal rise in the rate of aerobic metabolism, requiring a perfusion increase of roughly 50% to achieve the necessary rise in blood-brain O_2 diffusion, in general accordance with recently introduced theoretical models [49, 102, 110]. The proportionality between percent increases in CBF and CMR_{O_2} (Δ%CBF and Δ%CMR_{O_2}, respectively), was the same for all visual stimuli examined, including patterns believed to stimulate tissues with different levels of aerobic metabolic enzymes.

Fox *et al.* [30] reported that, unlike CMR_{O_2}, glucose uptake is coupled to blood flow in a relative ratio of 1:1. While it was originally suggested that limitations in aerobic capacity led to shortfalls in energy production which had to be met through anaerobic glycolysis, the significant

CMR_{O_2} increases observed in our experiments indicate that this is not the case. Given the 2:1 coupling between fractional increases in glucose delivery (blood flow) and oxidative glycolysis observed in our experiments, purely anaerobic metabolism of the residual glucose would contribute negligible amounts of energy. We propose that glucose uptake for purely anaerobic metabolism proceeds as an incidental consequence of the large flow increases required for delivery of additional oxygen combined with the fact that any available glucose is readily transported into tissues by facilitated diffusion. This hypothesis reconciles reports of increased tissue lactate during activation [41] with the finding that most energy consumed during such episodes is produced aerobically. A number of studies have demonstrated that glucose transport rates in brain are several times greater than rates of phosphorylation, indicating that the latter is the rate-limiting step for anaerobic glucose utilization [111, 112].

It is unlikely that differences in blood volume during hypercapnia and visual stimulation caused the signal reductions that were observed at equal perfusion levels. The BOLD signal depends exclusively on the volume fraction of *deoxygenated* blood in tissue, which can only be increased by distension of venous vessels. Because available evidence [113–116] indicates that this is a passive biomechanical process, venous blood volume can be considered a simple correlate of perfusion.

In conclusion, we emphasize that our results support the use of BOLD contrast as a generally applicable marker for neuronal activation. Increased energy needs are met through acceleration of aerobic metabolism with linear coupling of Δ%CBF:Δ%CMR_{O_2} in a ~2:1 ratio over a broad range of activity levels. The resultant BOLD signal increases are linearly proportional to Δ%CBF, and hence to increases in neuronal energy consumption, if systemic physiological parameters (*e.g.* arterial CO_2 levels) are stabilized.

Acknowledgements

We thank Pamela Rabbitz for technical assistance. We are also grateful to Curtis Baker, Gareth Barnes, Cathy Bushnell, Ken Kwong, Joe Mandeville, Eric Shoubridge, and Gary Zaharchuk for discussion and critical reading of the manuscript. This work was supported by the Killam Foundation, FRSQ (Canada), and the Whitaker Foundation.

Chapter 5:

Investigation of BOLD Signal Dependence on CBF and CMR_{O_2}: The Deoxyhemoglobin Dilution Model

Preface

The previous paper introduced a novel experimental protocol based on matching activation-induced perfusion increases, using hypercapnia, to isolate the effects of metabolic deoxyhemoglobin production on the BOLD fMRI signal. While this provided strong model-independent evidence for graded increases in oxygen consumption, the ability to make quantitative estimates of changes in oxygen consumption rates was critical for determination of neuronal energy demands. In the last chapter, model-based calculations were used to quantify the relative changes in CMR_{O_2} implied by our data, and while the resultant values were in close agreement with a reference point established using PET, the biophysical model used has never been thoroughly investigated.

In the current paper, a detailed analysis of the model used for CMR_{O_2} calculation in the previous study is given, and a novel model formulation that predicts highly specific characteristics in the relationship between the BOLD signal, perfusion, and cerebral oxygen consumption is presented. I also introduce a novel graphical formalism for interpreting simultaneously acquired perfusion and BOLD measurements in terms of iso-CMR_{O_2} contours on the BOLD-CBF plane.

In the experimental portion of this paper, different combinations of graded hypercapnia and visual stimulation were used to investigate the effects of perfusion and oxygen consumption on the BOLD signal, and to test predictions made using the quantitative model. The experimental data are in impressive agreement with the theoretical predictions, greatly strengthening confidence in model-derived estimates of relative CMR_{O_2} presented in this and the previous paper.

Because the previous paper was a concise report focusing on the physiological significance of our findings, the data contained therein are also included in the present, more comprehensive article. The current paper also included several additional large multi-subject experiments and places an emphasis on biophysical modeling issues.

Investigation of BOLD Signal Dependence on CBF and CMR_{O_2}: The Deoxyhemoglobin Dilution Model

RICHARD D. HOGE, JEFF ATKINSON, BRAD GILL, GÉRARD R. CRELIER,

SEAN MARRETT*, AND G. BRUCE PIKE

McConnell Brain Imaging Centre, Montreal Neurological Institute, McGill University, Montreal, Quebec, Canada

**Nuclear Magnetic Resonance Center, Massachusetts General Hospital, Charlestown, Massachusetts, USA*

Submitted to Magnetic Resonance in Medicine: Oct. 1998

Running Head: Investigation of BOLD signal dependence on CBF and CMR_{O_2}

Abstract

The relationship between blood oxygenation level-dependent (BOLD) MRI signals, cerebral blood flow (CBF), and oxygen consumption (CMR_{O_2}) in the physiological steady-state was investigated. A quantitative model, based on flow-dependent dilution of metabolically generated deoxyhemoglobin, was validated by measuring BOLD signals and relative CBF simultaneously in the primary visual cortex (V1) of human subjects ($n = 12$) during graded hypercapnia at different levels of visual stimulation. BOLD and CBF responses to specific conditions were averaged across subjects and plotted as points in the BOLD-CBF plane, tracing out lines of constant CMR_{O_2}. The relationship between different iso-CMR_{O_2} contours was consistent with the quantitative dHb dilution model, supporting its use in MRI-based CMR_{O_2} measurement techniques. Analysis of data acquired during graded visual stimulation indicated that relative changes in CBF and CMR_{O_2} are coupled in an approximate ratio of $\sim$2:1 over a wide range of activation conditions.

Index terms: BOLD contrast • aerobic metabolism • perfusion • hypercapnia

Introduction

A detailed understanding of the relationship between the blood oxygenation level-dependent (BOLD) MRI signal, cerebral blood flow (CBF), and oxygen consumption (CMR_{O_2}) is critical for the rigorous physiological interpretation of BOLD fMRI activation data. It is also essential for validation of MRI-based methods for measuring CMR_{O_2} that have recently been proposed [51, 117].

Sensitivity to blood oxygenation arises in T_2^*-weighted MR images of the brain because the local image intensity is generally subject to some degree of attenuation caused by deoxyhemoglobin (dHb), a paramagnetic relaxation enhancer introduced into venous blood as tissues extract oxygen for aerobic metabolism. Increasing the perfusion rate in a tissue volume element generally leads to dilution of venous deoxyhemoglobin [118], reducing the tendency of the blood to attenuate the magnetic resonance signal. The resultant increase in signal intensity, referred to as the BOLD response, can be detected in images and forms the basis for functional MRI brain mapping [17, 25]. Increases in blood flow rate also cause distension of the highly compliant venous vessels, however, and the resultant increase in the fraction of tissue volume occupied by deoxygenated blood partially counteracts the diluting effect of the perfusion increase. If the rise in perfusion is due to heightened neuronal activity, then metabolic oxygen extraction may also increase, accelerating the production of deoxyhemoglobin and further counteracting the dilution effect. The role of aerobic metabolism in meeting increased energy demands during neuronal activation has, however, been a point of considerable debate [99].

Cerebral blood volume has been found to be highly correlated with steady state perfusion level over a broad range of flow rates [107, 119]. Perfusion is, in turn, regulated by varying the diameter of arterioles feeding a region of tissue. This mechanism generally serves to sustain tissue metabolism at different levels of activity, but pharmacological perturbations, such as CO_2 inhalation and infusion of L-arginine or acetazolamide, can be used to induce arteriolar dilation indepen-

dent of tissue metabolism [104, 107, 120–125].

Although neurally mediated arteriolar dilation is the mechanism by which CBF is regulated, the influence of arterial blood on the BOLD signal is probably insignificant since it comprises a relatively small fraction (~25%) of total CBV and contains negligible amounts of deoxyhemoglobin [109]. MRI-relevant changes in total CBV are therefore due primarily to passive inflation of venules caused by the elevation of venous blood pressure occurring when arteriolar resistance is lowered [76, 115, 126]. Because of their passive, mechanical nature, venous CBV changes are believed to be simple correlates of CBF, independent of the cause of the perfusion increase.

While it appears possible to specify a stimulus-independent relationship linking CBF and CBV (*i.e.* Grubb's formula [107]), it is not possible to do so for CBF and CMR_{O_2} because CBF can be manipulated independently of tissue metabolism by introducing vasoactive substances such as CO_2 into the blood. Nevertheless, it is conceivable that a fixed relationship between CBF and CMR_{O_2}, analogous to Grubb's formula, may apply during brain activation if systemic physiological parameters are stabilized. Oxidative metabolism is responsible for generating virtually all deoxyhemoglobin in tissues, and is therefore a critical determinant of the BOLD signal. Under steady-state conditions, CMR_{O_2} depends primarily on the rate of ATP turnover in tissues and the availability of oxygen and glucose.

A number of theoretical and experimental studies have examined BOLD signal dependence on the concentration of deoxyhemoglobin in venous blood ($[dHb]_v$) and the blood volume fraction of tissue [87, 88, 105, 108, 127, 128]. Because these parameters directly reflect the amount and distribution of dHb in tissues, it is possible to predict their influence on the T_2^*-weighted MRI signal using Monte Carlo simulations and *in vitro* model systems.

Venous blood volume and deoxyhemoglobin concentration, in turn, depend primarily on local rates of cerebral blood flow and oxygen consumption. While BOLD signal dependence on CBV

and $[dHb]_v$ has been reasonably well characterized, there is much less data on the influence of CBF and CMR_{O_2}, which are more directly linked to neuronal activity. Furthermore, the limited amount of experimental data that does exist has been difficult to integrate into a coherent framework. Kim *et al.* measured BOLD signal and perfusion values at a single level of visual stimulation and, using the quantitative biophysical model of Ogawa *et al.* [105] to interpret their data, concluded that oxygen consumption did not increase during visual stimulation [42]. Davis *et al.* measured BOLD and perfusion data at a single level of hypercapnia and at a single level of visual stimulation and, using a different formulation of Ogawa's model, concluded that oxygen consumption increased [51]. While the latter study made the important advance of using hypercapnia to calibrate the BOLD signal, the single level of activation and hypercapnia used did not permit elucidation of variable relationships between physiological and MRI parameters. Lack of validation of the quantitative relationships used to calculate CMR_{O_2} in the studies cited above makes it difficult to assess the accuracy of those measurements, which were not verified using an independent standard such as positron emission tomography (PET).

Two fundamental relationships must be better characterized to establish the exact physiological significance of activation-induced BOLD signals and validate MRI-based CMR_{O_2} measurement techniques. The first is the dependency of the BOLD signal on CBF when oxygen consumption is held constant, and the second is the association between these quantities during neuronal activation. Both of these relationships may vary between tissue samples (*e.g.* different MR image voxels), and the latter relationship could conceivably vary within a given tissue sample for different types of stimulation. In this study we focus on examining steady-state signals in a single cortical area with well defined and homogeneous characteristics (peripheral V1). Although transient features of the BOLD response such as the initial dip [50, 72, 73], and post-stimulus undershoot [129–131] have attracted considerable interest recently, clarification of the steady-state relationship between

the BOLD signal, CBF, and CMR_{O_2} is essential for understanding the physiological basis of the BOLD effect.

This report presents a detailed derivation of a specific formulation of the deoxyhemoglobin dilution model of BOLD contrast, emphasizing quantitative predictions of BOLD signal dependence on CBF and CMR_{O_2}. We introduce the concept that, for a homogeneous tissue sample, different combinations of BOLD and CBF responses represent specific levels of CMR_{O_2} (CBV is assumed to be a simple correlate of CBF). Plots of simultaneously measured BOLD and perfusion-sensitive fMRI responses on orthogonal axes can therefore be viewed as maps of CMR_{O_2} on the BOLD-CBF plane. We demonstrate that by introducing vasoactive substances such as CO_2 into the arterial blood to manipulate CBF independently of tissue metabolism during different levels of neuronal activation, it is possible to trace out lines of constant CMR_{O_2} (iso-CMR_{O_2} contours) in such maps.

By adjusting the contrast of a visual stimulus to match hypercapnia-induced perfusion increases, we show that activation-induced BOLD responses include significant attenuation due to increases in metabolic dHb production. The resultant BOLD-CBF coordinates are shown to travel between, rather than along, iso-CMR_{O_2} contours, with trajectories that are co-linear for different types of visual stimulus. A modified version of the method of Davis *et al.* [51] is used for explicit calculation of relative CMR_{O_2} changes, and the region of the BOLD-CBF plane corresponding to a relative Δ%CBF:Δ%CMR_{O_2} coupling ratio of $\sim$2:1 is shown to encompass the BOLD and CBF responses observed over a broad range of activation states. This work confirms our preliminary observations of an identical coupling ratio, made using different pulse sequences and visual stimuli and reported previously in abstract form [132, 133]. We also included an activation paradigm characterized in a previous PET study of CBF and CMR_{O_2} [2], providing an independently determined reference point for our quantitative results.

Theory

Here we present a quantitative model predicting BOLD signal changes during increased cerebral blood flow and oxygen consumption, based on expected changes in venous dHb concentration and CBV. The expressions derived constitute an alternate formulation of previous biophysical models [51, 105, 117], with an emphasis on testable predictions of BOLD-CBF interdependence. We introduce a novel formalism for interpreting simultaneously acquired BOLD and CBF data in terms of iso-CMR_{O_2} contours in the BOLD-CBF plane, and an extension of the calibration method described in [51] that incorporates graded hypercapnia.

We first consider the effect of the amount and distribution of deoxyhemoglobin in tissues. The net rate constant R_2^* for transverse relaxation can be viewed as the sum of a component $R_2^*|_{dHb}$ caused by deoxyhemoglobin and a contribution, $R_2^*|_{other}$, due to other sources:

$$R_2^* = R_2^*|_{dHb} + R_2^*|_{other}. \tag{5.1}$$

Boxerman *et al.* determined that $R_2^*|_{dHb}$ was related to CBV and $[\mathrm{dHb}]_v$ according to the expression

$$R_2^*|_{dHb} = A \cdot \mathrm{CBV} \cdot [\mathrm{dHb}]_v^{\beta}. \tag{5.2}$$

where A is a field strength and sample-specific proportionality constant and β is a constant, in the range $1 \leq \beta \leq 2$, depending on the average blood volume within a tissue sample. The accuracy of this semi-empirical expression was thoroughly validated using *in vitro* models [108].

The magnitude of $R_2^*|_{dHb}$ is reduced by increases in CBF, due to dilution of venous deoxyhemoglobin, although resultant CBV increases partially counteract this effect. The change in transverse relaxation rate ($\Delta R_2^*|_{dHb}$) at non-baseline values of CBV and $[\mathrm{dHb}]_v$ can be expressed as follows, based on Eqn. 5.2:

$$\Delta R_2^*|_{dHb} = A\left(\mathrm{CBV}[\mathrm{dHb}]_v^{\beta} - \mathrm{CBV}_0[\mathrm{dHb}]_{v_0}^{\beta}\right), \tag{5.3}$$

where the subscript '0' is used here and elsewhere in the text to refer to the baseline steady-state value of a variable.

Reductions in $R_2^*|_{dHb}$ lead to increases in the T_2^*-weighted image intensity observed at a given echo time (TE), which can be expressed in fractional form as

$$\frac{\Delta \mathrm{BOLD}}{\mathrm{BOLD}_0} = e^{-\mathrm{TE}\,\Delta R_2^*|_{dHb}} - 1. \tag{5.4}$$

For the small changes in $R_2^*|_{dHb}$ that occur during fMRI experiments, the exponential function in Eqn. 5.4 can be linearized, resulting in the following simplified expression:

$$\frac{\Delta \mathrm{BOLD}}{\mathrm{BOLD}_0} \simeq -\mathrm{TE}\,\Delta R_{2_{dHb}}^*. \tag{5.5}$$

Substitution of Eqn. 5.3 for $\Delta R_2^*|_{dHb}$ leads to

$$\begin{aligned} \frac{\Delta \mathrm{BOLD}}{\mathrm{BOLD}_0} &\simeq \mathrm{TE} \cdot A\left(\mathrm{CBV}_0[\mathrm{dHb}]_{v_0}^{\beta} - \mathrm{CBV}[\mathrm{dHb}]_v^{\beta}\right) \\ &\simeq \mathrm{TE} \cdot A \cdot \mathrm{CBV}_0 \cdot [\mathrm{dHb}]_{v_0}^{\beta}\left(1 - \left(\frac{\mathrm{CBV}}{\mathrm{CBV}_0}\right)\left(\frac{[\mathrm{dHb}]_v}{[\mathrm{dHb}]_{v_0}}\right)^{\beta}\right). \end{aligned} \tag{5.6}$$

The term $\mathrm{TE} \cdot A \cdot \mathrm{CBV}_0 \cdot [\mathrm{dHb}]_{v_0}^{\beta} = \mathrm{TE} \cdot R_2^*|_{dHb_0}$ is approximately equal to the fractional BOLD signal attenuation that occurs due to deoxyhemoglobin at baseline, and therefore represents the maximum possible BOLD response (as pointed out by Davis in [51]). For clarity we use the constant M to denote this quantity:

$$M \equiv \mathrm{TE} \cdot A \cdot \mathrm{CBV}_0 \cdot [\mathrm{dHb}]_{v_0}^{\beta}. \tag{5.7}$$

We assume that there is a consistent functional relationship between blood flow and volume, in which CBV depends passively on CBF. Several investigators have determined this to be

$$\frac{\mathrm{CBV}}{\mathrm{CBV}_0} = \left(\frac{\mathrm{CBF}}{\mathrm{CBF}_0}\right)^{\alpha} \tag{5.8}$$

where α is a constant with an approximate value of 0.38 [107, 134]. The baseline-normalized CBV term of Eqn. 5.6 can thus be determined from MRI-based measurements of relative CBF (defined here as the volume flux of blood per unit time through a tissue volume element, normalized to baseline).

Assuming that the concentration of deoxyhemoglobin in arterial blood is negligible, the steady-state dHb concentration within the venous compartment of a constant unit volume element of tissue depends on CMR_{O_2} and CBF, from basic mass conservation (Fick's Principle):

$$[\mathrm{dHb}]_v = \frac{1}{4}\frac{\mathrm{CMR_{O_2}}}{\mathrm{CBF}}, \tag{5.9}$$

where simplified units of $\frac{\mathrm{mol}}{\mathrm{ml}}$, $\frac{\mathrm{mol}}{\mathrm{sec}}$, and $\frac{\mathrm{ml}}{\mathrm{sec}}$ are used respectively for $[\mathrm{dHb}]_v$, CMR_{O_2}, and CBF (the factor $\frac{1}{4}$ reflects the fact that each dHb molecule delivers $4O_2$). If CMR_{O_2} is held constant, the baseline-normalized $[\mathrm{dHb}]_v$ term in Eqn. 5.6 is therefore inversely proportional to normalized CBF, reflecting simple dilution:

$$\frac{[\mathrm{dHb}]_v}{[\mathrm{dHb}]_{v_0}} = \frac{\mathrm{CBF_0}}{\mathrm{CBF}}. \tag{5.10}$$

Substitution of Eqs. 5.8 and 5.10 into Eqn. 5.6 gives the following expression predicting the fractional BOLD signal change for a given change in relative CBF at constant CMR_{O_2}:

$$\frac{\Delta\mathrm{BOLD}}{\mathrm{BOLD_0}} = M\left(1 - \left(\frac{\mathrm{CBF}}{\mathrm{CBF_0}}\right)^{\alpha-\beta}\right). \tag{5.11}$$

Because β is larger then α by at least a factor of two [107, 108, 115, 134], the exponent $\alpha - \beta$ is negative and the term $\left(\frac{\mathrm{CBF}}{\mathrm{CBF_0}}\right)^{\alpha-\beta}$ decreases with increasing CBF, leading to monotonic BOLD increases with perfusion. Figure 5.1a shows Eqn. 5.11 plotted over a large range of CBF values with $\alpha = 0.38$ and $\beta = 1.5$. The predicted BOLD-CBF relationship for constant CMR_{O_2} contains a linear region for moderate CBF increases (up to ~50%), but over a larger range the function becomes increasingly sub-linear and eventually plateaus to an asymptotic value of M. This picture

is intuitively correct, since we would expect monotonic increases in the BOLD signal which must be close to linear for small changes but plateau to some maximal level when capillary transit occurs so rapidly that venous blood is completely oxygenated.

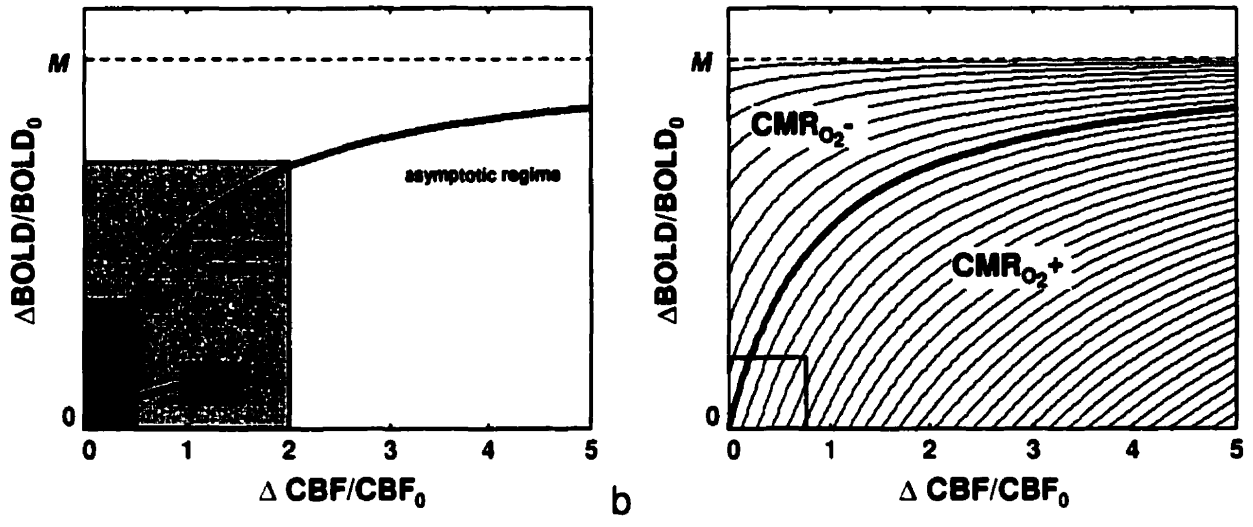

Figure 5.1: Relationships between BOLD MRI signal, CBF, and CMR_{O_2} predicted by the deoxyhemoglobin dilution model. (a) Fractional BOLD signal change, plotted as a function of fractional CBF change, calculated using Eqn. 5.11 with $\alpha = 0.38$ and $\beta = 1.5$. The predicted function has a linear domain for perfusion increases up to approximately 50%, and becomes nonlinear at higher CBF levels. In the theoretical limit of very high perfusion rates, venous blood is completely oxygenated, leading to a sample-dependent asymptotic upper limit of M for BOLD signal increases. (b) Iso-CMR_{O_2} contours predicted by the deoxyhemoglobin dilution model at 10% intervals. Increases in CMR_{O_2} lead to reductions in the BOLD signal observed at a given level of CBF, producing BOLD-CBF data in the zone labeled 'CMR_{O_2}+'. Every point along an iso-CMR_{O_2} contour corresponds to a different CBF:CMR_{O_2} coupling ratio. Iso-CMR_{O_2} contours are evenly spaced and approximately parallel over small patches of the BOLD-CBF plane, as indicated in the small box in the lower left corner of the plot.

The curve in Fig. 5.1a can be viewed as the baseline iso-CMR_{O_2} contour in the BOLD-CBF plane. The shape of this function, and hence the extent of the linear domain, depends entirely on the difference $\alpha - \beta$; only the vertical scale factor M is unknown. Inspection of Eqn. 5.7 reveals that

M depends on the pulse sequence echo time, the main magnetic field strength, and MRI-relevant structural properties of the tissue sample (via the constant A) as well as its baseline blood volume and dHb concentration.

In the more general case, where CMR_{O_2} is not constant, Eqn. 5.10 must be replaced with the following expression for normalized $[dHb]_v$, based on Eqn. 5.9:

$$\frac{[dHb]_v}{[dHb]_{v_0}} = \left(\frac{CMR_{O_2}}{CMR_{O_2}|_0}\right)\left(\frac{CBF_0}{CBF}\right). \tag{5.12}$$

This results in a modified form of Eqn. 5.11:

$$\frac{\Delta BOLD}{BOLD_0} = M\left(1 - \left(\frac{CMR_{O_2}}{CMR_{O_2}|_0}\right)^{\beta}\left(\frac{CBF}{CBF_0}\right)^{\alpha-\beta}\right). \tag{5.13}$$

The above expression can be used to generate a set of iso-CMR_{O_2} contours by plotting the BOLD signal as a function of CBF at different levels of oxygen consumption. This is illustrated in Fig. 5.1b, which shows iso-CMR_{O_2} curves plotted over a region of the BOLD-CBF plane using Eqn. 5.13.

Figure 5.1 shows the expected shape of the BOLD-CBF-CMR_{O_2} relationship given the values of α and β believed to apply in fMRI experiments. Since the horizontal scaling of the plot is based on experimentally determined parameter estimates, the BOLD and CBF increases observed in most fMRI experiments should be restricted to the linear regime of the relationship, where the iso-CMR_{O_2} contours are approximately straight and parallel. One of the goals of this study was to confirm these predictions experimentally by mapping out iso-CMR_{O_2} contours using graded hypercapnia and visual stimulation.

If the positions of one or more iso-CMR_{O_2} contours are known, then pairs of BOLD and CBF measurements can be translated into relative CMR_{O_2} increases by examining their position with respect to the contours. It is also possible to compute relative CMR_{O_2} increases from BOLD-CBF measurement pairs by solving Eqn. 5.13 for the oxygen consumption term, as in the method of

Davis *et al.* [51]:

$$\frac{\mathrm{CMR_{O_2}}}{\mathrm{CMR_{O_2}}|_0} = \left(1 - \frac{\left(\frac{\Delta \mathrm{BOLD}}{\Delta \mathrm{BOLD_0}}\right)}{M}\right)^{\frac{1}{\beta}} \left(\frac{\mathrm{CBF}}{\mathrm{CBF_0}}\right)^{1-\frac{\alpha}{\beta}}. \tag{5.14}$$

Davis' approach is equivalent to solving Eqn. 5.11 for M using BOLD and CBF measurements at a single level of hypercapnia and using Eqn. 5.14 to calculate $\mathrm{CMR_{O_2}}$ during activation. In the present study, M was estimated using an optimization procedure to fit Eqn. 5.11 to BOLD and CBF data acquired during graded hypercapnia. The symbol $\mathrm{C\hat{M}R_{O_2}} \equiv \frac{\mathrm{CMR_{O_2}}}{\mathrm{CMR_{O_2}}|_0}$ will be used as a concise notation for relative (baseline-normalized) $\mathrm{CMR_{O_2}}$ in the remainder of the text.

Measurement of relative $\mathrm{CMR_{O_2}}$ from MRI-based BOLD and CBF measurements can thus be summarized as a two part process. First, the positions of iso-$\mathrm{CMR_{O_2}}$ contours in the BOLD-CBF plane must be determined. Then the BOLD signal and perfusion increases during activation must be measured. It is sufficient to map out the baseline iso-$\mathrm{CMR_{O_2}}$ contour, since once M is known the other contours can be computed using Equation 5.13. Ideally, the baseline contour would be measured over a wide range of CBF values spanning both the linear region and the asymptotic portion at high perfusion levels. Unfortunately this is not possible using hypercapnia in human subjects, as tolerable levels of CO_2 produce relatively small ($\leq$20%) CBF increases.

Although direct measurements of M are not feasible in humans, this quantity can be estimated by fitting Eqn. 5.11 to graded hypercapnia data in the linear regime of the model. Furthermore, it can be shown that for small excursions in the BOLD-CBF plane, the spacing between iso-$\mathrm{CMR_{O_2}}$ contours depends primarily on the slope of the baseline iso-$\mathrm{CMR_{O_2}}$ contour near $\Delta\mathrm{CBF} = 0$. Because $\mathrm{CMR_{O_2}}$ increases as an approximately linear function of position over small patches of the BOLD-CBF plane, the spacing D between iso-$\mathrm{CMR_{O_2}}$ contours for a given step size $\Delta\mathrm{C\hat{M}R_{O_2}}$ is equal to $\frac{\Delta\mathrm{C\hat{M}R_{O_2}}}{|\vec{\nabla}\mathrm{C\hat{M}R_{O_2}}|}$ where $|\vec{\nabla}\mathrm{C\hat{M}R_{O_2}}|$ is used to denote the magnitude of the gradient vector of $\mathrm{C\hat{M}R_{O_2}}$ in the (normalized) BOLD-CBF plane. It can be shown that the gradient magnitude of

Eqn. 5.14 for small BOLD and CBF changes is given by

$$\lim_{\Delta BOLD,\Delta CBF\to 0} |\vec{\nabla}\hat{CMR}_{O_2}| = \left(1-\frac{\alpha}{\beta}\right)\frac{\sqrt{1+m^2}}{m} \simeq \left(1-\frac{\alpha}{\beta}\right)\frac{1}{m} \quad \text{for} \quad m \ll 1. \tag{5.15}$$

where m is the slope, in the linear region, of the BOLD vs. CBF relationship at constant baseline CMR_{O_2} (*e.g.* during a hypercapnia experiment). The spacing between iso-CMR_{O_2} contours for step size $\Delta\hat{CMR}_{O_2}$ is therefore given by

$$D \simeq \frac{m}{\left(1-\frac{\alpha}{\beta}\right)}\Delta\hat{CMR}_{O_2}. \tag{5.16}$$

Since β is greater than α by a factor of at least two, the denominator $(1-\frac{\alpha}{\beta})$ in the above expression is only weakly sensitive to changes in either parameter because the fraction $\frac{\alpha}{\beta}$ lies on the asymptotic tail of the reciprocal function. This means that if BOLD and CBF measurements during graded hypercapnia confirm a linear relationship between the two quantities for BOLD increases of up to a few percent, moderate uncertainty in the model parameters α and β is not likely to have a large effect on the accuracy of $\hat{CMR}_{O_2}$ calculations. However, when data are only available in the linear regime, the consequence of inaccurate values for α and β would be a large error in estimates of the asymptotic fractional BOLD signal increase M.

Methods

The main experimental objectives of this study were: 1) to verify that BOLD and CBF responses during graded hypercapnia (GHC) at different levels of visual stimulation (VS) followed iso-CMR_{O_2} contours predicted by the dHb dilution model; 2) to determine whether a fixed relationship between CBF and CMR_{O_2} applies during brain activation. In this section we describe the

experiments used to meet these objectives and give details regarding region of interest definition, hypercapnic modulation of CBF, visual stimulation, and MRI data acquisition.

Experiments

Each experiment consisted of a controlled comparison of the BOLD-CBF trajectories produced by two graded stimulus types, at four potency levels for each. A standardized experimental protocol was used in which BOLD and CBF responses were simultaneously measured and the different stimulation conditions interleaved in random order. Data were averaged over many subjects with different randomization orders, and baseline signal levels were sampled before and after each stimulation interval. This approach ensured that any sources of systematic bias were distributed uniformly across all baseline and activation conditions, permitting accurate isolation of signal modulation due to deliberate changes in experimental conditions. All relative signal changes in all experiments were referenced to the same baseline condition. To ensure that only physiological steady-state responses were included in percent change calculations, data acquired less than one minute after changes in stimulation state were excluded. The experimental protocol used for all experiments is outlined in Fig. 5.2, and the different experiments performed are summarized in Table 5.1. The main experiments are described in detail below, numbered as in Table 5.1. Stimulus types in each experiment are labelled A and B, corresponding to the notation used in Table 5.1 and Fig. 5.2a. Subjects (healthy volunteers) gave informed consent and the experimental protocol was approved by the Research Ethics Committee at the Montreal Neurological Institute.

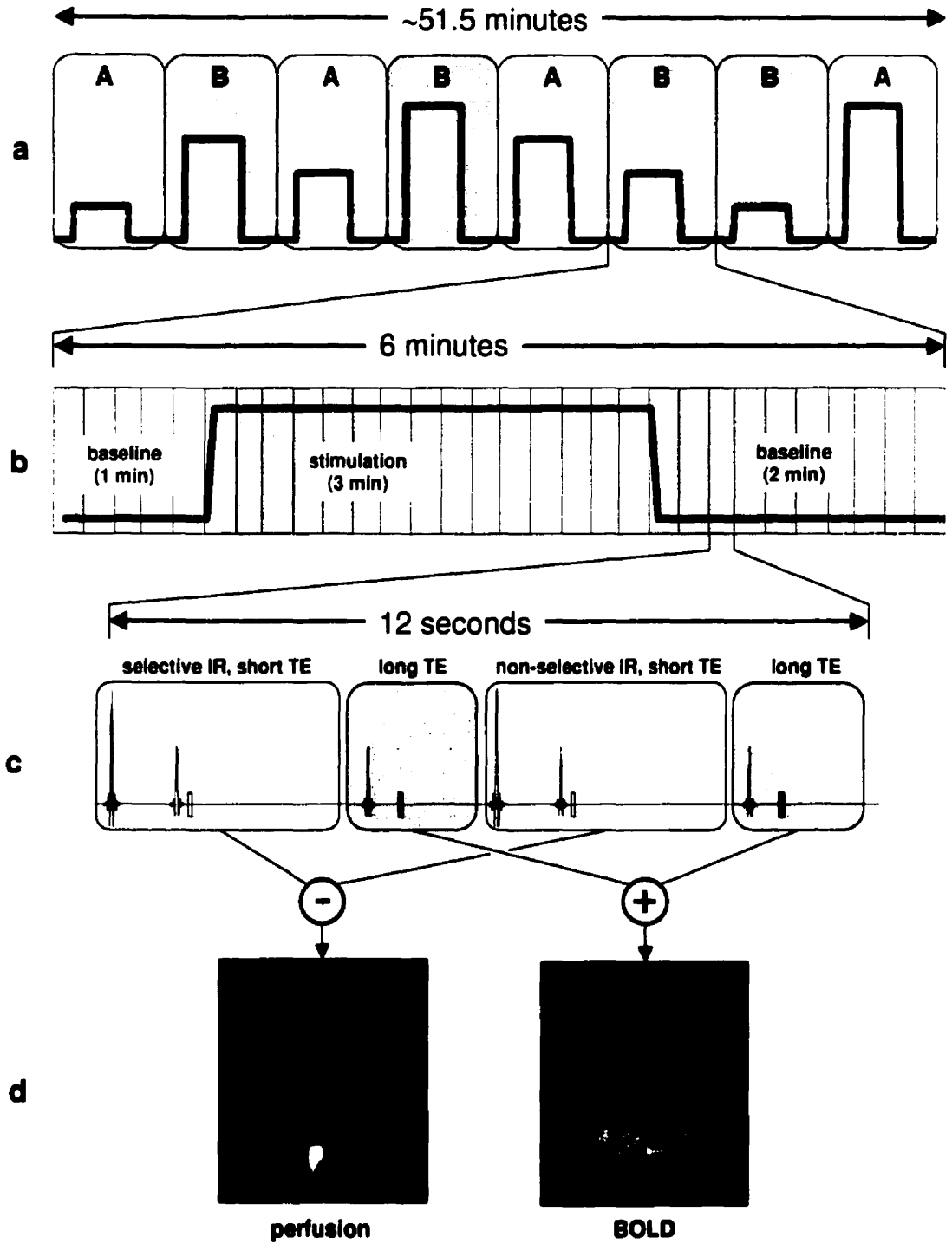

Figure 5.2: See caption next page

Fig. 5.2 (previous page). Experimental protocol used for all experiments. (a) Example of a randomized scanning session for a single subject. Sessions consisted of eight scanning runs during which responses to two stimulus types (A and B) at four potency levels each (indicated by height of square pulses) were determined. (b) Timeline of a single scanning run within a session. Each run contained one stimulation interval, indicated by the square pulse in the figure. Scanning runs produced 30 image pairs (rectangular blocks) comprised of one BOLD and one CBF image each. Image pairs shaded in grey (one minute post onset and cessation of stimulation plus first scan in run) were excluded in percent change calculations to ensure that time averaged data included only physiological and NMR steady states. (c) Interleaved MRI pulse sequence used to acquire BOLD/CBF image pairs. Scans 1 and 3 (white blocks) comprised a FAIR acquisition, while scans 2 and 4 (grey blocks) were T_2^*-weighted (long TE) acquisitions which were added to produce a single BOLD image overlapping in time with the perfusion image. (d) Examples of perfusion and BOLD images for a single subject.

List of Experiments

Experiment	Condition A		Condition B		N
	Stimulus	Parameter varied	Stimulus	Parameter varied	
1	graded hypercapnia (GHC)	% CO_2: 1.25 2.50 3.75 5.00	graded hypercapnia + 4Hz/25% radial checker-board (GHC+VS)	% CO_2: 1.25 2.50 3.75 5.00	12
2	graded hypercapnia (GHC)	% CO_2: 1.25 2.50 3.75 5.00	graded 4cpd squarewave grating (GVS)	% contrast: 20 40 60 80	12
3	graded uniform red field (GVS)	% saturation: 25 50 75 100	graded 4cpd squarewave grating (GVS)	% contrast: 20 40 60 80	12
4	graded 4Hz radial checker-board (GVS)	% contrast: 6.25 12.50 18.75 25.00	graded 4cpd squarewave grating (GVS)	% contrast: 20 40 60 80	12
5	graded 4Hz radial checker-board (GVS)	% contrast: 25 50 75 100	graded 4cpd squarewave grating (GVS)	% contrast: 20 40 60 80	1 (6 sessions)
6	graded 8Hz radial checker-board (GVS)	% contrast: 12.50 25.00 37.50 50.00	variable frequency 50% radial checker-board (GVS)	frequency (Hz): 2 4 6 8	6

Table 5.1:

Experiment #1: Iso-CMR_{O_2} contour mapping

In this experiment, the two stimulus types were: A) graded hypercapnia at visual baseline (GHC) and B) graded hypercapnia at a constant level of visual stimulation (GHC+VS). To compute iso-CMR_{O_2} contours, we fit Eqn. 5.11 to the GHC data by adjusting M. Next, we determined relative CMR_{O_2} increases during GHC+VS, at each CO_2 concentration, using Eqn. 5.14 and the GHC-derived M value. The iso-CMR_{O_2} contour for the average response during GHC+VS was then computed, using Eqn. 5.13, and plotted on the same axes as the measured data. The fit between the computed non-baseline iso-CMR_{O_2} contour and the experimentally determined BOLD-CBF points was assessed based on the RMS error between predicted and measured BOLD signals at the four CBF levels observed during GHC+VS.

The visual stimulus used in the GHC+VS condition was a radial checkerboard pattern containing both color (yellow/blue) and luminance contrast, with 30 spokes and 6.5 rings (counting from 0.5–10° eccentricity; defined as the angle from the center of the visual field) of equal radial thickness, modulated in a temporal squarewave at 4 Hz (all frequencies in this paper are specified as squarewave modulation frequencies; 4 Hz is equivalent to *eight* contrast reversals per second). A relatively low contrast of ~25% was used, to ensure closely spaced iso-CMR_{O_2} contours. A uniform grey field at the mean luminance of the checkerboard was presented throughout GHC scanning runs and used as the baseline in the GHC+VS runs. Twelve subjects participated in this experiment.

Experiment #2:

Comparison of graded visual and hypercapnic stimulation at matched perfusion levels

Here the stimulus types were: A) graded hypercapnia at visual baseline (GHC); and B) graded visual stimulation (GVS) at normocapnia. Contrast levels of the visual stimulus were adjusted

(based on pilot studies) to match, approximately, the GHC-induced perfusion increases. The visual stimulus used in this experiment was a 4 cycle per degree (cpd) black and white squarewave grating drifting across the visual field at one degree per second at systematically varied orientations. The baseline display was again a uniform grey field at the mean luminance of the stimulus. To ascertain whether graded CMR_{O_2} increases occurred during visual stimulation, the BOLD-CBF trajectory produced by GVS was compared to iso-CMR_{O_2} contours derived from the GHC data as described above. This experiment was performed on twelve subjects.

Experiment #3: Stimulus specificity experiment

In this experiment, the stimulus types were: A) GVS with the 4cpd squarewave grating used in experiment #2, and B) GVS using a red uniform field changed to isoluminant grey and back at 3 Hz. Stimulus potency was graded by varying color saturation of the red phase without changing the luminance. Psychophysical isoluminance between the red and grey phases was achieved by having subjects adjust the luminance of the grey phase to minimize apparent flashing of a 5–10° red annulus in a flicker photometry procedure [135] conducted in the scanner. The BOLD-CBF trajectories produced by the two stimulus types were then compared for evidence of stimulus-specific CBF/CMR_{O_2} coupling. Twelve subjects were included in this experiment.

Experiments #4–6:

Graded visual stimulation over extended perfusion range

In the preceding experiments, the visual stimuli used were adjusted to produce CBF responses that overlapped with the levels of perfusion observed during hypercapnia. To investigate CBF/CMR_{O_2} coupling at higher CBF levels, we conducted experiments with the radial checkerboard stimulus at higher contrasts and different reversal rates (contrast levels and frequencies used are summarized

in Table 5.1). The weaker 4cpd grating stimulus was included as a reference condition in Experiments #4 and 5, to determine whether iso-CMR_{O_2} contours derived from GHC in Experiment #2 could be applied to the other experiments. Relative CMR_{O_2} changes during GVS were computed using Eqn. 5.14 with the M value derived from the GHC experiment.

Region of interest definition

To satisfy the assumption of a homogeneous and uniformly responding tissue sample made in the model derivations given above, all measurements in this study included only tissue in primary visual cortex from 5–10° eccentricity. At the spatial resolution of our MRI measurements, V1 is likely to be relatively homogeneous in terms of its neuronal, metabolic, and MRI-relevant structural properties. The only significant difference between distinct volume elements in V1 is the portion of visual field represented. Blood volume fraction may vary somewhat between voxels, but the *average* CBV within V1 is likely to resemble whole-brain values for perfused cortex. There is some functional heterogeneity due to cortical magnification of central visual field, but restriction of our measurements to peripheral eccentricities minimized the significance of this effect.

Maps of visual field eccentricity and polar angle representation within V1 were generated for each subject in separate preliminary scanning sessions, using methods adapted from [92]. The BOLD acquisition used for retinotopic mapping was identical to the one used in interleaved BOLD and CBF measurements (described below), except that a 16 slice acquisition with isotropic 4 mm resolution was used. The V1 visual field maps were resampled onto the voxel grids used in subsequent experiments according to the computed transformation required to align high resolution anatomic images acquired at the beginning of each session [93]. Primary visual cortex was defined as being the retinotopically organized region within the left or right calcarine sulcus containing a mirror-image representation of the contralateral visual hemifield.

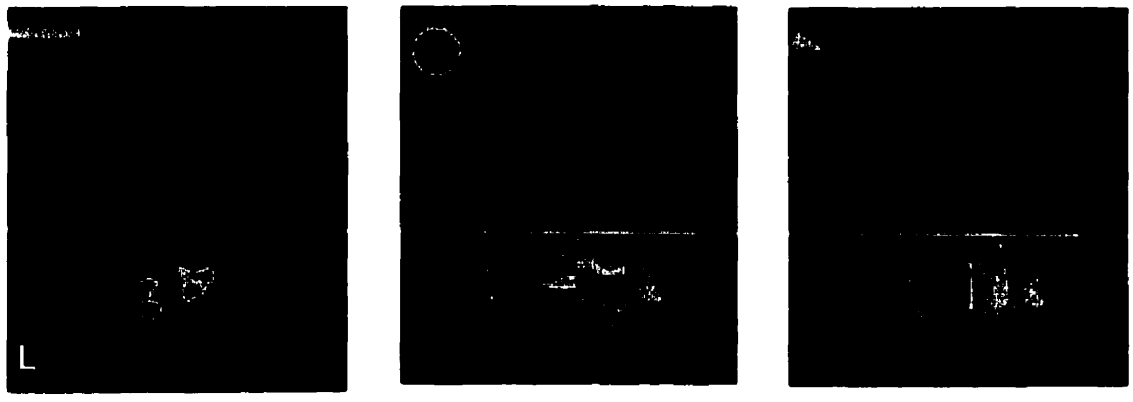

Figure 5.3: Example of resampled retinotopic mapping data, used for ROI delineation, from a single subject. (a) Normalized FFT modulus map showing retinotopic responses to a cyclically dilated visual stimulus. (b) Map of visual field eccentricity in retinotopically organized areas, overlaid on BOLD image acquired with interleaved sequence. Only the region receiving input from 5 to 10° (~green→yellow, inclusive, in eccentricity map) in each subject was included in percent change calculations. (c) Polar angle map for the same subject overlaid on BOLD image. Retinotopic representation of the contralateral visual hemifield within the left and right calcarine sulci was a criterion for V1 identification. Images, originally acquired on 64x64 matrices, are displayed here using interpolated oversampling for clarity.

The 5–10° eccentricity range was chosen because it lay within the region stimulated by the test patterns used in our experiments, while avoiding sagittal sinus interference and confluence of multiple visual areas that can occur near the fovea. Because all stimuli used in the present study encompassed this portion of the visual field, every voxel within the retinotopically defined region of interest (ROI) was guaranteed to contain activated neurons during stimulation. Hypercapnia can also be assumed to increase perfusion uniformly in all ROI voxels. Figure 5.3 shows examples of V1 retinotopic mapping used for ROI delineation. The average ROI volume was 1.7cc.

Hypercapnic modulation of CBF

Hypercapnic modulation of CBF was used in this study due to the relative rapidity with which perfusion can be manipulated, compared with infused agents such as L-arginine and acetazolamide. We induced graded hypercapnia by administering different concentrations of a CO_2/air mixture through a non-rebreathing face mask (Hudson RCI Model 1069) worn by subjects. The baseline condition was always inhalation of atmospheric composition medical air (~0% CO_2) delivered at 16L/min while attending to a standard baseline visual display (uniform grey field with attention/fixation task). Mild hypercapnic episodes were initiated during scanning runs by switching the breathing gas to a mixture of 5:21:74% CO_2:O_2:N_2 (BOC Canada Ltd.) and medical air. Different levels of hypercapnia (inhaled CO_2 concentrations of 1.25%, 2.5%, 3.75%, and 5%) were achieved by combining the pre-mixed CO_2/air preparation with medical air in a Y-connector and adjusting respective flow rates to achieve the desired proportions while maintaining a total flow rate of 16 L/min.

End-tidal CO_2, measured via a nasal cannula with monitoring aspirator (Normocap 200, Datex Inc.), increased by 5±1 mmHg on average (a 12% increase) during inhalation of the highest concentration CO_2 mixture. Subjects were instructed to breathe at a constant rate, which was easily maintained to within ± one breath per minute. Pulse rate and arterial oxygen saturation were also monitored (Oxygen/Pulse Monitor, Nonin Medical Inc.), and both remained constant throughout hypercapnia experiments. Sensations of respiratory stimulation were minimal in all subjects, even at the highest concentration of CO_2 (5%), and no undue discomfort was reported.

Visual Stimulation

Visual stimuli were generated in real time using a Silicon Graphics O_2 computer with locally developed OpenGL-based software. The RGB output was used to drive an LCD projector (NEC MT820) operating in 640x480 mode at 60Hz. Subjects viewed stimuli projected onto a screen mounted above their heads via a mirror while lying prone in the scanner. Stimulus presentation was automatically synchronized to data acquisition, and alertness and fixation were continually verified and logged in all subjects by requiring them to report, at three second intervals throughout all experiments, the orientation of a small, low contrast triangular fixation marker presented at the center of the display in a left-right orientation (◀ or ▶) that was varied at random intervals. Feedback was given via an MRI compatible two-button mouse.

All stimuli filled the entire rectangular area of the 640x480 pixel display (radial checkerboard stimuli were not restricted to a circular region), subtending 20x27° of visual field. The marker used in the attention/fixation task performed by subjects during all baseline and activation periods occupied the central ±0.5° of the display, but this region did not encroach on the 5–10° eccentricity range of V1 used for quantitative analysis.

The same baseline condition, consisting of a uniform grey field at the mean luminance of the stimulus patterns, was presented at the beginning and end of all scanning runs in this study, as indicated in Fig. 5.2b. Potency of the various stimuli was varied by changing their luminance contrast and, where applicable, chromatic saturation (by dilution with variable amounts of white). Luminance contrast was defined as the temporal luminance modulation amplitude expressed as a percent of the mean luminance, while chromatic saturation was defined to be the percent contribution of a 'pure' color (red, blue, or yellow) to the total luminance of a pixel. All stimuli converged in appearance to the uniform grey field as contrast/saturation approached zero.

MRI data acquisition

The BOLD signal and relative CBF were simultaneously recorded using an interleaved MRI pulse sequence consisting of a standard FAIR (flow sensitive alternating inversion recovery) acquisition [21] with a T_2^*-weighted (BOLD) EPI acquisition added after each of the two inversion-recovery acquisitions used in the basic FAIR technique (see Fig. 5.2c). The inversion time (TI) used in the FAIR acquisitions was 900ms, with an echo time (TE) of 20ms. A longer echo time of 50ms was used in the T_2^*-weighted BOLD acquisitions. Single-slice images were acquired on a 64x64 matrix with 5x5mm^2 in-plane voxel dimensions and 7mm slice thickness, along an oblique axial plane parallel to the calcarine sulcus. Both FAIR and BOLD images used identical EPI readouts, resulting in exact spatial correspondence between voxels in the two modalities. Excitation pulses were separated by a 3 second repetition time (TR), and audible gradient activity associated with the inversion prepulses of the FAIR acquisition was duplicated before the BOLD acquisitions, making the different phases of the sequence indistinguishable to the subjects. BOLD contamination of FAIR data and inflow effects in BOLD images, assessed by examination of non-selective IR images and comparison of BOLD images following selective vs. non-selective IR acquisitions, were found to be negligible.

Subjects were immobilized using a head-holder assembly incorporating a bite bar (not used in sessions including GHC), rigidly mounted ear cups which could be tightly clamped against the head, and a small saddle-shaped fixture pressed firmly into the subject's nose bridge. Subject motion was negligible using this apparatus. A receive-only circularly polarized surface coil was built into the head immobilization assembly, providing high signal-to-noise ratio MRI signals from the occipital lobe. All experiments were performed on a 1.5T Siemens Magnetom Vision MRI system.

Results

Experimental results are described here, numbered according to the order used in the Methods section and Table 5.1:

Experiment #1: Iso-CMR_{O_2} contour mapping

Average perfusion and BOLD signal changes in V1 during GHC and GHC+VS are shown in Figs. 5.4a and b. Addition of CO_2 to the subjects breathing air produced CBF and BOLD signal increases that were linearly proportional to concentration, and additive with visually evoked responses.

Figure 5.5a shows average responses during GHC and GHC+VS plotted in the BOLD-CBF plane. The value of M yielding the best fit between Eqn. 5.11 and the measured GHC data was 0.15. During GHC+VS, the average CMR_{O_2} increase was calculated to be 11.7±0.5%. The GHC+VS points lie precisely on the iso-CMR_{O_2} contour predicted using Eqn. 5.13 and the GHC-derived M value, with an RMS difference between predicted and measured BOLD signals of 0.15%.

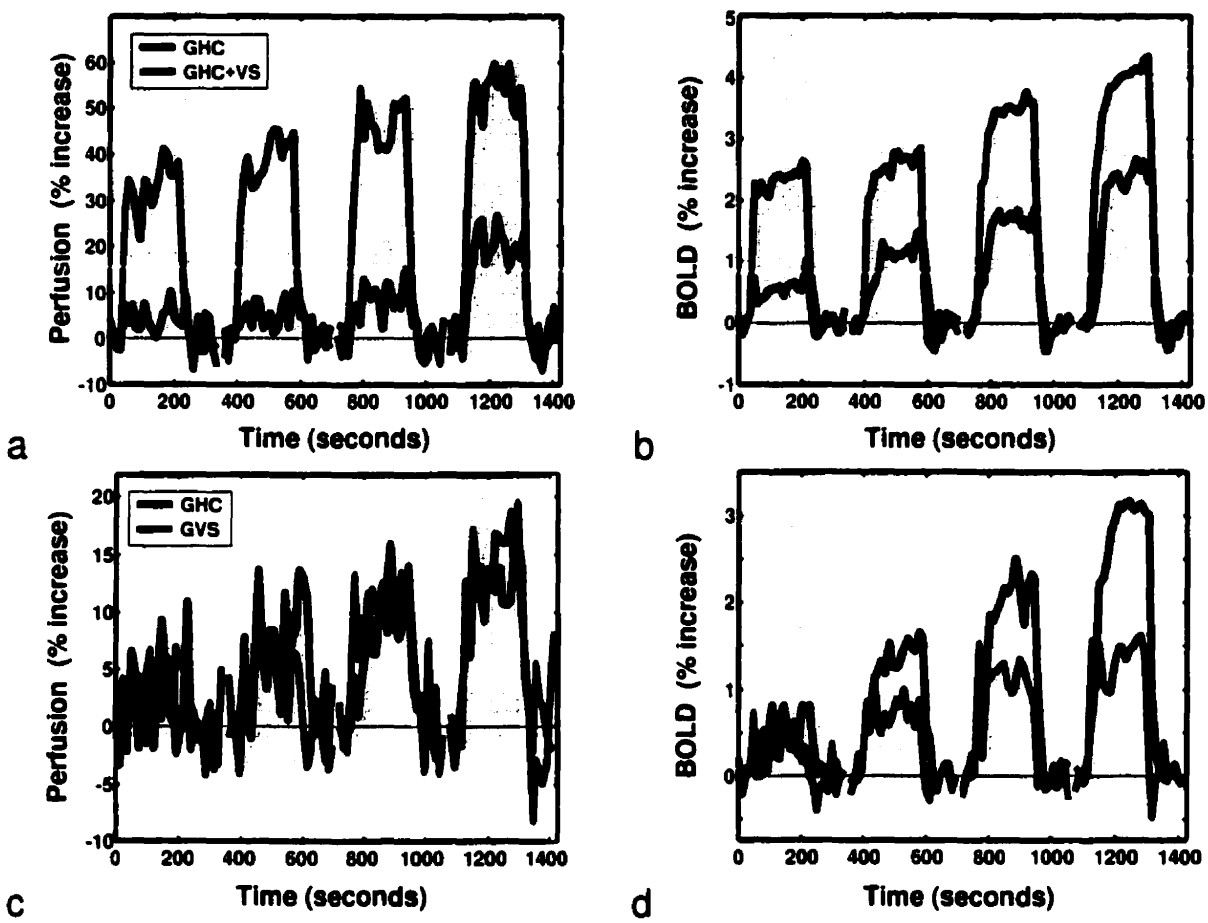

Figure 5.4: Perfusion and BOLD signals as a function of time during different combinations of graded hypercapnia and graded visual stimulation ($n = 12$ for all four graphs). Grey bars represent four successive periods of stimulation with increasing CO_2 concentration or visual stimulus contrast. (a) Relative CBF changes as a function of time during graded hypercapnia (GHC) with and without visual stimulation (±VS; blue and black curves, respectively). (b) Relative BOLD changes measured simultaneously with CBF data in (a). CBF and BOLD responses for visual stimulation and hypercapnia are additive. (c) Relative perfusion as a function of time measured during GHC (black curve) and graded visual stimulation (GVS; red curve) with contrasts adjusted to match hypercapnia-induced CBF increases. (d) BOLD signal as a function of time during perfusion increases shown in (c). BOLD signals during visual stimulation are significantly lower than those observed during hypercapnia at matched perfusion levels, revealing graded increases in oxygen consumption.

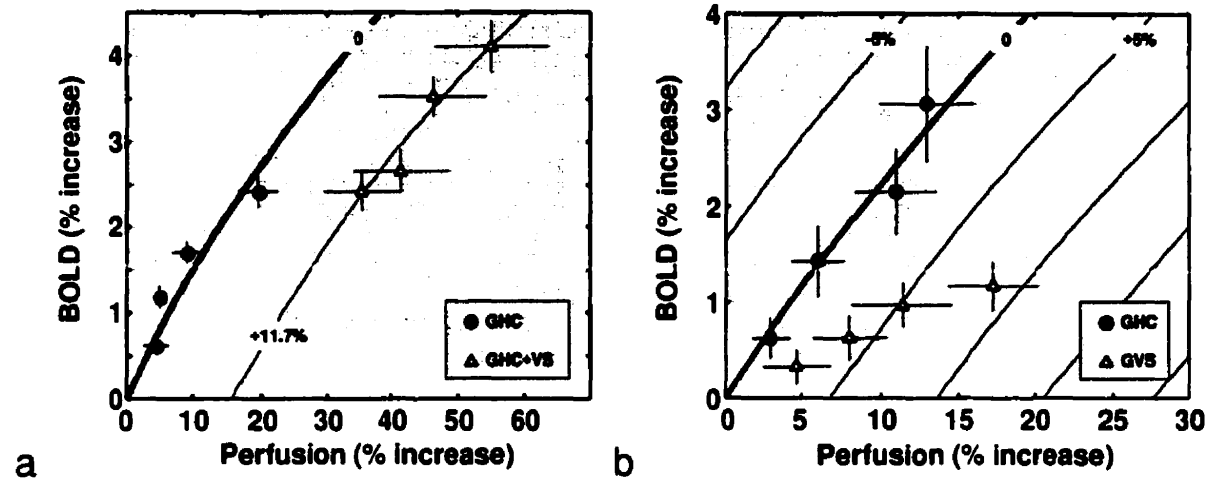

Figure 5.5: Maps of CMR_{O_2} on BOLD-CBF axes for primary visual cortex, with iso-CMR_{O_2} contours fit to hypercapnia data. The two stimulus types represented in each graph were randomly interleaved in single experimental sessions while BOLD and CBF responses were measured simultaneously (±SE; $n = 12$ for both experiments). (a) Average BOLD and CBF responses during graded hypercapnia (GHC) with and without visual stimulation (±VS; triangles and circles, respectively). The baseline iso-CMR_{O_2} contour ('0') was generated by fitting Eqn. 5.11 to the hypercapnia-only data (circles). The points measured during simultaneous hypercapnia and visual stimulation (GHC+VS) lie along a non-baseline contour predicted using Eqn. 5.13 with the M value estimated from the GHC-only data. (b) Average BOLD and CBF responses during graded hypercapnia (GHC; circles) and graded visual stimulation (GVS; triangles). As in (a), Eqn. 5.11 was fit to the graded hypercapnia data to produce the baseline iso-CMR_{O_2} contour and Eqn. 5.13 was used to generate non-baseline contours at 5% intervals. The data for graded visual stimulation can be seen to climb a gradient of CMR_{O_2} in the BOLD-CBF plane.

Experiment #2:

Comparison of graded visual and hypercapnic stimulation at matched perfusion levels

Figure 5.4c shows perfusion as a function of time during GHC and GVS at contrast levels adjusted to match the GHC-induced perfusion increases. The corresponding BOLD signals (Fig. 5.4d) reveal significant attenuation of the visually evoked responses compared with those produced by

hypercapnia. The degree of attenuation increased with perfusion, indicating graded CMR_{O_2} increases. Figure 5.5b shows the above data plotted on the BOLD-CBF plane. The visual stimulation data diverge from the baseline iso-CMR_{O_2} contour, and climb the CMR_{O_2} gradient. The M value providing the best fit of Eqn. 5.11 to the GHC data was 0.22.

Experiment #3: Stimulus specificity experiment

Figure 5.6 shows BOLD-CBF trajectories measured during GVS with the red uniform field and 4cpd grating. These were precisely co-linear, indicating that steady-state CBF:CMR_{O_2} coupling averaged over V1 does not vary for these stimuli.

#4–6: Graded visual stimulation over extended perfusion range

Slopes of the BOLD-CBF relationship were found to be similar for different visual stimuli and reproducible across sessions. All visual stimulation data fell in a single linear cluster in the BOLD-CBF plane, as shown in Fig. 5.7a, and responses observed by averaging multiple sessions in a single subject (Experiment #4 in Table 5.1) were co-linear with group average data.

Regions of the BOLD-CBF and CMR_{O_2}-CBF planes corresponding to relative CMR_{O_2}/CBF response ratios in the range 0.5 ± 0.1, shown as darker grey areas in each plot, include all visual stimulation responses observed in the present study. Slopes of the relative $\Delta\hat{CMR}_{O_2}$ vs. ΔCBF relationships are summarized in Fig. 5.7c.

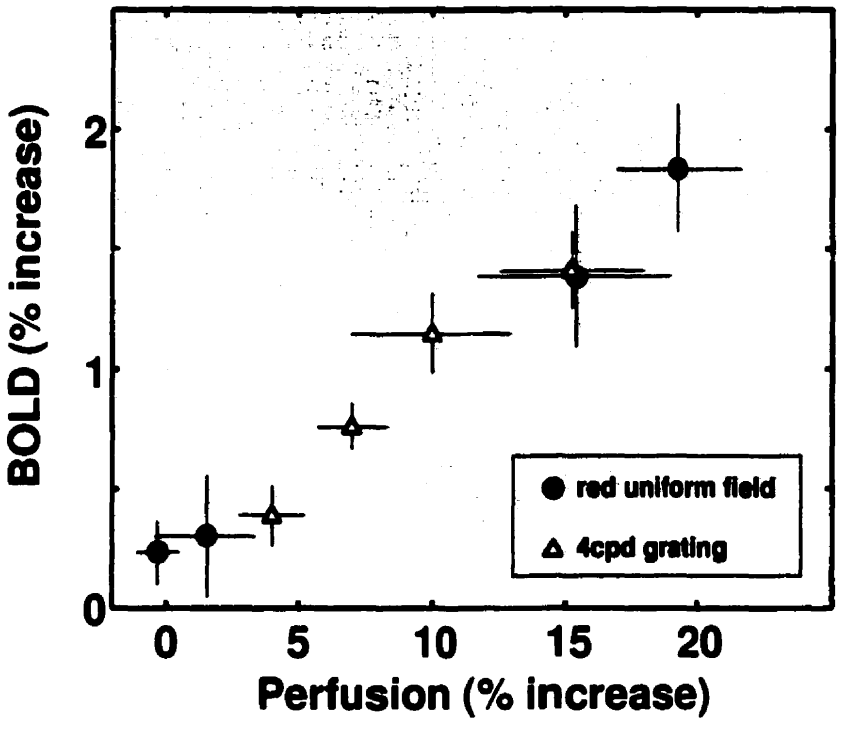

Figure 5.6: Steady-state BOLD vs. CBF relationships for two different visual stimuli. Data for visual stimulation with a color varying (red/isoluminant grey) uniform field (circles) and a high spatial frequency black and white grating (triangles) are precisely co-linear, indicating that CBF-CMR_{O_2} coupling was the same for both stimuli. Responses to the two stimulus types were randomly interleaved in the same experimental session while BOLD and CBF responses were measured simultaneously ($n = 12$).

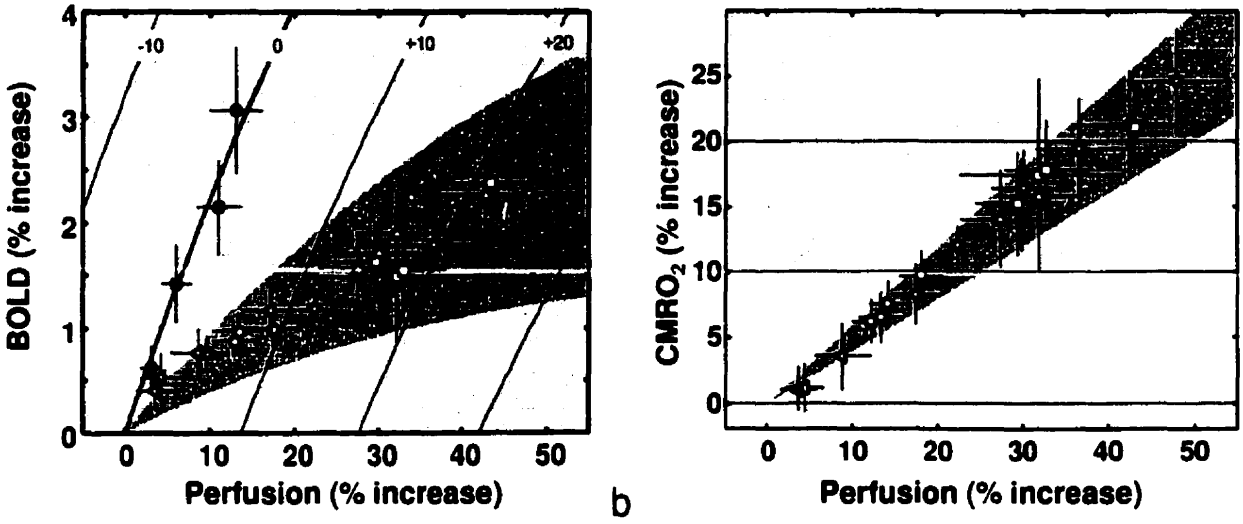

Symbol	Stimulus	$\frac{\Delta\%CMR_{O_2}}{\Delta\%CBF}$	subjects
•	hypercapnia (4 CO_2 concentrations)	0	12
◁	high spatial frequency black/white grating (4 contrast levels)	0.5±0.1	12
○	4Hz yellow/blue radial checkerboard (4 low contrast levels)	0.52±0.06	12
▽	4Hz yellow/blue radial checkerboard (4 high contrast levels)	0.52±0.04	1
△	8Hz yellow/blue radial checkerboard (4 contrast levels)	0.50±0.02	6
□	yellow/blue radial checkerboard (4 frequencies: 2, 4, 6, 8 Hz)	0.51±0.08	6

Figure 5.7: Coupling relationships between CBF and CMR_{O_2} during visual stimulation. Regions where $(\Delta CMR_{O_2}/CMR_{O_2}|_0)/(\Delta CBF/CBF_0) = 0.5 \pm 0.1$ are shown as the darker grey areas in both plots. (a) CMR_{O_2} map, derived from graded hypercapnia data (black circles), on BOLD-CBF axes. BOLD and CBF measurements during graded visual activation with different stimuli form a well defined linear cluster within the darkened region. (b) Relative CMR_{O_2} calculated using the BOLD-CBF data in (a) and Eqn. 5.14. The data reveal a strict Δ%CBF:Δ%CMR_{O_2} ratio of ~2:1.

Discussion

Measured iso-CMR_{O_2} contours were approximately linear and parallel, as predicted by the quantitative dHb dilution model, over the range of CBF changes expected during brain activation. Under such conditions, BOLD-CBF coordinates translate to CMR_{O_2} levels as a simple linear function of

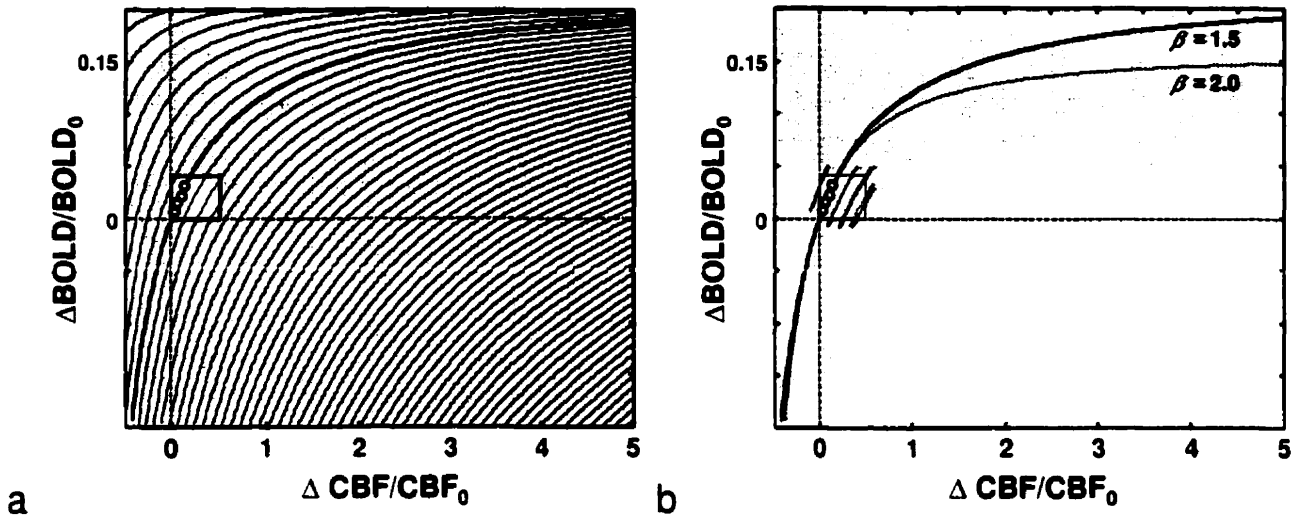

Figure 5.8: Extrapolation of experimentally determined iso-CMR_{O_2} contours. (a) CMR_{O_2} map over large range of CBF values, fit to GHC data (circles), with iso-CMR_{O_2} contours at 10% intervals. The domain/range included in Fig. 5.7a is shown as the white patch. The BOLD-CBF-CMR_{O_2} relationship is approximately linear over the physiologically relevant range of BOLD and CBF values. (b) Effect of different β estimates on fitted iso-CMR_{O_2} contours. The solid and dashed lines were both generated by fitting Eqn. 5.11 to graded hypercapnia data, but with respective β values of 1.5 and 2.0. While changing the model parameter caused a significant shift in the extrapolated asymptote, the positions of iso-CMR_{O_2} contours in the domain relevant for activation studies remained relatively constant. Sensitivity to α is similar.

position in the BOLD-CBF plane, whose gradient can be determined from the slope of the baseline iso-CMR_{O_2} contour. Robust measurements of relative CMR_{O_2} can thus be obtained from pairs of BOLD and CBF measurements, with little sensitivity to uncertainty in the model parameters α and β. Figure 5.8a shows a map of relative CMR_{O_2} over an extensive range of the BOLD-CBF plane, fit to data acquired during graded hypercapnia. It is clear from this illustration that brain activation studies occur in a domain where the BOLD signal, CBF, and CMR_{O_2} are related in an approximately linear fashion.

The BOLD-CBF-CMR_{O_2} relationship depicted in Fig. 5.8a is consistent with reports of in-

creased BOLD sensitivity to activation-induced CBF changes during hypocapnia in rats [136]. This behavior can be attributed to the increase in the slope, in the BOLD-CBF plane, of iso-CMR_{O_2} contours at lower CBF levels. During hypocapnia, baseline CBF is decreased, but activation-induced CBF increases combine additively with this effect in such a way that the *relative* CBF responses to stimuli are not affected [136–138]. This results in larger fractional BOLD signal changes during activation due to the increased partial derivative of the BOLD signal with respect to CBF at lower perfusion levels. Conversely, increased baseline CBF (due to hypercapnia and acetazolamide infusion) has been associated with reductions in the amplitude of activation-induced BOLD signal changes measured in human visual and motor cortices [122, 139]. While the experimental conditions of the present study produced responses within the linear domain of the quantitative dHb dilution model, the level of hypocapnia induced in the rat study of Hsu *et al.* [136] was fairly intense (a ~30% decrease in end-tidal CO_2) and the human studies of Bruhn and Bandettini [122, 139] combined maximal levels of vasodilatory and neuronal stimulation. It is therefore likely that the above trends are due to the decreasing slope of iso-CMR_{O_2} contours with increasing relative CBF depicted in Fig. 5.8a.

By matching perfusion levels during graded hypercapnia and graded visual stimulation, we obtained direct demonstrations of the effect of increased metabolic dHb production during brain activation. This constitutes truly model-independent evidence for graded increases in CMR_{O_2}, since experimental comparisons were controlled for CBF (and its correlate CBV) with no reliance on extrapolated relationships. Acceleration of oxidative metabolism reduced the visually evoked BOLD response to about one half of the value observed during equal perfusion increases produced by direct vasodilatory stimulation, equivalent to a reduction in the BOLD signal by ~1.5% of its average baseline value. Comparison of visually evoked steady-state BOLD responses during stronger stimulation with the extrapolated GHC-derived baseline iso-CMR_{O_2} contour reveals even

greater attenuation of up to 5.7% (of baseline). This is a significantly larger effect than the ~0.5% initial BOLD dip reported by Menon *et al.* using a 4 T MRI system [50], indicating that the transient dip does not reflect steady-state CMR_{O_2} levels but, more likely, a slight lag of the CBF response with respect to onset of CMR_{O_2} increases.

Our comparison of BOLD-CBF responses during visual activation with highly dissimilar stimuli revealed virtually indistinguishable BOLD:CBF ratios. The two stimuli used have been found, in previous autoradiographic studies [61, 106], to selectively activate either the blob or inter-blob systems of primate V1. Due to disparate levels of the aerobic metabolic enzyme cytochrome oxidase, it has been suggested that these tissues might exhibit different coupling between CBF and CMR_{O_2} [2, 3]. Although this idea has led to speculation that the BOLD-CBF relationships produced by the two types of stimulus may be characteristically different [67, 70, 140], our measurements (which are presumably superpositions of blob and inter-blob responses, since they were restricted to V1 tissue) indicate that they are not.

Visually-evoked BOLD-CBF relationships averaged across sufficient numbers of sessions were found to be reproducible, as shown by the well defined cluster in Fig. 5.7a. While previous reports have described large frequency-dependent variations in CBF-CMR_{O_2} coupling [141, 142], our data showed no evidence of such an effect. Estimates of the baseline BOLD signal attenuation M were found to be sensitive to slight differences in the measured slope of the baseline iso-CMR_{O_2} contour and to small variations in the model parameters α and β, as shown in Fig. 5.8b. Nevertheless, the positions of iso-CMR_{O_2} contours in the BOLD-CBF domain relevant to our experiments (the white patch in Fig. 5.8b) were relatively insensitive to these effects.

Analysis of our graded visual stimulation data revealed a consistent coupling ratio of ~2:1 for fractional changes in CBF and CMR_{O_2} during brain activation. Our MRI-based measurements of relative CBF and CMR_{O_2} increases during 4 Hz yellow/blue radial checkerboard stimulation at

maximal contrast (48±5% and 25±4%, respectively) are in reasonable agreement with values obtained by one of the authors (SM) using PET (68±15% and 25±15%) during an identical activation protocol [2]. In the same PET study, a (high-contrast) luminance varying uniform field stimulus flashing at 4Hz was found to produce CBF and CMR_{O_2} increases of 50±15% and 22±15%, which also corresponds well with our findings.

Davis *et al.* reported visually-evoked CBF and CMR_{O_2} increases of 45±4% and 16±1%, respectively, at a single level of visual stimulation [51]. In that study, single voxel CMR_{O_2} values were calculated in individual subjects and then averaged. Pooling the raw BOLD and CBF data over homogeneous regions of interest and multiple subjects, as done in the present study, is likely to produce more robust CMR_{O_2} estimates, given the non-linearity of the model and the extremely high variance of single-voxel MRI-based perfusion measurements. Our method of estimating M, based on fitting Eqn. 5.11 to graded hypercapnia data, is also likely to be more reliable. Nonetheless, the averaged results given in that report are in approximate agreement with our data at maximal stimulation.

Although the reports cited above yielded evidence of activation-induced CMR_{O_2} increases, the present study constitutes the first demonstration of a specific linear CBF/CMR_{O_2} coupling relationship maintained during a wide range of activation conditions. Theoretical analyses of oxygen delivery [49, 102, 110] have supported the assertion that relative CBF increases exceed fractional rises in CMR_{O_2} to accelerate diffusion limited delivery of oxygen across the blood-brain barrier. While the coupling relationship observed in our experiments is more linear than that predicted by Buxton *et al.* in [49], a recent extension of that model to include small variations in capillary diffusion area is consistent with linear coupling [110].

Since the emergence of fMRI, the BOLD effect has been attributed to the constancy of CMR_{O_2} across different activation states. Our results show that the BOLD phenomenon is more accu-

rately described as the outcome of strong competition between CMR_{O_2} and flow-related deoxyhemoglobin dilution during activation. Inspection of experimentally derived CMR_{O_2} maps on the BOLD-CBF plane reveals that the balance is a delicate one, with small shifts in CMR_{O_2} at a given level of CBF producing large changes in BOLD signal.

Acknowledgements

We thank Pamela Rabbitz for technical assistance. We are also grateful to Joe Mandeville for discussion and critical reading of the manuscript. This work was supported by the Killam Foundation, FRSQ (Canada), and the Whitaker Foundation.

Chapter 6:

Non-Linear BOLD and Perfusion Dynamics in Human V1

Preface

In the previous two papers, measures were taken to ensure that only steady-state signal changes were included in quantitative analyses. While this simplified analysis of the theoretical model involved and the physiological interpretation of our results, it avoids important questions that exist concerning the dynamic behavior of the BOLD fMRI signal. These issues were addressed in the present paper.

In this report, transient blood flow and oxygenation (BOLD) responses to changes in stimulation state in human visual cortex were examined in detail. We found that, for both the BOLD and flow signals, the step response in V1 depended strongly on the spatio-temporal pattern used as a stimulus, even when mean luminance was held constant and stimulus contrasts were adjusted to produce similar steady-state flow responses. We also discovered that the BOLD over and undershoot produced by certain patterns is associated with previously unknown transient signals in the perfusion response, which we were able to detect using novel averaging techniques. Finally, we used graded activation to demonstrate that BOLD signal transients are not necessarily correlated with steady-state flow levels. These results challenge current biomechanical models of BOLD contrast dynamics, and reveal important non-linear characteristics of fMRI signals.

Several additional multi-subject studies were performed specifically for this paper, and selected experiments included in the previous articles are also included in this chapter where they are subjected to different analyses with an emphasis on dynamic aspects of the measured signals.

Non-Linear BOLD and Perfusion Dynamics in Human V1

RICHARD D. HOGE, JEFF ATKINSON, BRAD GILL, GÉRARD R. CRELIER,

SEAN MARRETT*, AND G. BRUCE PIKE

McConnell Brain Imaging Centre, Montreal Neurological Institute, McGill University, Montreal, Quebec, Canada

**Nuclear Magnetic Resonance Center, Massachusetts General Hospital, Charlestown, Massachusetts, USA*

Submitted to NeuroImage: Nov. 1998

Key words: functional MRI; hemodynamics; visual cortex; psychophysiological habituation; contrast sensitivity; nonlinear dynamics

Abstract

Blood oxygenation level-dependent (BOLD) fMRI signals often exhibit pronounced over or undershoot upon changes in stimulation state. Current models postulate that this is due to the delayed onset or decay of perfusion-dependent attenuating responses such as increased cerebral blood volume or oxygen consumption, which are presumed to lag behind the rapid adjustment of blood flow rate to a new steady-state level. If this view is correct, then BOLD overshoot amplitudes in a specific tissue volume should be correlated with steady-state increases in perfusion, independent of stimulus type. To test this prediction, we simultaneously recorded BOLD and relative perfusion signals in primary visual cortex while inducing graded perfusion increases with three types of visual stimulus. Two of these, a diffuse chromatic stimulus with no luminance variation and a very high spatial frequency luminance grating, did not produce detectable BOLD overshoot (or undershoot) when an equal mean luminance baseline was used. Radial checkerboard stimuli, however, caused pronounced over/undershoot of both BOLD and perfusion signals even when temporal mean luminance was held constant and stimulus contrast was adjusted to produce the same steady-state blood flow increases evoked by the other stimuli. Transient amplitudes were generally uncorrelated with the steady-state responses, demonstrating non-linear BOLD signal dynamics in human V1. These findings suggest that, rather than a tissue-specific biomechanical or metabolic phenomenon, BOLD overshoot represents a stimulus-specific transient neural reaction that is distinct from the steady-state response to sustained stimulation.

Introduction

Sensitivity to blood oxygenation arises in T_2^*-weighted MR images of the brain because the local image intensity is generally subject to some degree of attenuation caused by deoxyhemoglobin (dHb), which is introduced into venous blood as tissues extract oxygen for aerobic metabolism. Increasing the perfusion rate in a tissue volume element generally leads to dilution of venous deoxyhemoglobin [118], reducing the tendency of the blood to attenuate the magnetic resonance signal. The resultant increase in signal intensity, referred to as the blood oxygenation level-dependent (BOLD) response, can be detected in images and forms the basis for functional MRI brain mapping [17, 25]. Increases in blood flow rate also cause distension of the highly compliant venous vessels, however, and the resultant increase in the fraction of tissue volume occupied by deoxygenated blood partially counteracts the diluting effect of the perfusion increase. If the rise in perfusion is due to heightened neuronal activity, then metabolic oxygen extraction may also increase, accelerating production of deoxyhemoglobin and further decreasing the BOLD signal. The net BOLD response is a balance between these three effects, with dHb dilution generally dominating to produce the commonly observed positive signal change with increased neuronal activity.

Temporal characteristics of the BOLD signal have attracted considerable interest recently, due to their physiological importance and implications for experimental design in fMRI. Although early work suggested that the BOLD response was a transient phenomenon [65, 66], subsequent studies have demonstrated that increases in neuronal activity produce positive changes in the steady-state BOLD signal [67–70] that can be sustained for arbitrarily long periods. This finding supported experimental design based on detection of steady-state changes, but current 'event-related' fMRI techniques [71] require a detailed understanding of dynamic aspects of the BOLD signal.

Two transient features are commonly observed in activation-induced BOLD responses: a large,

positive post-onset overshoot and a post-cessation negative undershoot of similar amplitude. Both events are followed by an exponential-like decay to a new steady-state level within approximately one minute. A small and brief ($\sim$1s) negative dip immediately following onset of stimulation is also occasionally observed [50, 72, 73], but this feature is much less prominent. All of these responses have attracted intense interest as evidence for various physiological phenomena, and several biophysical models incorporating them have recently been introduced. These theories are generally based on temporal lag between perfusion adjustment (which is assumed to occur within several seconds) and the more gradual onset of an attenuating response such as increased oxygen consumption [66, 74] or blood volume [75, 76].

Since it is also widely believed that CBV, CMR_{O_2}, and CBF are interrelated in a consistent (although incompletely characterized) manner in specific tissue volumes during steady-state brain activation [75, 76, 107, 110, 143], the amplitude of transient features of the BOLD signal should be strongly correlated with steady-state increases in cerebral blood flow. However, there is practically no data confirming this prediction. Most previous studies of BOLD signal dynamics in V1 have used a single maximal level of visual stimulation with darkness as a baseline condition (*e.g.* [67, 70]), making it difficult to rule out the possibility that transient signal features reflect neuronal responses to abrupt changes in mean luminance level. Furthermore, most prior studies comparing different stimuli have not included simultaneous recording of the CBF response. In experiments where CBF was monitored, perfusion signals were isolated either by extrapolating T_2^*-weighted data acquired at multiple echo times (TE's) to estimate the pure inflow contribution at TE=0, or by subtracting variably flow-sensitive images acquired several seconds apart [67]. Due to the constant subtraction ordering generally used to remove BOLD signal contributions, such techniques are subject to systematic error during periods of BOLD signal change (in a recent study of BOLD undershoot this limitation was overcome by averaging across multiple control acquisi-

tions [75]). Because such conditions apply during BOLD over or undershoot, the ability to detect these features in the perfusion signal is compromised. The sensitivity of MRI-based perfusion measurement techniques to transient CBF responses is further hampered by their very low signal-to-noise ratio (SNR), and the degree of signal averaging performed in prior work may have been inadequate to identify such features. These limitations are important, because current models of BOLD signal dynamics generally incorporate the assumption that there is no flow over/undershoot [74–76]. Although MRI-based studies have generally failed to detect such behavior, perfusion over and undershoots have been observed using Doppler ultrasound [144] and laser-Doppler flowmetry [145].

The goal of the present study was to address the above issues by inducing graded activation in a fixed cortical region of interest (ROI) while simultaneously recording its BOLD and relative CBF responses. Primary visual cortex (V1) was selected as a test system, since its well characterized retinotopic organization [146] and contrast sensitivity [147] can be exploited to control activation within an easily delineated tissue volume. The technique used to simultaneously measure BOLD and perfusion signals was designed to permit accurate monitoring of the relative CBF response during rapid changes in BOLD signal, and extensive signal averaging was performed to overcome the SNR limitations inherent to quantitative perfusion methods.

The main experimental objectives of this study were: 1) to determine whether different visual stimuli evoking similar steady-state perfusion increases produce equal BOLD over or undershoot, and 2) to assess the degree of correlation between over/undershoot amplitudes and steady-state CBF increases produced by a specific stimulus pattern at different contrast levels and temporal modulation frequencies.

General Methods

Overview

The study was organized into a series of experiments in which BOLD and perfusion time-courses were measured during graded activation with different stimuli. A standardized experimental protocol was used in which BOLD and CBF responses were simultaneously measured and the different stimulation conditions of a given experiment were interleaved in random order. Data were averaged over multiple subjects with different randomization orders, and baseline signal levels were sampled before and after each stimulation interval. This approach ensured that any sources of systematic bias were distributed uniformly across all baseline and activation conditions, permitting accurate isolation of signal modulation due to deliberate changes in experimental conditions. All relative signal changes in all experiments were referenced to the same baseline condition, and a fixed ROI was used for all conditions (retinotopic mapping procedures, described below, were performed to restrict ROI's to true striate cortex). In all experiments except one, a series of scanning runs of six minute duration each was performed, with stimulation state divided into the following three epochs: a one minute initial baseline period, a three minute stimulation interval, and a final two minute baseline period. In this section we first describe general procedures pertaining to the entire study, followed by specific methods and results for the two main sets of experiments.

MRI data acquisition

The BOLD signal and relative CBF were simultaneously recorded using an interleaved MRI pulse sequence consisting of a standard FAIR (flow sensitive alternating inversion recovery) acquisition [21, 148] with a T_2^*-weighted (BOLD) EPI acquisition added after each of the two inversion-recovery (IR) acquisitions used in the basic FAIR technique. The inversion time used in the FAIR

acquisitions was 900ms, with an echo time (TE) of 20ms. A longer echo time of 50ms was used in the T_2^*-weighted BOLD acquisitions. Images of relative perfusion were produced by subtracting non-selective from selective IR images, and T_2^*-weighted images were added in a pairwise fashion to produce a single BOLD image overlapping in time with each FAIR image. Excitation pulses were separated by a 3 second repetition time (TR), resulting in a temporal resolution of 12s per BOLD/perfusion image pair, which is sufficient for monitoring typical BOLD over and undershoots. All images were acquired on a single-slice 64x64 matrix with $5x5mm^2$ in-plane voxel dimensions and 7mm slice thickness, along an oblique axial plane parallel to the calcarine sulcus. Both FAIR and BOLD images used identical EPI readouts, resulting in exact spatial correspondence between voxels in the two modalities. Audible gradient activity associated with the inversion prepulses of the FAIR acquisition was duplicated before the BOLD acquisitions, making the different phases of the sequence indistinguishable to the subjects. BOLD contamination of FAIR data and inflow effects in BOLD images, assessed by examination of non-selective IR images and comparison of BOLD images following selective vs. non-selective IR acquisitions, were found to be negligible.

To permit accurate monitoring of perfusion during periods of BOLD signal change, half of the subjects in every experiment were imaged with the order of the selective and non-selective phases of the FAIR acquisition reversed. This canceled out any systematic bias due to changes in T_2^* in the interval between selective IR imaging and the non-selective control phase. The use of a short TE in the IR acquisitions further reduced the possibility of error due to BOLD contamination, and increased the SNR of perfusion measurements.

Subjects were immobilized using a head-holder assembly incorporating a bite bar, rigidly mounted ear cups which could be tightly clamped against the head, and a small saddle-shaped fixture pressed firmly into the subject's nose bridge. Subject motion was negligible using this ap-

paratus. A receive-only circularly polarized surface coil was built into the head immobilization assembly, providing high signal-to-noise ratio MRI signals from the occipital lobe. All experiments were performed on a 1.5T Siemens Magnetom Vision MRI system.

Visual stimulus presentation

Visual stimuli were generated in real time using a Silicon Graphics O_2 computer with locally developed OpenGL-based software. The RGB output was used to drive an LCD projector (NEC MT820) operating in 640x480 mode at 60Hz. Subjects viewed stimuli projected onto a screen mounted above their heads via a mirror while lying prone in the scanner. Stimulus presentation was automatically synchronized to data acquisition, and alertness and fixation were continually verified and logged in all subjects by requiring them to report, at three second intervals throughout all experiments, the orientation of a small, low contrast triangular fixation marker presented at the center of the display in a left-right orientation (◀ or ▶) that was varied at random intervals. Feedback was given via an MRI compatible two-button mouse.

All stimuli filled the entire rectangular area of the 640x480 pixel display (radial checkerboard stimuli were not restricted to a circular region), subtending 20x27° of visual field. The marker used in the attention/fixation task performed by subjects during all baseline and activation periods occupied the central ±0.5° of the display, but this region did not encroach on the 5–10° eccentricity range of V1 included in spatial averages.

Region of interest delineation

To avoid mixing of heterogeneous physiological and neuronal responses which might occur if we pooled multiple visual areas, all measurements in this study included only tissue in primary visual

cortex from 5–10° eccentricity. At the spatial resolution of our MRI measurements, V1 is likely to be relatively homogeneous in terms of its neuronal, metabolic, and MRI-relevant structural properties. The only significant difference between distinct volume elements in V1 is the portion of visual field represented. Blood volume fraction may vary somewhat between voxels, but the *average* CBV within V1 is likely to resemble whole-brain values for perfused cortex. There is some functional heterogeneity due to cortical magnification of central visual field, but restriction of our measurements to peripheral eccentricities minimized the significance of this effect.

Maps of visual field eccentricity and polar angle representation within V1 were generated for each subject in separate preliminary scanning sessions, using methods adapted from [92]. The BOLD acquisition used for retinotopic mapping was identical to the one used in interleaved BOLD and CBF measurements, except that a 16 slice acquisition with isotropic 4 mm resolution was used. The V1 visual field maps were resampled onto the voxel grids used in subsequent experiments according to the computed transformation required to align high resolution anatomic images acquired at the beginning of each session [93]. Primary visual cortex was defined as being the retinotopically organized region within the left or right calcarine sulcus containing a mirror-image representation of the contralateral visual hemifield.

The 5–10° eccentricity range was chosen because it lay within the region stimulated by the test patterns used in our experiments, while avoiding sagittal sinus interference and confluence of multiple visual areas that can occur near the foveal representation. Because all stimuli used in the present study encompassed this portion of the visual field, every voxel within the retinotopically defined region of interest (ROI) was guaranteed to contain activated neurons during stimulation. Figure 6.1 shows examples of V1 retinotopic mapping used for ROI delineation. Activation patterns produced by different conditions used in our experiments are also shown, illustrating that ROI's derived from activation maps would vary depending on stimulus type. The use of retino-

topic criteria for ROI delineation avoided this problem, and identified regions necessarily activated by all stimuli. The average ROI volume was 1.7cc.

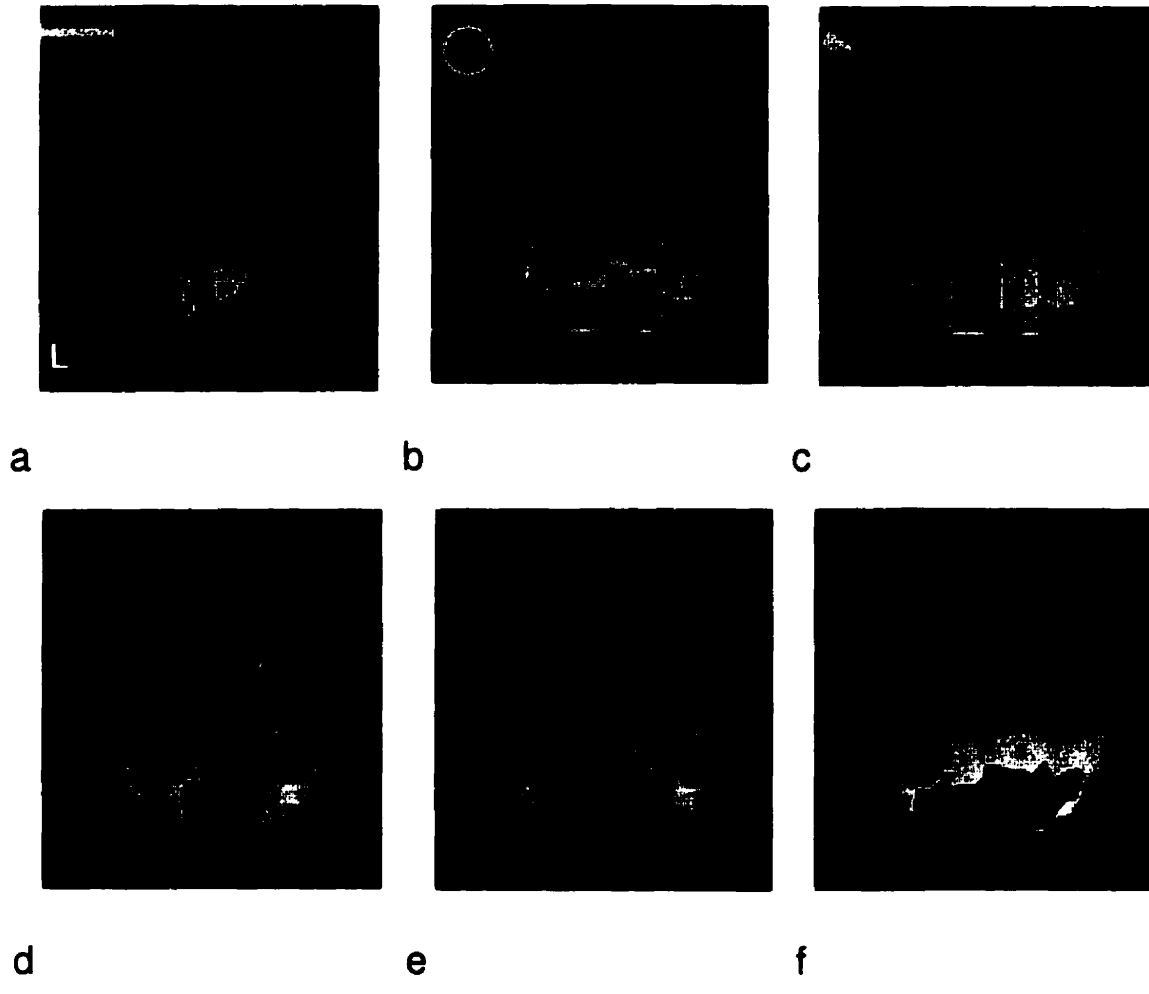

Figure 6.1: Example of resampled retinotopic mapping data (a–c), used for ROI delineation, from a single subject. Maps of activation produced by different experimental stimuli (d–f) in the same subject are included for comparison. (a) Normalized FFT modulus map [92] showing retinotopic responses to a cyclically dilated visual stimulus. (b) Map of visual field eccentricity in retinotopically organized areas, overlaid on BOLD image acquired with interleaved sequence. Only the region of V1 receiving input from 5 to 10° (~green→yellow, inclusive, in eccentricity map) in each subject was included in spatial averages. (c) Polar angle map for the same subject overlaid on BOLD image. Retinotopic representation of the contralateral visual hemifield within the left and right calcarine sulci was a criterion for V1 identification. (d) Regions activated by red/grey uniform field stimulus. (e) Regions activated by 4cpd drifting squarewave grating. (f) Regions activated by yellow/blue radial checkerboard. Extrastriate areas (*e.g.* V5,V3a) are activated in e and f, due to luminance modulation and apparent motion in the stimuli. Activation maps (d–f) were generated using Spearman rank-order correlation [149] and thresholded to 0.01 significance with correction for multiple comparisons.

The different experiments are summarized in Table 6.1 and described individually in detail in the following sections. Subjects (healthy volunteers) gave informed consent and the experimental protocol was approved by the Research Ethics Committee at the Montreal Neurological Institute. Volunteers had no known neurological abnormalities and possessed normal or corrected-to-normal vision.

Experiments #1–3: Stimulus specificity

Methods

In these experiments, BOLD and CBF time-courses were recorded during presentation of different visual stimuli to determine whether they all produced BOLD over or undershoot when similar steady-state perfusion increases were induced. The time averaged luminance of all points in the visual field was held constant, and each pattern was presented at four contrast levels. This allowed us to compare responses to different stimuli at overlapping levels of steady-state perfusion, eliminating the possibility that stimulus-specific transient BOLD features could be due to differences in CBF response magnitude. In each of these experiments, the results were averaged over twelve subjects.

Three different visual stimulus patterns were investigated. In Expt. #1, a red uniform field changing to isoluminant grey and back at 3 Hz was used. Experiment #2 employed a 4 cycle per degree (cpd) black and white squarewave grating drifting across the visual field at one degree per second at systematically varied orientations. In Expt. #3, we measured responses to a radial checkerboard pattern containing both color (yellow/blue) and luminance contrast, with 30 spokes and 6.5 rings (counting from 0.5–10° eccentricity; defined as the angle from the center of the visual field) of equal radial thickness, modulated in a temporal squarewave at 4 Hz (all frequencies in

Experiment	Stimulus	Parameter Values	N
1	graded uniform red field	% saturation: 25, 50, 75, 100	12
2	graded 4cpd squarewave grating	% contrast: 20, 40, 60, 80	12
3	graded 4Hz radial checker-board	% contrast: 6.25, 12.50, 18.75, 25.00	12
4	graded 4Hz radial checker-board	% contrast: 25, 50, 75, 100	1 (6 sessions)
5	variable frequency radial checker-board	frequency (Hz): 1.0, 1.5, 2.0, 2.5, 3.0, 4.0, 5.0, 8.0	10
6	radial checker-board with variable baseline luminance	baseline luminance (% of max.): 0, 25, 50, 75, 100	6
7	4Hz radial checker-board with variable temporal waveform	modulation waveform: square, triangular	6

Table 6.1: List of experiments.

this paper are specified as squarewave modulation frequencies; 4 Hz is equivalent to *eight* contrast reversals per second). The first two stimuli (the 4cpd grating and the red field) have been found, in previous autoradiographic studies [61, 106], to selectively activate either the blob or inter-blob systems of primate V1 (at peripheral eccentricities). Due to disparate levels of the aerobic metabolic enzyme cytochrome oxidase, it has been suggested that these tissues may exhibit different coupling between blood flow and oxygen consumption, leading to differences in their BOLD responses to stimulation [2, 3, 67, 70, 140]. The two patterns were therefore included, to test this prediction. The radial checkerboard pattern should be less selective, activating larger numbers of neurons, due to the combination of color and luminance contrast and inclusion of a broad range of spatial frequencies at multiple orientations.

Potency of the various stimuli was varied by changing their luminance contrast and, where applicable, chromatic saturation (by dilution with variable amounts of white) in linear steps. Luminance contrast was defined as the temporal luminance modulation amplitude expressed as a percent of the mean luminance, while chromatic saturation was defined to be the percent contribution of a 'pure' color (red, blue, or yellow) to the total luminance of a pixel. Potency of the yellow/blue radial checkerboard was graded by simultaneously changing both luminance contrast and color saturation, while that of the red uniform field was graded by varying color saturation of the red phase without changing its luminance. Psychophysical isoluminance between the red and grey phases was achieved by having subjects adjust the luminance of the grey phase to minimize apparent flashing of a 5–10° red annulus in a flicker photometry procedure [135] conducted in the scanner. Otherwise, all stimulus color and intensity values were calibrated to ensure contrast linearity using a single-channel optometer with photometric detector (Model S370, United Detector Technology). All stimuli converged in appearance to the uniform grey field baseline as contrast/saturation approached zero.

Results

Figure 6.2 shows average BOLD and perfusion signals recorded in V1 during presentation of the three stimulus types. In general, steady-state BOLD signal levels were strongly correlated with steady-state perfusion responses, and all responses reached maximal levels within a single sampling interval (12s). However, two signal characteristics varied systematically with stimulus type: the sensitivity of the response magnitude to reductions in stimulus contrast, and the shape of the temporal waveform. Responses to the red uniform field were found to decrease dramatically when the color saturation was reduced from 75% to 50%, while the response to the high spatial-frequency grating was an approximately linear function of contrast. Reducing the contrast of the radial checkerboard stimulus from 25% to 6.25% attenuated the response very little, however. The radial checkerboard was also unique in being the only stimulus to produce systematic BOLD over and undershoot upon onset and cessation of stimulation. Given the similarity of the checkerboard responses at different contrasts, we computed the average of the four time courses shown in Fig. 6.2e–f to further increase the SNR of the perfusion data. This resulted in the plots shown in Fig. 6.3, which show the strong overshoot of the BOLD signal, and reveal a detectable overshoot in the perfusion data (based on standard error of signal amplitudes averaged across subjects and runs). Exponential curves fit to the BOLD data indicated time constants of 25.8±5s for the overshoot and 19±3s for the undershoot. Exponential functions with the same time constants produced reasonable fits with the noisier perfusion data. Subjects reported that the checkerboard pattern produced a persistent (up to one minute) afterimage that was not noted with other patterns.

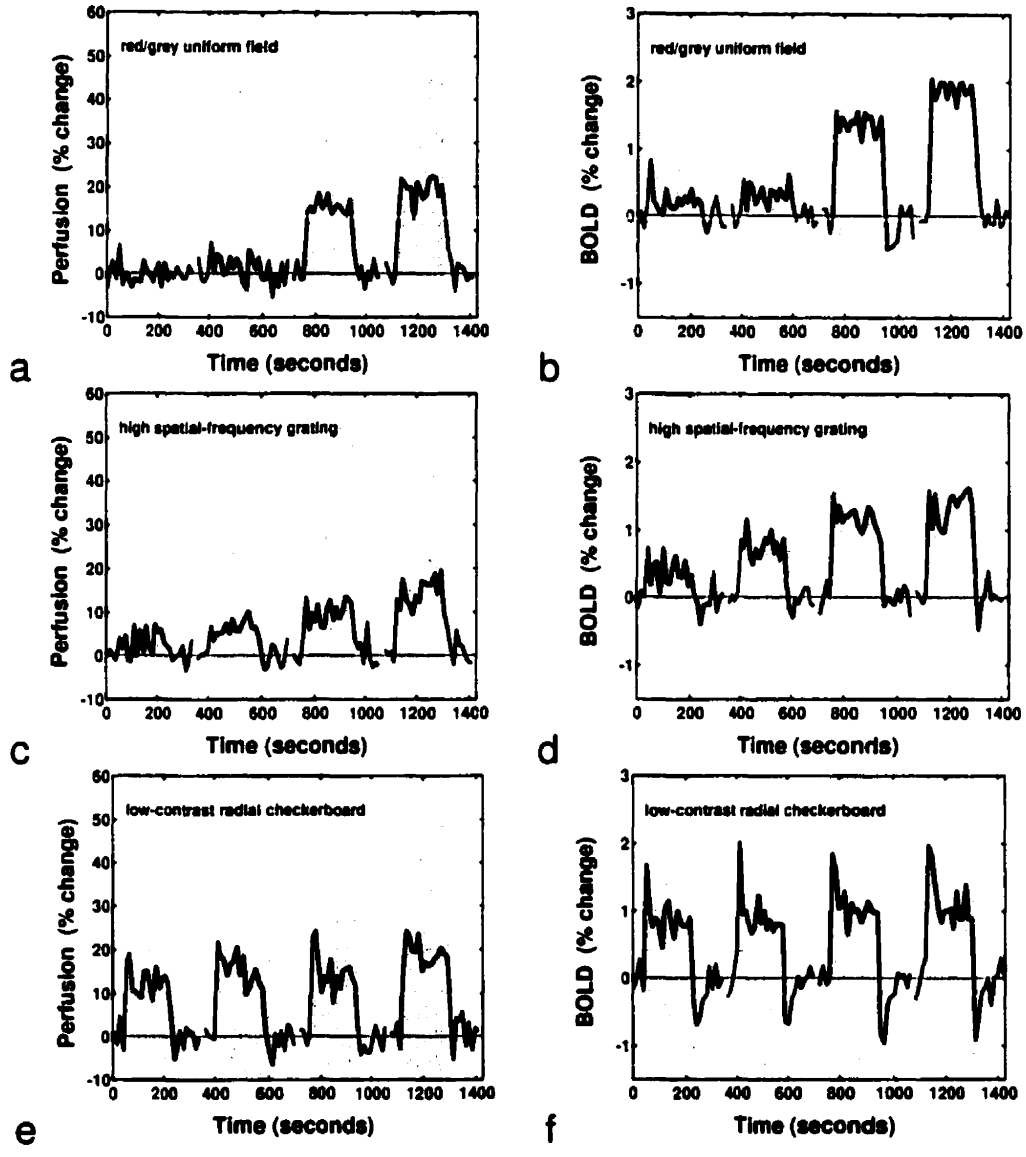

Figure 6.2: Simultaneously measured perfusion and BOLD signals from peripheral V1 during graded CBF increases induced with different stimuli (Expts. #1–3; $n = 12$). The four grey bars in each plot represent stimulation intervals of three minutes duration each. Contrasts were adjusted, in linear steps, to produce overlapping steady-state perfusion responses to all stimuli. (a–b) Red/grey uniform field. (c–d) High spatial-frequency black and white drifting grating. (e–f) Yellow/blue radial checkerboard. Only the radial checkerboard stimulus causes BOLD over and undershoot.

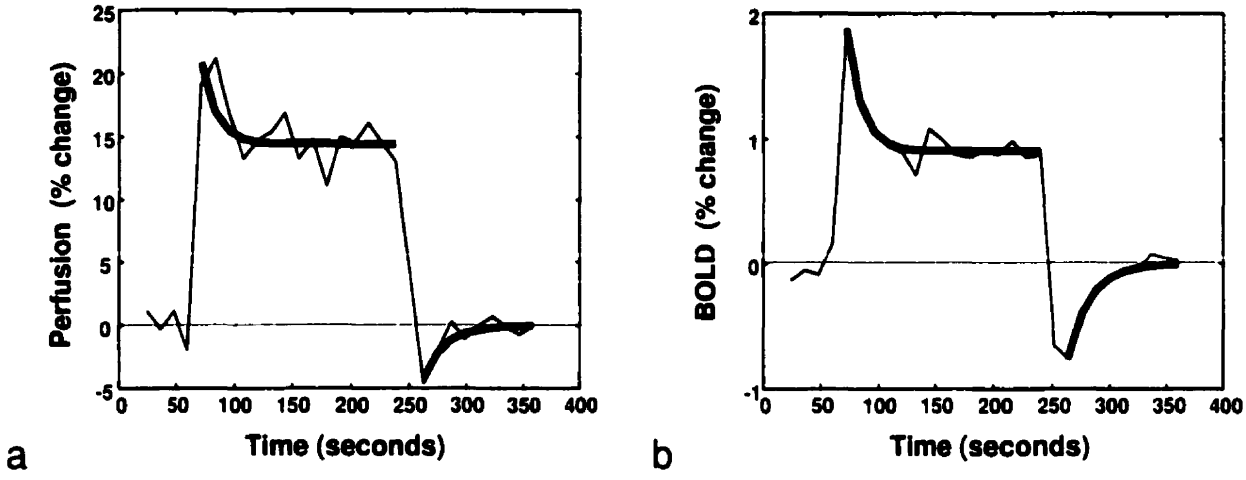

Figure 6.3: Simultaneously measured perfusion and BOLD responses in peripheral V1 to low-contrast radial checkerboard stimulation, averaged over 48 scanning runs (Expt. #3: 12 subjects with 4 runs each). Exponential curves fit to the BOLD and perfusion data are also shown (heavy lines; time constants for both plots are derived from BOLD data). (a) Perfusion data. An initial overshoot and post-stimulus undershoot are evident. (b) BOLD timecourse.

Experiments #3–7: Comparison of transient and steady-state responses

Methods

Because our stimulus specificity experiments revealed that the yellow/blue radial checkerboard stimulus produced consistent BOLD over and undershoot, the pattern was singled out for further examination in this section. In these experiments, a wide range of steady-state perfusion increases were produced by varying the temporal modulation frequency and contrast of the checkerboard pattern. We then assessed the degree of correlation between BOLD over and undershoot amplitudes and steady-state perfusion increases. Data from Expt. #3 were also included in this correlational analysis. In Expt. #4, the 4Hz radial checkerboard used in Expt. #3 was presented at higher contrast levels.

In Expt. #5, the radial checkerboard stimulus was again used, at constant maximal contrast and different temporal modulation frequencies ranging from 1–8 Hz. The scanning run duration and stimulus presentation timing used in this experiment were different from that used in all other experiments: a one minute baseline period was followed by seven minutes of stimulation. This study was averaged over ten subjects.

In Expt. #6, we investigated the effect of varying the luminance of the uniform field used as a baseline condition. The object was to determine whether an abrupt change in temporal mean luminance contributed to BOLD overshoots. All previous experiments used a grey field baseline at the temporal and spatial mean luminance of the experimental stimulus. In Expt. #6, five scanning runs were conducted, in random order in six subjects, with baseline luminance levels spanning the full range of the display hardware.

In a final experiment (#7), we sought to determine whether changing the temporal modulation waveform of the checkerboard stimulus from a squarewave to a function with a slower rise time would affect the response dynamics. The radial checkerboard stimulus was presented to six subjects with both square and triangular modulation waveforms at 4Hz, and a constant contrast amplitude of 75%.

In Expts. #3, 4, and 6, over and undershoot amplitudes were estimated by taking the inter-subject average of the first two time points immediately following changes in activation condition. Steady-state signal levels were computed by averaging responses in all subjects over the second and third minutes of stimulation. Baseline signal levels for percent change calculations were defined as the average signal level during the initial one minute baseline period and the final one minute steady-state baseline period. The first time point of each scanning run, comprising four EPI scans, was discarded to ensure stabilization of longitudinal magnetization. Transient amplitudes were then plotted as a function of steady-state perfusion level and, for Expt. #6, baseline luminance

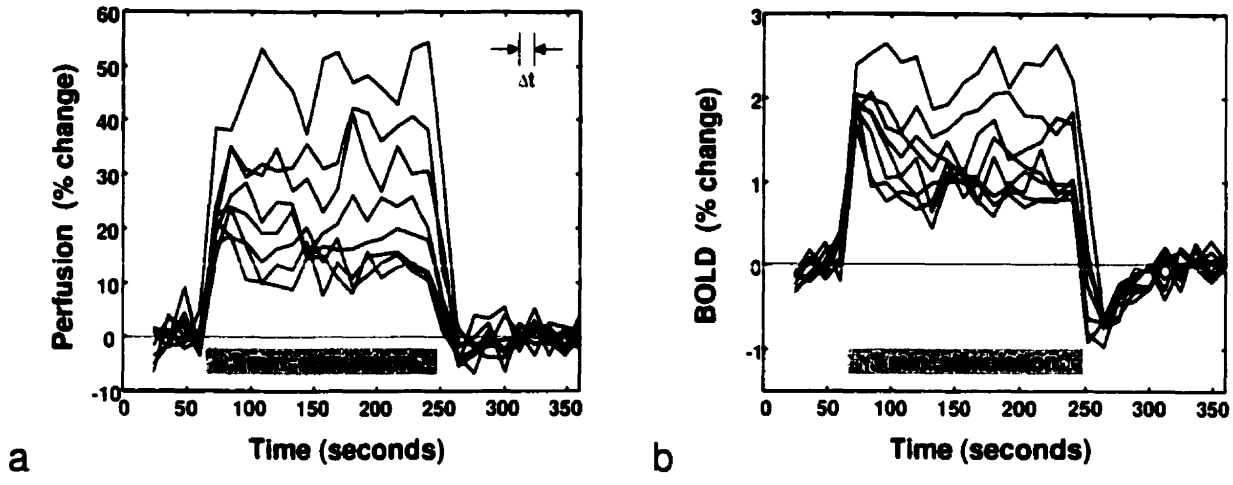

Figure 6.4: Perfusion and BOLD responses during radial checkerboard stimulation with graded contrasts (Expts. #3–4). The four largest responses are averages from multiple sessions using a single subject with higher contrast stimuli. (a) Perfusion responses. (b) BOLD responses. The overall variation in over/undershoot amplitude is smaller than that of the steady-state signals. Temporal sampling interval Δt is indicated in the perfusion plot.

level.

Results

Figure 6.4 shows perfusion and BOLD signals recorded in Experiments #3 and 4, plotted on the same axes. Variation of steady-state perfusion over a wide range, using 4Hz radial checkerboard stimulation at different contrasts, caused surprisingly little change in either over or undershoot magnitude. Changing the checkerboard modulation frequency at constant contrast produced an even more striking dissociation between the BOLD overshoot amplitude and steady-state CBF response, as shown in Fig. 6.5. At the lowest modulation frequency of 1Hz, a decline in the flow signal is clearly visible.

Varying the luminance level of the baseline uniform field display (Expt. #6) had no signifi-

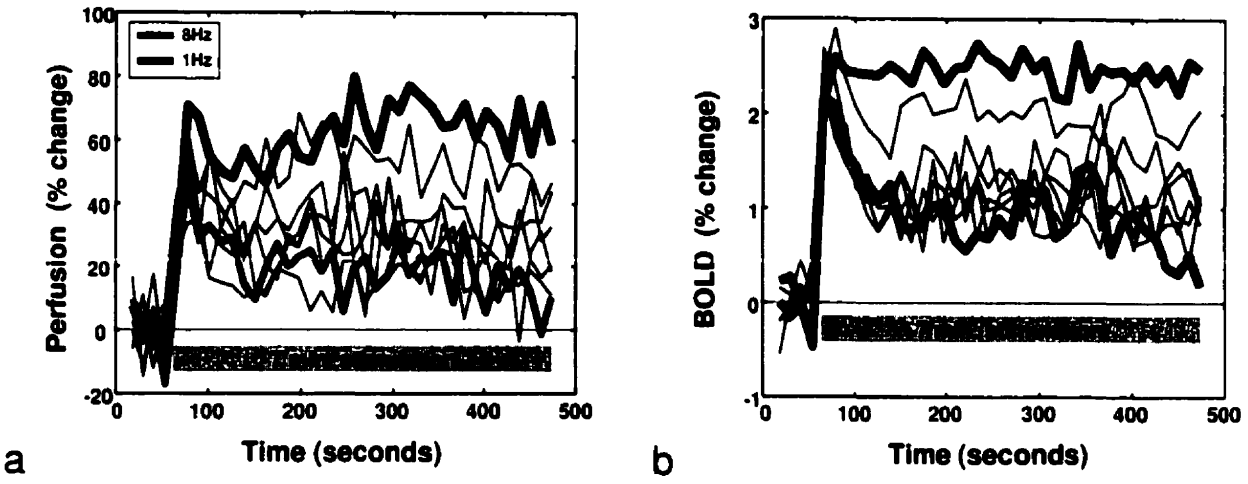

Figure 6.5: Perfusion and BOLD responses during sustained visual stimulation using a yellow/blue radial checkerboard at different modulation frequencies (Expt. #5). Responses for 1Hz and 8Hz stimulation are shown in red and blue, respectively. (a) Perfusion data. Note significant variation in steady-state responses. (b) Simultaneously measured BOLD signals. The amplitude of the initial overshoot is clearly similar for all frequencies, even though the steady-state responses vary greatly.

cant effect on either transient or steady-state radial checkerboard responses, which are plotted in Fig. 6.6a. Changing the temporal modulation waveform shape from square to triangular (Expt. #7) caused a small decrease in response magnitude, but did not change the shape of the BOLD step response, as shown in Fig. 6.6b.

Figure 6.7a shows transient and steady-state BOLD responses to 4Hz radial checkerboard stimulation (from Expts. #3 and 4) plotted as a function of steady-state perfusion. While steady-state BOLD signal increases appeared to be a linear function of the steady-state perfusion response, the BOLD undershoot amplitude exhibited almost no variation across a wide range of flow levels. The magnitude of the BOLD overshoot was a non-linear function of steady-state perfusion, with much of the correlation probably arising from inclusion of variable steady-state contributions in the sec-

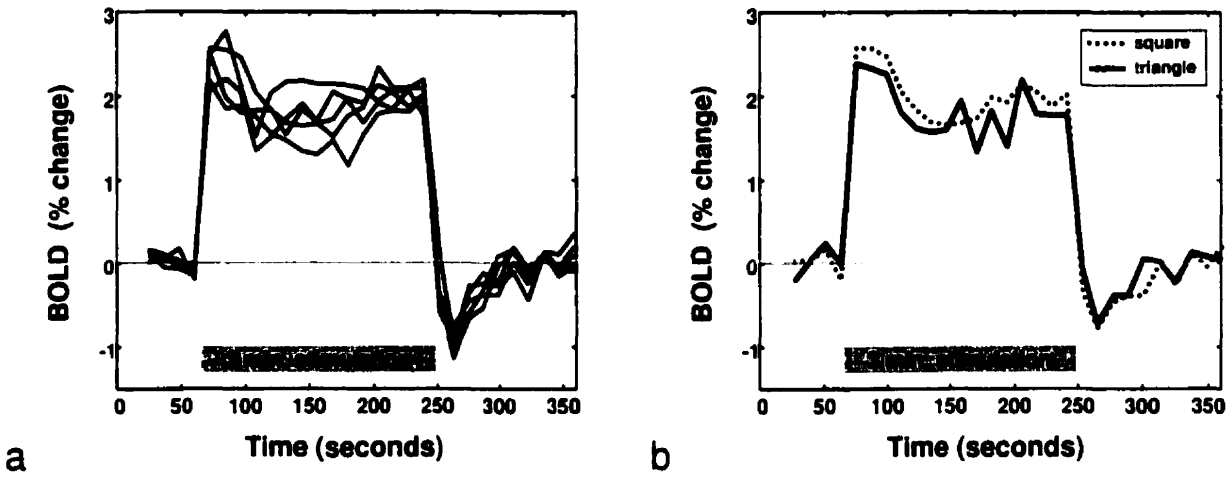

Figure 6.6: Effects of changing baseline luminance level and temporal modulation waveform. (a) BOLD signals for different baseline luminance levels (Expt. #6), revealing little effect. (b) BOLD signals for square and triangular modulation waveforms with identical amplitude and frequency (Expt. #7). The response magnitude is slightly reduced with triangle-wave stimulation, but the signal shape does not change.

ond time-point used for averaging (in a separate article, currently in press, we examine steady-state BOLD/CBF correlations in detail). Transient and steady-state responses are plotted as a function of baseline luminance in Fig. 6.7b, illustrating their lack of dependence on this parameter.

Discussion

BOLD signal transients in V1 appear to be neurally mediated responses that only arise when specific visual patterns are presented. Moreover, transient amplitudes were generally uncorrelated with changes in steady-state perfusion produced by viewing overshoot-evoking stimuli at different temporal modulation frequencies and contrast levels (although steady-state BOLD and CBF increases were strongly correlated). These observations are difficult to reconcile with biomechanical

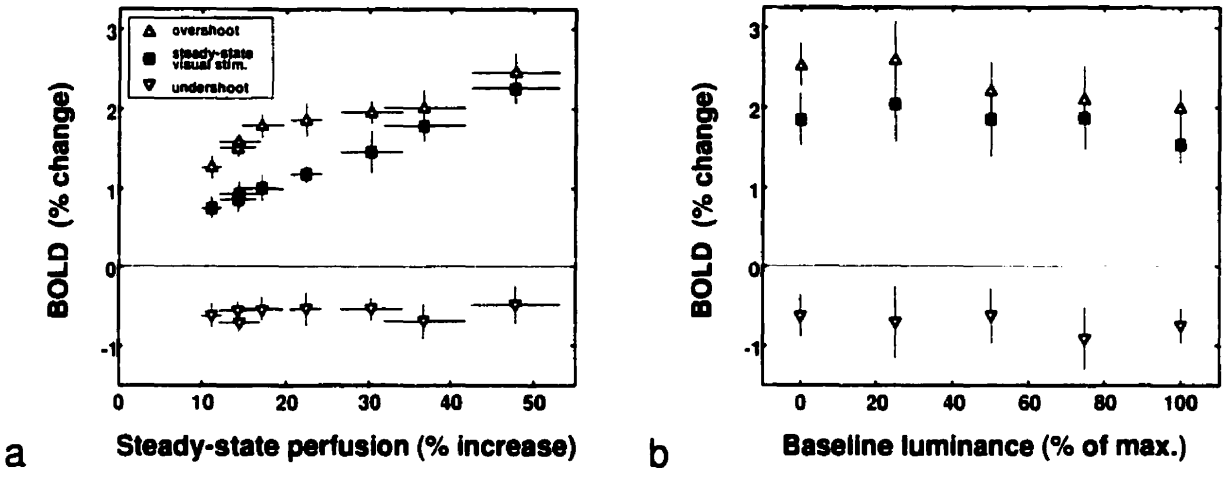

Figure 6.7: Scatter plots showing variations in radial checkerboard-induced over/undershoot magnitudes with different quantities. Plotted transient amplitudes are averages of first two time points following state transition, expressed as percent differences from baseline. (a) BOLD transient response magnitude as a function of steady-state perfusion increase (Expts #3–4). Undershoot amplitude is relatively constant in spite of large variations in steady-state CBF. Overshoot amplitude appears to be a non-linear function of steady-state perfusion. Steady-state BOLD signal is a linear function of steady-state CBF increase. (b) BOLD over/undershoot magnitude as a function of baseline luminance (Expt. #6). There is no significant variation in transient amplitude over a broad range of baseline luminance levels.

temporal-mismatch models, because such models predict that the over and undershoot amplitudes produced by a given perfusion increase should be constant in a fixed tissue volume, independent of stimulus type.

Because of the retinotopic criteria used to restrict spatial averages within subjects, the observed variations in step response cannot be attributed to tissue-specific differences. Every voxel in each ROI was certain to contain activated neurons, and hence undergo accelerated perfusion, during all stimulation conditions. Different voxels varied only in the portion of visual field represented, within a restricted peripheral range, so there was practically no possibility of inter-voxel variations

in response dynamics.

While it is beyond the scope of this paper to derive a detailed neural model explaining the observed behavior, we can interpret our results in terms of multiple neuronal systems, distributed within primary visual cortex, that are individually attuned to particular spatial and temporal characteristics of visual input. The unique transient responses associated with radial checkerboard stimulation could be explained in terms of systems that are unable to detect diffuse isoluminant stimuli or very high spatial-frequency patterns. This notion is supported by the distinctively high contrast sensitivity to this pattern in V1, which is characteristic of the color-insensitive, low-acuity magnocellular visual pathway [62]. The overshoot observed at the onset of checkerboard stimulation could be produced by temporary activity in a specific sub-population of neurons with extremely high contrast sensitivity and subject to gradually increasing inhibitory feedback. Persistence of the inhibitory influence following stimulus cessation could produce the observed undershoot. While this hypothetical mechanism is superficially similar to the temporal-mismatch biomechanical/metabolic models mentioned above, such a neuronal sub-system could, more plausibly, be completely independent of other visual pathways capable of sustained activity during continuous stimulation.

The current prevalence of models describing BOLD overshoot as a general, mechanistic phenomenon can probably be attributed partly to the popularity of dark baseline conditions and checkerboard stimuli in studies of BOLD contrast mechanisms [66, 67, 70, 74, 150–154]. Patterns similar to the checkerboard used in our study have been favored due to their compatibility with the modest resolution of available display hardware, the known potency of high luminance-contrast stimuli, and the belief that many orientation-selective cells will be concurrently stimulated. The radial checkerboard was indeed found to be a potent stimulus, producing much larger steady-state responses at maximal contrast (approximately double the perfusion increase) than more pathway-

specific input such as the red field and high spatial-frequency grating. However, the prominent transient features observed in checkerboard-evoked BOLD signals were found to be atypical responses that were not produced by other patterns, illustrating the risks inherent in generalizing results obtained with a specific stimulus. Although we found that neither the transient nor steady-state responses associated with radial checkerboard stimulation depend on baseline luminance levels, this is probably not the case with diffuse stimuli. Abrupt increases in the luminance of a uniform field have been shown to produce a transient BOLD response followed by a decay to baseline [67], suggesting that previous observations of overshoot with diffuse stimuli [70] may have been due to the use of a dark baseline.

Temporal-mismatch models of BOLD overshoot have generally incorporated the assumption, commonly accepted as axiomatic, that perfusion responses re-stabilize within several seconds in an approximately trapezoidal step response. Our data indicate that, on the contrary, a perfusion overshoot underlies BOLD transient responses. The extremely low signal-to-noise ratio of MRI-based perfusion measurements combined with insufficient signal averaging and the potential inaccuracy of conventional spin-labelling techniques during non-steady-state conditions are probably the reasons why this feature was not observed in previous studies. However, using 48 signal averages and our order-alternated FAIR method, we obtained results that were in qualitative agreement with previous laser and ultrasound-based Doppler flow studies [144, 145].

A number of recent studies have demonstrated approximately linear behavior in BOLD fMRI responses [71, 80]. When visual stimulus contrast was modulated using a step function in our study, however, the shape of the response waveform varied significantly depending both on the spatio-temporal pattern used as a signal carrier and on the amplitude of the input. While this clearly violates the basic requirement that a linear time-invariant system have a unique step response function, it does not necessarily imply that fMRI techniques such as event-related averag-

ing are inherently flawed. The non-linearities involved are predominantly neuronal, and may be less severe when very short, randomly spaced stimulus presentations are used. Our results do indicate, however, that measurements of the BOLD response (and any other index of neuronal activity) as a function of a stimulus parameter may depend strongly on the recording interval. A BOLD contrast-response curve derived from 500ms presentations of our yellow/blue radial checkerboard stimulus in an event-related fMRI study would presumably be very different from one based on steady-state responses. This does not reflect a deficiency in either approach, but rather the ability of each to capture a specific phase of the neuronal response.

Acknowledgements

This work was supported by the Killam Foundation, FRSQ (Canada), and the Whitaker Foundation.

Chapter 7: Summary and Conclusions

In this thesis a new, non-invasive, MRI based methodology for *in vivo* measurement of CBF and CMR_{O_2} was introduced. Specific technical contributions include: an interleaved perfusion and oxygenation-sensitive MRI pulse sequence permitting simultaneous measurement of these quantities with high SNR; hardware and software for fMRI experiment automation and stimulus generation; apparatus for subject immobilization, gas inhalation, and visual stimulus presentation during MRI scanning; and novel experimental protocols such as perfusion matching using inhaled CO_2 for isolation of metabolic effects in oxygenation-sensitive fMRI. These tools permitted experimental validation of a model describing BOLD signal dependence on CBF and CMR_{O_2}, which was used in conjunction with a new BOLD signal calibration approach (based on fitting the model to graded hypercapnia data) to measure CMR_{O_2}. A novel graphical formalism for interpreting simultaneously acquired BOLD and perfusion data in terms of iso-CMR_{O_2} contours on the BOLD-CBF plane was introduced, providing a powerful conceptual framework for understanding the relationship between these parameters.

The predictive model presented in Chapter 5 was strongly supported by the iso-CMR_{O_2} mapping experiment described in that paper, and model-derived measurements of activation-induced CMR_{O_2} increases were in close agreement with measurements performed under identical activation conditions using the quantitative gold standard of PET imaging [2]. This work establishes a

powerful new tool to probe the metabolic physiology and pathophysiology of the human brain.

A particularly significant finding made possible by the developments described in this thesis was the determination of a specific linear ~2:1 coupling relationship between relative changes in cerebral blood flow and oxygen consumption produced by graded activation in a specific cortical structure (Chapter 4). Previous studies attempting to determine a relationship between these quantities used a single level of stimulation and compared responses in different brain regions that responded variably to the same experimental condition [44], an approach which does not depict dynamic regulatory relationships. Even when responses have been restricted to specific regions of interest, most previous studies of brain activation physiology [42, 50, 51, 66, 67, 69, 70, 155, 156] have only employed a single level of stimulation and pooled all brain regions activated by the experimental stimulus. For visual activation with typical stimuli (contrast reversing radial checkerboards), this approach virtually assures that the spatially averaged responses will include multiple visual areas that may differ considerably in their neuronal, metabolic, and MRI-relevant structural properties. Furthermore, in functional MRI studies this approach may lead to ROI's that are biased towards voxels with high blood volume fractions, since these tend to produce more significant signal changes. These factors complicate interpretation of the observed responses, since the characteristics of different regions may vary and their relative contributions to spatially averaged signals may change during graded activation.

In the present study, the spatial specificity of measurements, and hence their physiological interpretability, were greatly enhanced by the use of retinotopic mapping procedures to identify primary visual cortex. This region is probably the best characterized of all brain systems in terms of its structural, physiological, and information processing properties. By studying different neuronal systems distributed within this well-delineated cortical region, in particular those with different enzymatic capacities for aerobic metabolism (the blob and interblob systems), the general

applicability of the BOLD fMRI contrast mechanism was tested under conditions which could quite reasonably be expected to challenge it. This constitutes an extremely important evaluation of the BOLD contrast method of functional imaging. The experiments described in this thesis could have revealed a fundamental limitation of BOLD fMRI (if activation of specific neuronal sub-populations was undetectable due to special metabolic properties), but instead showed that there is little variation in CBF/CMR_{O_2} coupling for different stimulus types in human visual cortex, considerably strengthening justification for the use of BOLD contrast as a general marker for brain activation. These findings represent the first direct experimental evidence in humans of a specific regulatory relationship between cerebral blood flow and oxygen consumption, and provide an unprecedented view of variable energy utilization by neurons.

In Chapter 6, important non-linear characteristics of BOLD fMRI signals arising from primary visual cortex were demonstrated, revealing behavior that challenges current biomechanical models of BOLD contrast dynamics. The detailed investigation of stimulus parameter effects given in this paper yielded results that contribute significantly to the reconciliation of conflicting findings in previous studies. For example, by changing the temporal modulation frequency of a radial checkerboard stimulus from 8 contrast reversals per second to 8 squarewave cycles per second (both frequency definitions have commonly been used without explicit specification), we observed a progression from the overshoot and decay behavior described by Frahm *et al.* [66] to the stable BOLD response reported by Bandettini *et al.* [67]. Overall, the results presented in Chapter 6 indicate that BOLD overshoot and undershoot probably reflect transient neural reactions to specific transitions in stimulation state, and may represent processes completely unrelated to steady-state processing of sustained visual input. This distinction has important implications for the design and interpretation of event-related fMRI protocols, which may lead to observation of different stimulus parameter-dependence than steady-state paradigms.

From the studies described in this dissertation, a number of topics emerge as particularly attractive for future investigation. More rigorous cross-modality validation studies using both fMRI and PET to measure changes in cerebral blood flow and oxygen uptake, in a single group of subjects, using the graded activation protocols introduced in the present work would provide additional verification of the quantitative accuracy of fMRI-based CMR_{O_2} measurement techniques. Ideally such PET studies would measure not only CMR_{O_2}, but CBF and CBV as well, permitting detailed assessment of assumptions underlying biophysical models of MRI signal behavior during brain activation. An area that is particularly worthy of further study is the relationship between blood flow and volume during brain activation. The steady-state model used in the present report relies critically on the assumption that CBV is a simple correlate of CBF, independent of the cause of a perfusion increase. While there is considerable indirect evidence that this is indeed the case, experimental verification of this supposition by measuring CBF and CBV during graded hyperperfusion, evoked using activation protocols like the ones developed in this work, is essential. This could be carried out using either PET-based steady-state CBV measurement techniques, or dynamic MRI methods in conjunction with recently developed blood pool contrast agents such as MION (monocrystalline iron oxide nanoparticles) [119].

There are several extensions of the CBF/CMR_{O_2} coupling experiments described in this thesis that would be interesting to perform. One example would be to investigate BOLD/CBF relationships during graded presentation of different combinations of visual patterns that are highly selective for complementary sub-populations of neurons. Such a protocol would be highly sensitive to variations in CBF/CMR_{O_2} coupling which might occur at specific energy consumption levels, depending on whether ATP requirements arise due to maximal electrical activity in a small number of neurons or moderate electrical activity in a large number of neurons. One pair of potential candidates for suitably complimentary stimuli would be the red uniform field and high spatial

frequency luminance grating used in the present study, which could be combined in simple linear superpositions. A second possibility would be different combinations of monocular and binocular stimulation using a non-specific visual stimulus, which might reveal interesting global coupling behavior due to the gratuitous hyperperfusion of unstimulated ocular dominance columns initially described by Frostig *et al.* [39,47]. Extension of the simultaneous BOLD and perfusion measurement technique to multiple slices [20] would permit cortical surface-based analysis of the data [92], facilitating comparisons of visual areas.

Another series of experiments that should be conducted is extension of the CBF/CMR_{O_2} coupling measurement protocol introduced here to additional cortical systems, including frontal, sensorimotor, and temporal cortex, as well as striatum. Activation in frontal cortex could be induced using a lexical search task, the hand region in sensorimotor cortex could be stimulated using repetitive finger/thumb opposition and vibrotactile stimulation, temporal regions could be activated with a working memory exercise, and striatal activity could be evoked using planned motor tasks. All of the above paradigms could be adapted to produce graded levels of activation, yielding general information about cerebral regulatory mechanisms. The basic V1 coupling protocol could also be performed in patients suffering from mitochondrial disorders such as MELAS (mitochondrial myopathy, encephalopathy, lactic acidosis, and stroke-like episodes) for quantitative characterization of aerobic metabolic deficits.

The results of the dynamics study presented in Chapter 6 suggest yet another area worthy of future study: examination of the implications of the non-linear signal characteristics reported in this paper for event-related fMRI methodologies. In particular it would be interesting to determine whether the impulse-response function yielded by such techniques for a specific stimulus is altered when it is randomly intermixed with a stimulus type, such as the yellow/blue radial checkerboard described in Chapter 6, which may invoke inhibitory feedback mechanisms with long time

constants. Because many of the experimental protocols developed in this work depend on complex gradations of multiple stimulus parameters, implementation of event-related versions of these methods (should the linearity issues prove tractable) is of considerable interest due to the potential for time savings and increased numbers of signal averages for a particular experimental condition. This attractive possibility is currently impeded by the steady-state requirements inherent to most MRI-based perfusion measurement techniques, and the increased complexity of dynamic biophysical models, however. The use of blood-pool contrast agents in animals and humans (upon approval by regulatory agencies) may expand the number of physiological processes open to dynamic study on relatively short time scales.

Finally, a more detailed understanding of the metabolic physiology of human brain and its relationship to neural information processing is only likely to be attained through integration of multiple imaging strategies. Magnetic resonance spectroscopy (MRS) [41, 66] and optical imaging of intrinsic signals [39, 47, 157–162] are examples of two techniques which should be systematically incorporated into the study of MRI-relevant brain activation physiology. Both of these methods have the potential to probe the biochemical events underlying physiological responses to neuronal activation, and optical techniques provide the additional benefit of extremely high spatial resolution. While MRS has been used to monitor levels of metabolic reagents such as glucose and lactate, optical imaging has been predominantly focused on systemic oxygen transporters, specifically hemoglobin and deoxyhemoglobin. The development of optical methods for imaging molecules that are more directly implicated in oxidative metabolism, such as the fluorescent compound NADH, could potentially extend our understanding of brain activation physiology by permitting metabolic redox imaging [157–162] at the cellular or even mitochondrial level.

Bibliography

[1] P.T. Fox and M.E. Raichle. Focal physiological uncoupling of cerebral blood flow and oxidative metabolism during somatorsensory stimulation in human subjects. *Proc. Natl. Acad. Sci. USA.*, 83:1140–1144, 1986.

[2] S. Marrett and A. Gjedde. Changes of blood flow and oxygen consumption in visual cortex of living humans. *Adv. Exp. Med. Biol.*, 413:205–208, 1997.

[3] M.S. Vafaee, S. Marrett, E. Meyer, A.C. Evans, and A. Gjedde. Increased oxygen consumption in human visual cortex: response to visual stimulation. *Acta Neurol. Scand.*, 98:85–89, 1998.

[4] P. C. Lauterbur. Image formation by induced local interactions: Examples using nuclear magnetic resonance. *Nature*, 242:190–191, 1973.

[5] J. W. Belliveau, D. N. Kennedy Jr., R. C. McKinstry, B. R. Buchbinder, R. M. Weisskoff, M. S. Cohen, J. M. Vevea, T. J. Brady, and B. R. Rosen. Functional mapping of the human visual cortex by magnetic resonance imaging. *Science*, 254(5032):716–9, Nov 1 1991.

[6] B. R. Rosen, J. W. Belliveau, and D. Chien. Perfusion imaging by nuclear magnetic resonance. *Magnetic Resonance Quarterly*, 5(4):263–81, Oct 1989.

[7] B. R. Rosen, J. W. Belliveau, J. M. Vevea, and T. J. Brady. Perfusion imaging with NMR contrast agents. *Magn. Reson. Med.*, 14(2):249–65, 1990.

[8] H. Fujita, E. Meyer, H. Kuwabara, A. C. Evans, and A. Gjedde. Cerebral ^{15}O water clearance in humans determined by PET: II. vascular response to vibrotactile stimulation. *Journal of Cerebral Blood Flow and Metabolism*, 1994. submitted April 1994.

[9] D. Le Bihan, E. Breton, D. Lallemand, P. Grenier, E. Cabanis, and M. Laval-Jeantet. MR imaging of intravoxel incoherent motions: application to diffusion and perfusion in neurologic disorders. *Radiology*, 161(2):401–7, Nov 1986.

[10] D. Le Bihan, E. Breton, D. Lallemand, M. L. Aubin, J. Vignaud, and M. Laval-Jeantet. Separation of diffusion and perfusion in intravoxel incoherent motion MR imaging. *Radiology*, 168(2):497–505, Aug 1988.

[11] D. Le Bihan. Magnetic resonance imaging of perfusion. *Magn. Reson. Med.*, 14(2):283–92, May 1990.

[12] R. Turner, D. Le Bihan, and A. S. Chesnick. Echo-planar imaging of diffusion and perfusion. *Magn. Reson. Med.*, 19(2):247–53, Jun 1991.

[13] D. Le Bihan, R. Turner, C. T. Moonen, and J. Pekar. Imaging of diffusion and microcirculation with gradient sensitization: design, strategy, and significance. *Journal of Magnetic Resonance Imaging*, 1(1):7–28, Jan-Feb 1991.

[14] J. Pekar, C. T. Moonen, and P. C. van Zijl. On the precision of diffusion/perfusion imaging by gradient sensitization. *Magn. Reson. Med.*, 23(1):122–9, Jan 1992.

[15] D. S. Williams, J. A. Detre, J. S. Leigh, and A. P. Koretsky. Magnetic resonance imaging of perfusion using spin inversion of arterial water [published erratum appears in proc natl acad sci u s a 1992 may 1;89(9):4220]. *Proceedings of the National Academy of Sciences of the United States of America*, 89(1):212–6, Jan 1 1992.

[16] J. A. Detre, J. S. Leigh, D. S. Williams, and A. P. Koretsky. Perfusion imaging. *Magn. Reson. Med.*, 23(1):37–45, Jan 1992.

[17] K. K. Kwong, J. W. Belliveau, D. A. Chesler, I. E. Goldberg, R. M. Weisskoff, B. P. Poncelet, D. N. Kennedy, B. E. Hoppel, M. S. Cohen, and R. Turner. Dynamic magnetic resonance imaging of human brain activity during primary sensory stimulation. *Proc. Natl. Acad. Sci. USA.*, 89(12):5675–9, Jun 15 1992.

[18] R. R. Edelman, B. Siewert, D. G. Darby, V. Thangaraj, A. C. Nobre, M. M. Mesulam, and S. Warach. Qualitative mapping of cerebral blood flow and functional localization with echo-planar MR imaging and signal targeting with alternating radio frequency. *Radiology*, 192(2):513–20, Aug 1994.

[19] E.C. Wong, R.B. Buxton, and L.R. Frank. Implementation of quantitative perfusion imaging techniques for functional brain mapping using pulsed arterial spin labeling. *NMR in Biomedicine*, 10:237–249, 1997.

[20] E.C. Wong and R.B. Frank, L.R. Buxton. QUIPPS II: a method for improved quantitation of perfusion using pulsed arterial spin labeling. In *Proceedings of the 5th Annual Meeting of the ISMRM*, page 1761, 1997.

[21] S. G. Kim. Quantification of relative cerebral blood flow change by flow-sensitive alternating inversion recovery (FAIR) technique: Application to functional mapping. *Magn. Reson. Med.*, 34(3):293–301, 1995.

[22] S. Ogawa, T. M. Lee, A. S. Nayak, and P. Glynn. Oxygenation-sensitive contrast in magnetic resonance image of rodent brain at high magnetic fields. *Magn. Reson. Med.*, 14(1):68–78, Apr 1990.

[23] S. Ogawa, T. M. Lee, A. R. Kay, and D. W. Tank. Brain magnetic resonance imaging with contrast dependent on blood oxygenation. *Proceedings of the National Academy of Sciences of the United States of America*, 87(24):9868–72, Dec 1990.

[24] S. Ogawa and T. M. Lee. Magnetic resonance imaging of blood vessels at high fields: in vivo and in vitro measurements and image simulation. *Magn. Reson. Med.*, 16(1):9–18, Oct 1990.

[25] S. Ogawa, D. W. Tank, R. Menon, J. M. Ellermann, S. G. Kim, H. Merkle, and K. Ugurbil. Intrinsic signal changes accompanying sensory stimulation: functional brain mapping with magnetic resonance imaging. *Proc. Natl. Acad. Sci. USA.*, 89:5951–5, 1992.

[26] L. Pauling and C. D. Coryell. The magnetic properties and structure of hemoglobin, oxyhemoglobin, and carbonmonoxyhemoglobin. *Proceedings of the National Academy of Sciences of the United States of America*, 22:210–216, 1936.

[27] K. R. Thulborn, J. C. Waterton, P. M. Matthews, and G. K. Radda. Oxygenation dependence of the transverse relaxation time of water protons in whole blood at high field. *Biochimica et Biophysica Acta*, 714(2):265–70, Feb 2 1982.

[28] G. A. Wright, B. S. Hu, and A. Macovski. 1991 I.I. Rabi Award. Estimating oxygen saturation of blood in vivo with MR imaging at 1.5 T. *Journal of Magnetic Resonance Imaging*, 1(3):275–83, May-Jun 1991.

[29] P. T. Fox and M. E. Raichle. Focal physiological uncoupling of cerebral blood flow and oxidative metabolism during somatosensory stimulation in human subjects. *Proceedings of the National Academy of Sciences of the United States of America*, 83(4):1140–4, Feb 1986.

[30] P. T. Fox, M. E. Raichle, M. A. Mintun, and C. Dence. Nonoxidative glucose consumption during focal physiologic neural activity. *Science*, 241:462–4, 1988.

[31] P. A. Bandettini, E. C. Wong, R. S. Hinks, R. S. Tikofsky, and J. S. Hyde. Time course epi of human brain function during task activation. *Magn. Reson. Med.*, 25(2):390–7, Jun 1992.

[32] J. M. Levin, M. H. Ross, and P. F. Renshaw. Clinical applications of functional MRI in neuropsychiatry. *Journal of Neuropsychiatry & Clinical Neurosciences*, 7(4):511–22, Fall 1995.

[33] R. E. Latchaw, K. Ugurbil, and X. Hu. Functional MR imaging of perceptual and cognitive functions. *Neuroimaging Clinics of North America*, 5(2):193–205, May 1995.

[34] D. Le Bihan and A. Karni. Applications of magnetic resonance imaging to the study of human brain function. *Current Opinion in Neurobiology*, 5(2):231–7, Apr 1995.

[35] K. K. Kwong. Functional magnetic resonance imaging with echo planar imaging. *Magnetic Resonance Quarterly*, 11(1):1–20, Mar 1995.

[36] M. S. Cohen and S. Y. Bookheimer. Localization of brain function using magnetic resonance imaging. *Trends in Neurosciences*, 17(7):268–77, Jul 1994.

[37] C.S. Roy and C.S. Sherrington. On the regulation of the blood supply of the brain. *J. Physiol.*, 11:85–105, 1890.

[38] P.T. Fox, M.A. Mintun, M.E. Raichle, F.M. Miezin, J.M. Allman, and D.C. Van Essen. Mapping human visual cortex with positron emission tomography. *Nature*, 323(6091):806–809, 1986.

[39] R.D. Frostig, E.E. Lieke, D.Y. Tso, and A. Grinvald. Cortical functional architecture and local coupling between neuronal activity and the microcirculation revealed by in vivo high-resolution optical imaging. *Proc. Natl. Acad. Sci. USA.*, 87(16):6082–6086, 1990.

[40] B. Siesjo. *Brain Energy Metabolism*. Wiley, New York, 1978.

[41] J. Prichard, D. Rothman, and E. Novotny. Lactate rise detected by ^{1}H NMR in human visual cortex during physiologic stimulation. *Proc. Natl. Acad. Sci. USA.*, 88:5829–5831, 1991.

[42] S.-G. Kim and K. Uğurbil. Comparison of blood oxygenation and cerebral blood flow effects in fMRI: Estimation of relative oxygen consumption change. *Magn. Reson. Med.*, 38:59–65, 1997.

[43] S. Ogawa, R.S. Menon, D.W. Tank, S.-G. Kim, H. Merkle, J.M. Ellermann, and K. Uğurbil. Functional brain mapping by blood oxygenation level-dependent contrast magnetic resonance imaging; A comparison of signal characteristics with a biophysical model. *Biophys. Journal*, 64:803–812, 1993.

[44] P.E. Roland, L. Eriksson, S. Stone-Elander, and L. Widen. Does mental activity change the oxidative metabolism of the brain? *J. Neurosci.*, 7(8):2373–2389, 1987.

[45] S. Marrett, H. Fujita, E. Meyer, L. Ribeiro, A.C. Evans, H. Kuwabara, and A. Gjedde. *Stimulus specific increase of oxidative metabolism in human visual cortex*, pages 217–224. Elsevier Science Publishers, 1993.

[46] M. Vafaee, E. Meyer, S. Marrett, T. Paus, A. C. Evans, and Gjedde A. Frequency-dependent changes in cerebral metabolic rate of oxygen (cmr_{o_2}) in the human striate cortex. In *Proceedings of the 3d International Conference on Functional Mapping of the Human Brain*, volume 5, page 35, Copenhagen, 1997.

[47] D. Malonek and A. Grinvald. Interactions between electrical activity and cortical microcirculation revealed by imaging spectroscopy: implications for functional brain mapping. *Science*, 272:551–554, 1996.

[48] F. Hyder, J.R. Chase, K.L. Behar, G.F. Mason, M. Sideek, D.L. Rothman, and R.G. Shulman. Increased tricarboxylic acid cycle flux in rat brain during forepaw stimulation detected with $^{1}H[^{13}C]$NMR. *Proc. Natl. Acad. Sci. USA.*, 93(15):7612–7617, 1996.

[49] R. B. Buxton and L. R. Frank. A model for the coupling between cerebral blood flow and oxygen metabolism during neural stimulation. *J. Cereb. Blood. Flow Metab.*, 17(1):64–72, Jan 1997.

[50] R.S. Menon, S. Ogawa, X. Hu, J.P. Strupp, P. Anderson, and K. Uğurbil. BOLD based functional MRI at 4 Tesla includes a capillary bed contribution: Echo-planar imaging correlates with previous optical imaging using intrinsic signals. *Magn. Reson. Med.*, 33:453–459, 1995.

[51] T.L. Davis, K.K. Kwong, R.M. Weisskoff, and B.R. Rosen. Calibrated functional MRI: Mapping the dynamics of oxidative metabolism. *Proc. Natl. Acad. Sci. USA.*, 95:1834–1839, 1998.

[52] J.C. Horton. Mapping of cytochrome oxidase patches and ocular dominance columns in human visual cortex. *Philos. Trans. R. Soc. London, Ser. B*, 304:255–272, 1984.

[53] J.C. Horton. Cytochrome oxidase patches: a new cytoarchitectonic feature of monkey visual cortex. *Philos. Trans. R. Soc. London, Ser. B*, 304:199–253, 1984.

[54] E.W. Carroll and M.T. Wong-Riley. Quantitative light and electron microscopic analysis of cytochrome oxidase-rich zones in the striate cortex of the squirrel monkey. *Journal of Comparitive Neurology*, 222:1–17, 1984.

[55] M.T. Wong-Riley and E.W. Carroll. Quantitative light and electron microscopic analysis of cytochrome oxidase-rich zones in V II prestriate cortex of the squirrel monkey. *Journal of Comparitive Neurology*, 222:18–37, 1984.

[56] M.T.T. Wong-Riley. Cytochrome oxidase: an endogenous metabolic marker for neuronal activity. *Trends in neurosciences*, 12(3):94–101, 1989.

[57] I.W. Borowsky and R.C. Collins. Metabolic anatomy of the brain: A comparison of regional capillary density, glucose metabolism, and enzyme activities. *Journal of Comparitive Neurology*, 288:401–413, 1989.

[58] U.I. Tuor, G. Kurpita, and C. Simone. Correlation of local changes in cerebral blood flow, capillary density, and cytochrome oxidase during development. *Journal of Comparitive Neurology*, 342:439–448, 1994.

[59] D. Zheng, A.-S. LaMantia, and D. Purves. Specialized vascularization of the primate visual cortex. *J. Neurosci.*, 11(8):2622–2629, 1991.

[60] R.B.H. Tootell, S.L. Hamilton, M.S. Silverman, and E. Switkes. Functional anatomy of macacque striate cortex. I. Oculuar dominance, binocular interactions, and baseline conditions. *J. Neurosci.*, 8(5):1500–1530, 1988.

[61] R.B.H. Tootell, M.S. Silverman, S.L. Hamilton, R.L. De Valois, and E. Switkes. Functional anatomy of macacque striate cortex. III. Color. *J. Neurosci.*, 8(5):1569–1593, 1988.

[62] M.S. Livingstone and D. Hubel. Psychophysical evidence for separate channels for the perception of form, color, movement, and depth. *J. Neurosci.*, 7(11):3416–3468, 1987.

[63] M. Livingstone and D. Hubel. Segregation of form, color, movement, and depth: anatomy, physiology, and perception. *Science*, 240:740–749, 1988.

[64] M.S. Livingstone and D. Hubel. Segregation of form, color, and stereopsis in primate area 18. *J. Neurosci.*, 7(11):3378–3415, 1987.

[65] G.M. Hathout, K.A.T. Kirlew, G.J.K. So, D.R. Hamilton, J.X. Zhang, U. Sinha, S. Shinha, J. Sayre, D. Gozal, R.M. Harper, and R.B. Lufkin. MR imaging signal response to sustained stimulation in human visual cortex. *J. Magn. Reson. Imaging*, 4:537–543, 1994.

[66] J. Frahm, G. Kr uger, K.-D. Merboldt, and A. Kleinschmidt. Dynamic uncoupling and recoupling of perfusion and oxidative metabolism during focal brain activation in man. *Magn. Reson. Med.*, 35:143–148, 1996.

[67] P.A. Bandettini, K.K. Kwong, T.L. Davis, R.B.H. Tootell, E.C. Wong, P.T. Fox, J.W. Belliveau, R.M. Weisskoff, and B.A. Rosen. Characterization of cerebral blood oxygenation and flow changes during prolonged brain activation. *Hum. Brain Mapp.*, 5:93–109, 1997.

[68] W. Chen, X.-H. Zhu, T. Kato, P. Andersen, and K. Uğurbil. Spatial and temporal differentiation of fMRI BOLD response in primary visual cortex of human brain during sustained visual stimulation. *Magn. Reson. Med.*, 39:520–527, 1998.

[69] A.M. Howseman, D.A. Porter, C. Hutton, O. Josephs, and R. Turner. Blood oxygenation level dependent signal time courses during prolonged visual stimulation. *Magn. Reson. Imaging*, 16(1):1–11, 1998.

[70] G. Kruger, A. Kleinschmidt, and J. Frahm. Stimulus dependence of oxygenation-sensitive MRI responses to sustained visual activation. *NMR Biomed.*, 11:75–79, 1998.

[71] A.M. Dale and R.L. Buckner. Selective averaging of rapidly presented individual trials using fmri. *Hum. Brain Mapp.*, 5:329–340, 1997.

[72] T. Ernst and J. Hennig. Observation of a fast response in functional MR. *Magn. Reson. Med.*, 32:146–149, 1994.

[73] E. Yacoub, E.R. Cohen, and X. Hu. Echo time dependence of the initial negative response in fMRI. In *Proceedings of the 6th Annual Meeting of the ISMRM*, page 5, Sydney, 1998.

[74] T. L. Davis, R.M. Weisskoff, K.K. Kwong, J.L. Boxerman, and B.R. Rosen. Temporal aspects of fMRI task activation: Dynamic modeling of oxygen delivery. In *Proceedings of the 2d Annual Meeting of the ISMRM*, page 69, San Francisco, 1994.

[75] R.B. Buxton, E.C. Wong, and L.R. Frank. Dynamics of blood flow and oxygenation changes during brain activation: The balloon model. *Magn. Reson. Med.*, 39:855–864, 1998.

[76] J.B. Mandeville, J.J.A. Marota, G. Zaharchuk, C. Ayata, T.L. Davis, M. Moskowitz, R.M. Weisskoff, and B.R. Rosen. Evidence for a cerebral post-arteriole windkessel. In *Proceedings of the 6th Annual Meeting of the ISMRM*, page 1144, Sydney, 1998.

[77] J.B. Mandeville, J.J.A. Marota, C. Ayata, G. Zaharchuk, M.A. Moskowitz, B.R. Rosen, and R.M. Weisskoff. Evidence for a cerebral post-arteriole windkessel. In *J. Cereb. Blood. Flow Metab.*, 1998. in press.

[78] O. Frank. Die grundform des arterielen pulses. *Z. Biol.*, 85:91–130, 1899.

[79] F.W. Cope. Elastic reservoir theories of the human circulation with applications to clinical medicine and computer analysis of the circulation. *Adv. Exp. Med. Biol.*, 10:277–356, 1965.

[80] G.M. Boynton, S.A. Engel, G.H. Glover, and D.J. Heeger. Linear systems analysis of functional magnetic resonance imaging in human V1. *J. Neurosci.*, 16(13):4207–4221, 1996.

[81] L. R. Schad, E. Wiener, K. T. Baudendistel, E. Muller, and W. J. Lorenz. Event-related functional MR imaging of visual cortex stimulation at high temporal resolution using a standard 1.5 T imager. *Magn. Reson. Imaging*, 13(6):899–901, 1995.

[82] K.J. Friston, O. Josephs, G. Rees, and R. Turner. Nonlinear event-related responses in fMRI. *Magn. Reson. Med.*, 39:41–52, 1998.

[83] R.L. Buckner. Event-related fMRI and the hemodynamic response. *Hum. Brain Mapp.*, 6:373–377, 1998.

[84] A.D. Wagner, D.L. Schacter, M. Rotte, W. Koutstaal, A. Maril, A.M. Dale, B.R. Rosen, and R.L. Buckner. Building memories: Remembering and forgetting of verbal experiences as predicted by brain activity. *Science*, 281(5380):1188–1191, 1998.

[85] K.J. Friston, P. Fletcher, O. Josephs, A. Holmes, M.D. Rugg, and R. Turner. Event-related fMRI: Characterizing differential responses. *NeuroImage*, 7(1):30–40, 1998.

[86] B.R. Rosen, R.L. Buckner, and A.M. Dale. Event-related functional MRI: Past, present, and future. *Proc. Natl. Acad. Sci. USA.*, 95(3):773–780, 1998.

[87] R. M. Weisskoff, C. S. Zuo, J. L. Boxerman, and B. R. Rosen. Microscopic susceptibility variation and transverse relaxation: Theory and experiment. *Magn. Reson. Med.*, 31(6):601–610, Jun 1994.

[88] H. L. Boxerman, J. L. Hamberg, B. R. Rosen, and R. M. Weisskoff. MR contrast due to intravascular magnetic susceptibility perturbations. *Magn. Reson. Med.*, 34(4):555–566, 1995.

[89] M. S. Silver, R. I. Joseph, and D. I. Hoult. Highly selective $\pi/2$ and π pulse generation. *Journal of Magnetic Resonance*, 59:47–351, 1984.

[90] G. R. Crelier, R. D. Hoge, P. Munger, and G. B. Pike. Perfusion-based functional magnetic resonance imaging with single-shot rare and grase acquisitions. *Magn. Reson. Med.*, Nov 1998. in press.

[91] R. D. Hoge, R. K. Kwan, and G. B. Pike. Density compensation functions for spiral mri. *Magn. Reson. Med.*, 38(1):117–28, Jul 1997.

[92] M.I. Sereno, A.M. Dale, J.B. Reppas, K.K. Kwong, J.W. Belliveau, T.J. Brady, B.R. Rosen, and R.B.H. Tootell. Borders of multiple visual areas in humans revealed by functional magnetic resonance imaging. *Science*, 268:889–893, 1995.

[93] D. L. Collins, P. Neelin, T. M. Peters, and A. C. Evans. Automatic 3D registration of MR volumetric data in standardized Talairach space. *J. Comput. Assist. Tomogr.*, 18(2):192–205, 1994.

[94] R.D. Hoge. Performing fMRI studies at the McConnell Brain Imaging Centre. http://www.bic.mni.mcgill.ca/users/rhoge/fmri.html.

[95] C.J. Holmes, R.D. Hoge, L. Collins, R. Woods, A.W. Toga, and A.C. Evans. Enhancement of magnetic resonance images using registration for signal averaging. *J. Comput. Assist. Tomogr.*, 22(2):324–333, 1998.

[96] J.D. Atkinson, R.D. Hoge, A.F. Sadikot, and G.B. Pike. fMRI demonstration of laterality of supplementary motor area and deep nuclear activation in subjects of different handedness. In *Proceedings of the 4th International Conference on Functional Mapping of the Human Brain*, volume 1, page 958, Montreal, 1998.

[97] P. Belin, R.J. Zatorre, R.D. Hoge, G.B. Pike, and A.C. Evans. Event-related fMRI of auditory cortex. In *Proceedings of the 4th International Conference on Functional Mapping of the Human Brain*, volume 1, page 369, Montreal, 1998.

[98] T. Paus, G. Leonard, M. Wolforth, R. Visca, R. Comeau, R. Hoge, B. Pike, T. Peters, C.J. Thompson, and A.C. Evans. Cortico-cerebellar connectivity revealed by transcranial magnetic stimulation of the human motor cortex during positron emission tomography. In *Proceedings of the Society for Neuroscience*, page 1276, 1997.

[99] M. Barinaga. What makes brain neurons run? *Science*, 276:196–198, 1997.

[100] P. Brodersen, O.B. Paulson, and T.G. Bolwig. Cerebral hyperemia in electrically induced epileptic seizures. *Arch. Neurol.*, 28:334–338, 1973.

[101] L. Widén. In N.A. Lassen, D.H. Ingvar, M.E. Raichle, and L. Friberg, editors, *Brain Work and Energy Metabolism*, pages 127–139, Copenhagen, 1991. Munskgaard.

[102] A. Gjedde, S. Ohta, H. Kuwabara, and E. Meyer. In N.A. Lassen, D.H. Ingvar, M.E. Raichle, and L. Friberg, editors, *Brain Work and Energy Metabolism*, pages 177–184, Copenhagen, 1991. Munskgaard.

[103] S.S. Kety and C.F. Schmidt. The effects of altered arterial tensions of carbon dioxide and oxygen on cerebral blood flow and cerebral oxygen consumption of normal young men. *J. Clin. Invest.*, 27:484–492, 1948.

[104] S.-P. Yang and J.A. Krasney. Cerebral blood flow and metabolic responses to sustained hypercapnia in awake sheep. *J. Cereb. Blood. Flow Metab.*, 15:115–123, 1995.

[105] S. Ogawa, R. S. Menon, D. W. Tank, S. G. Kim, H. Merkle, J. M. Ellermann, and K. Ugurbil. Functional brain mapping by blood oxygenation level-dependent contrast magnetic resonance imaging. A comparison of signal characteristics with a biophysical model. *Biophysical Journal*, 64(3):803–12, Mar 1993.

[106] R.B.H. Tootell, M.S. Silverman, S.L. Hamilton, R.L. De Valois, and E. Switkes. Functional anatomy of macacque striate cortex. V. Spatial frequncy. *J. Neurosci.*, 8(5):1610–1624, 1988.

[107] R.L. Grubb, M.E. Phelps, and J.O. Eichling. The effects of vascular changes in $PaCO_2$ on cerebral blood volume, blood flow and vascular mean transit time. *Stroke*, 5:630–639, 1974.

[108] J. L. Boxerman, P. A. Bandettini, K. K. Kwong, J. R. Baker, T. L. Davis, B. R. Rosen, and R. M. Weisskoff. The intravascular contribution to fMRI signal change: Monte carlo modeling and diffusion-weighted studies in vivo. *Magn. Reson. Med.*, 34(1):4–10, 1995.

[109] R.F. Schmidt and G. Thews. *Human Physiology*. Springer-Verlag, Berlin, 1983.

[110] F. Hyder, R.G. Shulman, and D.L. Rothman. A model for the regulation of cerebral oxygen delivery. *J. Appl. Physiol.*, 85:554–564, 1998.

[111] D.Y. Ho, E.S. Mocarski, and R.M. Sapolsky. Altering central nervous system physiology with a defective herpes simplex virus vector expressing the glucose transporter gene. *Proc. Natl. Acad. Sci. USA.*, 90:3655–3659, 1993.

[112] A. Akabayashi and T. Kato. Glucose utilization rates in single neurons and neuropil determined by injecting nontracer amounts of 2-deoxyglucose. *J. Neurochem.*, 60:931–935, 1993.

[113] R.S. Orlov, B. Isakov, A.T. Ketkin, and I.P. Plekhanov. *Brain Blood Supply*. Akadémiai Kiadó, Budapest, 1977.

[114] C.M. Rovainen, T.A. Woolsey, N.C. Blocher, D.-B. Wang, and O.F. Robinson. Blood flow in single surface arterioles and venules on the mouse somatosensory cortex measured with videomicroscopy, fluorescent dextrans, nonoccluding fluorescent beads, and computer-assisted image analysis. *J. Cereb. Blood. Flow Metab.*, 13:359–371, 1993.

[115] P.C.M. van Zijl, S.M. Eleff, J.A. Ulatowski, J.M.E. Oja, A.M. Uluğ, R.J. Traystman, and R.A. Kauppinen. Quantitative assessment of blood flow, blood volume and blood oxygenation effects in functional magnetic resonance imaging. *Nature Medicine*, 4(2):159–167, 1998.

[116] C. Estrada and J. DeFilipe. Nitric oxide-producing neurons in the neocortex: Morphological and functional relationship with intraparenchymal microvasculature. *Cerebral Cortex*, 8:1047–3211, 1998.

[117] J.B. Mandeville, J.J. Marota, R.W. Weisskoff, and B.R. Rosen. An NMR methodology for measuring changes in CMR_{O_2} during functional challenge. In *Proceedings of the 5th Annual Meeting of the ISMRM*, page 155, 1997.

[118] E.M. Haacke, S. Lai, J.R. Reichenbach, K. Kupusamy, F.G.C. Hoogenraad, H. Takeichi, and W. Lin. In vivo measurement of blood oxygen saturation using magnetic resonance imaging: A direct validation of the blood oxygen level-dependent concept in functional brain imaging. *Hum. Brain Mapp.*, 5:341–346, 1997.

[119] J.B. Mandeville, J.J.A. Marota, B.E. Kosofsky, J.R. Keltner, R. Weissleder, B.R. Rosen, and R.M. Weisskoff. Dynamic functional imaging of relative cerebral blood volume during rat forepaw stimulation. *Magn. Reson. Med.*, 39:615–624, 1998.

[120] J.L.D. Atkinson, R.E. Anderson, and T.M. Sundt. The effect of carbon dioxide on the diameter of brain capillaries. *Brain Research*, 517:333–340, 1990.

[121] E. Rostrup, H. B. Larsson, P. B. Toft, K. Garde, C. Thomsen, P. Ring, L. Sondergaard, and O. Henriksen. Functional MRI of CO_2 induced increase in cerebral perfusion. *NMR in Biomedicine*, 7(1-2):29–34, Mar 1994.

[122] H. Bruhn, A. Kleinschmidt, H. Boecker, K. D. Merboldt, W. Hanicke, and J. Frahm. The effect of acetazolamide on regional cerebral blood oxygenation at rest and under stimulation as assessed by MRI. *J. Cereb. Blood. Flow Metab.*, 14(5):742–8, Sep 1994.

[123] D.C. Reutens, M.D. McHugh, P.-J. Toussaint, A.E. Evans, A. Gjedde, E. Meyer, and D.J. Stewart. L-arginine infusion increases basal but not activated cerebral blood flow in humans. *J. Cereb. Blood. Flow Metab.*, 17:309–315, 1997.

[124] G. Zaharchuk, S. Sasamata, J.B. Mandevill, M.A. Moskowitz, and B.R. Rosen. Increased perfusion after acetazolamide challenge demonstrated in the ischemic rat brain using echo-planar arterial spin label perfusion imaging. In *Proceedings of the 5th Annual Meeting of the ISMRM*, page 604, 1997.

[125] G.G. Brown, L.T. Eyler-Zorrilla, B. Georgy, R.B. Buxton, S.S. Kindermann, and E.C. Wong. Simultaneous alteration of perfusion-weighted and BOLD-weighted contrast by acetazolamide infusion. In *Proceedings of the 6th Annual Meeting of the ISMRM*, page 1583, 1998.

[126] R.B. Buxton, E.C. Wong, and L.R. Frank. A biomechanical interpretation of the BOLD time course: the balloon model. In *Proceedings of the 5th Annual Meeting of the ISMRM*, page 743, 1997.

[127] D.A. Yablonskiy and E.M. Haacke. Theory of NMR signal behaviour in magnetically inhomogeneous tissues: The static dephasing regime. *Magn. Reson. Med.*, 32:749–763, 1994.

[128] G. M. Hathout, S. S. Gambhir, R. K. Gopi, K. A. Kirlew, Y. Choi, G. So, D. Gozal, R. Harper, R. B. Lufkin, and R. Hawkins. A quantitative physiologic model of blood oxygenation for functional magnetic resonance imaging. *Investigative Radiology*, 30(11):669–82, Nov 1995.

[129] P.A. Bandettini and K.M. Donahue. Analysis of activation-induced and post-activation undershoot ΔR_2^* and ΔR_2 magnitudes and ratios at 1.5 Tesla using synchronous gradient-echo and spin-echo (SGS)-EPI. In *Proceedings of the 6th Annual Meeting of the ISMRM*, page 1393, 1998.

[130] R.B. Buxton, W.M. Luh, E.C. Wong, L.R. Frank, and P.A. Bandettini. Diffusion-weighting attenuates the BOLD peak signal change but not the post-stimulus undershoot. In *Proceedings of the 6th Annual Meeting of the ISMRM*, page 7, 1998.

[131] R.A. Jones, T. Schirmer, B. Lipinski, and G.K. Elbel. Signal undershoots following visual stimulation: A comparison of gradient echo and spin-echo BOLD sequences. *Magn. Reson. Med.*, 40:112–118, 1998.

[132] R.D. Hoge, B. Gill, G.R. Crelier, and G.B. Pike. Comparison of perfusion and BOLD responses in human visual cortex to blob-selective stimuli, inter-blob-selective stimuli, and hypercapnia. In *Proceedings of the 6th Annual Meeting of the ISMRM*, page 1537, Sydney, 1998.

[133] R.D. Hoge, B. Gill, J. Atkinson, Crelier. G.R., S.M. Marrett, and G.B. Pike. Investigation of CMR_{O_2}/CBF coupling in human V1 using FMRI. In *Proceedings of the 4th International Conference on Functional Mapping of the Human Brain*, volume 1, page 262, Montreal, 1998.

[134] J.B. Mandeville, J. Marota, J.R. Keltner, B. Kosovsky, J. Burke, S. Hyman, and L. LaPointe. CBV functional imaging in rat brain using iron oxide agent at steady state concentration. In *Proceedings of the 4th Annual Meeting of the ISMRM*, page 292, 1996.

[135] H.E. Ives. A chart of the flicker photometer. *J Opt Soc Am Rev Sci Instr*, 7:363, 1923.

[136] E.W. Hsu, L.W. Hedlund, and J.R. MacFall. Functional MRI of the rat somatosensory cortex: Effects of hyperventilation. *Magn. Reson. Med.*, 40:421–426, 1998.

[137] S.C. Ramsay, K. Murphy, S.A. Shea, K.J. Friston, A.A. Lammertsma, J.C. Clark, L. Adams, A. Guz, and R.S.J. Frackowiak. Effect on regional cerebral blood flow during a neural activation task. *Journal of Physiology*, 471:521–534, 1993.

[138] E. Shimosegawa, I. Kanno, J. Hatazawa, H. Fujita, H. Iida, S. Miura, M. Murakami, A. Inugami, T. Ogawa, H. Itoh, T. Okudera, and K. Uemura. Photic stimulation study of changing the arterial partial pressure level of carbon dioxide. *J. Cereb. Blood. Flow Metab.*, 15:111–114, 1995.

[139] P.A. Bandettini and E.C. Wong. A hypercapnia-based normalization method for improved spatial localization of human brain activation with fMRI. *NMR Biomed.*, 10:197–203, 1997.

[140] F. Caramia, R.B. Tootell, B.G. Jenkins, B.R. Rosen, and K.K. Kwong. Comparison of fMRI signal changes produced by stimuli selective for blob vs. inter-blob cells in V1. In *Proceedings of the 1st International Conference on Functional Mapping of the Human Brain*, volume 1, page 26, Paris, 1995.

[141] M. Vafaee, E. Meyer, S. Marrett, T. Paus, A. C. Evans, and Gjedde A. Cerebral blood flow (CBF) and cerebral metabolic rate of oxygen (CMR_{o_2}) respond differently to the rate of visual stimulation. In *Proceedings of the 27th Annual Meeting of the Society for Neuroscience*, New Orleans, 1997.

[142] X.-H. Zhu, S.-G. Kim, P. Andersen, S. Ogawa, K. Uğurbil, and W. Chen. Dynamic study of BOLD, CBF, and CMR_{O_2} changes correlated to varied neuronal activity in primary visual cortex of humans. In *Proceedings of the 6th Annual Meeting of the ISMRM*, page 10, 1998.

[143] R.B. Buxton and L.R. Frank. A model for the coupling between cerebral blood flow and oxygen metabolism during neural stimulation. *J. Cereb. Blood. Flow Metab.*, 17:64–72, 1997.

[144] B. Conrad and J. Klingelh ofer. Dynamics of regional cerebral blood flow for varios visual stimuli. *Exp. Brain Res.*, 77:437–441, 1989.

[145] K. Irikura, K.I. Maynard, and M.A. Moskowitz. Importance of nitric oxide synthase inhibition to the attenuated vascular responses induced by topical L-nitroarginine during vibrissal stimulation. *J. Cereb. Blood. Flow Metab.*, 14:45–48, 1994.

[146] R.B.H. Tootell, E. Switkes, M.S. Silverman, and S.L. Hamilton. Functional anatomy of macacque striate cortex. II. Retinotopic organization. *J. Neurosci.*, 8(5):1531–1568, 1988.

[147] R.B.H. Tootell, S.L. Hamilton, and E. Switkes. Functional anatomy of macacque striate cortex. IV. Contrast and magno-parvo streams. *J. Neurosci.*, 8(5):1594–1609, 1988.

[148] K. K. Kwong, D. A. Chesler, R. M. Weisskoff, K. M. Donahue, T. L. Davis, L. Ostergaard, T. A. Campbell, and B. R. Rosen. MR perfusion studies with T1-weighted echo planar imaging. *Magn. Reson. Med.*, 34(6):878–87, Dec 1995.

[149] W.H. Press, S.A. Teukolsky, W.T. Verrerling, and B.P. Flannery. *Numberical Recipes in C.* Cambridge, New York, 1992.

[150] T. L. Davis, R.M. Weisskoff, K.K. Kwong, R. Savoy, and B.R. Rosen. Susceptibility contrast undershoot is not matched by inflow contrast undershoot. In *Proceedings of the 2d Annual Meeting of the ISMRM*, page 435, San Francisco, 1994.

[151] P. Hedera, D. Wu, J. S. Lewin, D. Miller, A. J. Lerner, and R. P. Friedland. Temporal patterns of uncoupling between oxidative metabolism and regional cerebral blood flow demonstrated by functional magnetic resonance imaging. *Invest. Radiol.*, 30(11):625–33, 1995.

[152] A. Kleinschmidt, O. Gruber, S. Posse, L. J anke, M. Grosse-Ruyken, H.-W. M uller-G artner, and H.-J. Freund. Deriving stimulus-response functions from cerebral blood oxygenation - optimizing timing and design of sensory activation paradigms. In *Proceedings of the 3d International Conference on Functional Mapping of the Human Brain*, volume 1, page 38, Copenhagen, 1997.

[153] C. Janz, O. Speck, and J. Hennig. Time-resolved measurements of brain activation after a short visual stimulus: New results on the physiological mechanisms of the cortical response. *NMR Biomed.*, 10:222–229, 1997.

[154] P. Fransson, G. Kr uger, K.-D. Merboldt, and J. Frahm. Temporal characteristics of oxygenation-sensitive MRI responses to visual activation in humans. *Magn. Reson. Med.*, 39:912–919, 1998.

[155] R. S. Menon, S. Ogawa, D. W. Tank, and K. Ugurbil. 4 Tesla gradient recalled echo characteristics of photic stimulation-induced signal changes in the human primary visual cortex. *Magn. Reson. Med.*, 30(3):380–6, Sep 1993.

[156] C.G. Thomas and R.S. Menon. Amplitude response and stimulus presentation frequency response of human primary visual cortex using BOLD EPI at 4 T. *Magn. Reson. Med.*, 40:203–209, 1998.

[157] B. Chance, P. Cohen, F. Jobsis, and B. Schoener. Intracellular oxidation-reduction states in vivo. *Science*, 137:499–508, 1962.

[158] A. Mayevsky and B. Chance. Intracellular oxidation-reduction state measured in situ by a multichannel fiber-optic surface fluorometer. *Science*, 217:537–540, 1982.

[159] G. Renault, E. Raynal, M. Sinet, M. Muffat-Joly, J.-P. Berthier, B.G. Cornilault, and J.-J. Pocidalo. In situ double-beam nadh laser fluorimetry: choice of a reference wavelength. *Am. J. Physiol.*, 246:491–499, 1984.

[160] J.C. Haselgrove, C.L. Bashford, C.H. Barlow, B. Quistorff, B. Chance, and A. Mayevsky. Time resolved 3-dimensional recording of redox ratio during spreading depression in gerbil brain. *Brain Res.*, 506:109–114, 1990.

[161] F.H. Tomlinson, R.E. Anderson, and F.B. Meyer. Brain ph_i, cerebral blood flow, and NADH fluorescence during severe incomplete global ischemia in rabbits. *Stroke*, 24:435–443, 1993.

[162] D.W. Piston, B.R. Masters, and W.W. Webb. Three-dimensional resolved NAD(P)H cellular metabolic redox imaging of the in situ cornea with two-photon excitation laser scanning microscopy. *J. Microsc.*, 178:20–27, 1994.

Chapter 9: Appendices

Appendix A: Density Compensation Functions for Spiral MRI

Density Compensation Functions for Spiral MRI

Richard D. Hoge, Remi K. S. Kwan, G. Bruce Pike

In interleaved spiral MRI, an object's Fourier transform is sampled along a set of curved trajectories in the spatial frequency domain (*k*-space). An image of the object is then reconstructed, usually by interpolating the sampled Fourier data onto a Cartesian grid and applying the fast Fourier transform (FFT) algorithm. To obtain accurate results, it is necessary to account for the nonuniform density with which *k*-space is sampled. An analytic density compensation function (DCF) for spiral MRI, based on the Jacobian determinant for the transformation between Cartesian coordinates and the spiral sampling parameters of time and interleaf rotation angle, is derived in this paper, and the reconstruction accuracy achieved using this function is compared with that obtained using several previously published expressions. Various nonideal conditions, including intersecting trajectories, are considered. The new DCF eliminated intensity cupping that was encountered in images reconstructed with other functions, and significantly reduced the level of artifact observed when unevenly spaced sampling trajectories, such as those achieved with trapezoidal gradient waveforms, were employed. Modified forms of this function were found to provide similar improvements when intersecting trajectories made the spiral-Cartesian transformation noninvertible, and when the shape of the spiral trajectory varied between interleaves.

Key words: spiral imaging; nonuniform sampling; image reconstruction.

INTRODUCTION

Spiral MRI (1, 2) has shown considerable promise as a fast imaging method with applications in cardiac imaging (2), functional brain imaging (3, 4), quantitative flow measurement (5), and fast 3D volumetric acquisition (6). In this class of techniques, the imaging gradients are modulated during readout so that the observed signal represents the Fourier transform of the object as seen along a spiral trajectory through the spatial frequency domain (*k*-space). An image of the object can then be reconstructed, either by direct summation of the nonuniformly sampled Fourier components or by interpolating the sampled data onto a Cartesian grid (7, 8) and inverting using the fast Fourier transform (FFT). In either approach, the nonuniform density of spiral sampling must be accounted for, or there will be errors in the reconstructed image. This is usually accomplished by multiplying the *k*-space samples by a *density compensation function*, or DCF.

Density compensation, in conjunction with *k*-space trajectory measurement, is especially important when hardware limits are approached. Takahashi and Peters have demonstrated that the high gradient slew-rates and amplitudes required for spiral techniques often lead to distortion of the waveforms delivered by the MRI system (9). This phenomenon has also been described by Spielman and Pauly as particularly severe on high-field small bore magnets (10). Furthermore, some high speed gradient systems cannot generate arbitrary waveforms, and trapezoidal approximations of the desired functions must be used (11, 12). The sampling density achieved with such distorted or approximated waveforms usually exhibits large and abrupt fluctuations with position in *k*-space, leading to severe artifacts in reconstructed images if appropriate compensation is not performed.

The most commonly cited analytic density compensation function for spiral MRI is the one described by Meyer *et al.* in (2). This expression has been shown to yield good image quality when the sampling density varies smoothly. Nonetheless, we have found that if the sampling density fluctuates sharply along the spiral trajectory, as is generally the case when trapezoidal or distorted gradient waveforms are employed, then this expression leads to prominent artifacts in reconstructed images. We have also found that images reconstructed using this DCF exhibit an intensity cupping artifact, even if the sampling density varies smoothly along the sampling trajectory. Other analytic expressions have been proposed (13, 14), but these suffer from similar problems and have not been widely adopted.

Several purely numerical techniques for calculating sampling density have also been described (7, 15), but these are more computationally intensive than analytic methods. Furthermore, closed form expressions for sampling density, as a function of *k*-space trajectory, are useful for gradient waveform design and optimization.

Much of the early work on spiral reconstruction addressed the problem of density compensation for noninterleaved, or single-shot, spiral techniques (16–18). The analysis given by Soumekh (17, 18) represents a valid solution of the density compensation problem for spiral data acquisition. However, only noninterleaved acquisitions were considered, necessitating the awkward notion of a pseudo-two-dimensional transformation, and issues that arise in interleaved acquisitions, such as intersecting and variable shape trajectories, were not addressed. While the formalism introduced by Soumekh leads to a more accurate DCF, the expression described more recently in ref. 2 is currently prevalent in the spiral MRI literature.

In this paper the problem of density compensation is revisited in the context of interleaved spiral sampling, and we derive an analytic DCF that permits accurate

MRM 38:117–128 (1997)

From the McConnell Brain Imaging Centre, Montreal Neurological Institute, McGill University, Montreal, Quebec, Canada.

Address correspondence to: Richard Hoge, Ph.D., Room WB320, McConnell Brain Imaging Centre, Montreal Neurological Institute, 3801 University Street, Montreal, Quebec H3A 2B4, Canada.

Received November 12, 1996; revised January 13, 1997; accepted January 15, 1997.

This work was supported by the Medical Research Council of Canada and the National Institute of Mental Health.

0740-3194/97 $3.00

image reconstruction even in the presence of complex fluctuations in k-space sampling density. This function is equivalent to the absolute value of the determinant of the Jacobian matrix for the transformation between Cartesian coordinates and the spiral sampling parameters of time and interleaf rotation angle (19). We also examine the implications of nonideal conditions, such as the intersection of adjacent spiral interleaves, and variations in trajectory shape with the interleaf rotation angle.

We then compare the results of simulated spiral sampling and image reconstruction using the Jacobian determinant and other previously published expressions. Simulated acquisitions are used exclusively in this study, as they permit the effects of the sampling trajectory and DCF to be examined in isolation, eliminating other instrumental factors such as spatially dependent shifts in resonant frequency. The simulations incorporate trapezoidal and distorted gradient waveforms, as well as more ideal ones, and significant improvements in reconstruction accuracy are demonstrated when the Jacobian determinant is used.

THEORY

In this section we introduce a generalized parameterization of the inverse Fourier transform integral, emphasizing the role of the Jacobian determinant as a density compensation function. This concept is illustrated using the example of integration in polar coordinates, which is then extended to yield a simple and general reconstruction filter for interleaved spiral MRI. Various nonideal situations are considered, and alternate density compensation expressions from the literature are reviewed.

Reparameterization of the Fourier Integral

The reconstruction of a two-dimensional image from its Fourier transform can be expressed as the following double integral:

$$\begin{aligned} I(\vec{x}) &= \iint_K F(\vec{k}) e^{2\pi i(\vec{k}\cdot\vec{x})} dA \\ &= \iint_K G(\vec{k};\vec{x}) dA \end{aligned} \quad [1]$$

where $I(\vec{x})$ is the complex image intensity at $\vec{x}$, $F(\vec{k})$ is the Fourier transform of $I(\vec{x})$ evaluated at $\vec{k}$, and the factor dA represents the differential area element around the point $\vec{k}$ in the Cartesian k-space plane. The integrand will henceforth be written as $G(\vec{k};\vec{x})$ for clarity.

Consider a differentiable coordinate transformation T given by $\vec{k} = T(\vec{u})$ where the coordinates of $\vec{k}$ and $\vec{u}$ are (k_x, k_y) and (u, v), respectively. According to the change of variables theorem of integral calculus, Eq. [1] can be rewritten as

$$I(\vec{x}) = \iint_{T^{-1}(K)} G(k_x(\vec{u}),k_y(\vec{u});\vec{x}) \left|\frac{\partial(k_x,k_y)}{\partial(u,v)}\right| du\ dv \quad [2]$$

where $|\partial(k_x, k_y)/\partial(u, v)|$ is the absolute value of the determinant of the Jacobian matrix for the transformation T. In the remainder of this discussion, it will be assumed that references to the Jacobian determinant in the context of integration or density compensation imply its absolute value unless otherwise indicated. This term is required because the area, in the Cartesian plane, of the differential area element dA encompassed by small displacements $T(du, 0)$ and $T(0, dv)$ is given by

$$dA = \left|\frac{\partial(k_x,k_y)}{\partial(u,v)}\right| du\ dv \quad [3]$$

The Jacobian determinant is therefore proportional to the area in the Cartesian plane surrounding points which are uniformly spaced in the (u, v) plane. It is then *inversely* proportional to the *density* of such points in the Cartesian plane, and hence appropriately considered a density compensation function. The concepts discussed in this paper are equally relevant for sampling and integration in three or more dimensions with the area element, dA, replaced by a generalized volume element.

The above reformulation is useful, because u and v can represent parameters of an imaging system that are varied in uniform increments to scan through the k-space domain of interest. In a projection imaging scheme, for example, u and v correspond to the k-space radius ρ and polar angle θ, respectively. This results in the following form of the integral:

$$\begin{aligned} I(\vec{x}) &= \iint_{K_p} G_c(\rho\cos(\theta),\rho\sin(\theta);\vec{x}) \left|\frac{\partial(k_x,k_y)}{\partial(\rho,\theta)}\right| d\rho\ d\theta \\ &= \iint_{K_p} G_p(\rho,\theta;\vec{x})\rho\ d\rho\ d\theta \end{aligned} \quad [4]$$

where G_c and G_p represent, respectively, the Cartesian and polar parameterizations of the function $G(\vec{k};\vec{x})$, and the domain of integration, K_p, is expressed in polar coordinates. The above formulation leads to the well known result that $dA = \rho\ d\rho\ d\theta$ for integration over a two-dimensional domain in polar coordinates. This is the basis for the Rho filter employed in filtered backprojection of radially sampled data (20), and the reparameterization can be extended to derive a more general density compensation term for interleaved spiral sampling.

Interleaved spiral MRI is performed by repeatedly scanning the 2D Fourier transform of an object along a spiral trajectory following successive rotations of the trajectory about the origin. In this way, any point in the 2D k-space plane can be examined by sampling at the appropriate point along the spiral after it has been rotated through a suitable angle. We will assume initially that the shape of the spiral trajectory, $\vec{k}(t)$, does not vary for different interleaves and that its radial component, $|\vec{k}(t)|$, increases monotonically with time (cases where these assumptions are not true will be examined later in this section). Under these assumptions, the polar k-space coordinates of a sample acquired at time t on a spiral trajectory $\vec{k}(t)$ rotated by an angle β are given by the transformation

$$\begin{aligned} \rho(t) &= |\vec{k}(t)| \\ \theta(t,\beta) &= \arg(\vec{k}(t)) + \beta \end{aligned} \quad [5]$$

where $|\vec{k}(t)|$ and $\arg(\vec{k}(t))$ are used to denote the Cartesian magnitude and polar angle of $\vec{k}(t)$, respectively. We can now rewrite Eq. [4] with t and β as the variables of integration:

$$I(\vec{x}) = \int\int_{K_s} G_s(t,\beta;\vec{x})\rho(t)\left|\frac{\partial(\rho,\theta)}{\partial(t,\beta)}\right| dt\, d\beta \quad [6]$$

where G_s indicates the spiral parameterization of the function G, and K_s is the integration domain in spiral coordinates.

The assumptions made above allow the Jacobian determinant for the transformation from spiral to polar coordinates to be written in simple form:

$$\begin{aligned} \left|\frac{\partial(\rho,\theta)}{\partial(t,\beta)}\right| &= \begin{vmatrix} \frac{\partial\rho}{\partial t} & \frac{\partial\rho}{\partial\beta} \\ \frac{\partial\theta}{\partial t} & \frac{\partial\theta}{\partial\beta} \end{vmatrix} = \begin{vmatrix} |\vec{k}'(t)|\cos(\vec{k}'(t),\vec{k}(t)) & 0 \\ \frac{|\vec{k}'(t)|}{|\vec{k}(t)|}\sin(\vec{k}'(t),\vec{k}(t)) & 1 \end{vmatrix} \\ &= |\vec{k}'(t)| \cdot |\cos(\vec{k}'(t),\vec{k}(t))| \end{aligned} \quad [7]$$

where $\cos(\vec{k}'(t), \vec{k}(t))$ or $\sin(\vec{k}'(t), \vec{k}(t))$ is used to indicate the cosine or sine, respectively, of the angle between $\vec{k}(t)$ and the k-space velocity vector, $\vec{k}'(t)$. Where the delimiters $|\cdot|$ enclose a matrix, the absolute value of its determinant is indicated.

The Jacobian determinant for the transformation from spiral to Cartesian coordinates can then be written as

$$\begin{aligned} \left|\frac{\partial(k_x,k_y)}{\partial(t,\beta)}\right| &= |\vec{k}(t)| \cdot |\vec{k}'(t)| \cdot |\cos(\vec{k}'(t),\vec{k}(t))| \\ &= \frac{\gamma}{2\pi}|\vec{k}(t)| \cdot |\vec{g}(t)| \cdot |\cos(\vec{g}(t),\vec{k}(t))| \end{aligned} \quad [8]$$

where $\vec{g}(t)$ is the gradient waveform vector (g_x, g_y) and γ is the gyromagnetic ratio of the relevant nucleus. Note that, under the assumed conditions of radial symmetry and monotonicity, only the *radial* velocity, $\partial\rho/\partial t$, affects the sampling density; there is no dependence on angular velocity. Segments of interleaved spiral trajectories with very low angular velocity, which appear to be radial or nearly radial, indeed coincide with an apparent decrease in the angular sampling density, as shown in Fig. 1. Insufficient angular sampling density can lead to aliasing, but it does not otherwise affect the point-spread function associated with the acquisition. The aliasing effect is not corrigible by deconvolution, so the DCF, which is more properly described as a reconstruction filter, need not reflect sampling density variations of this nature. Note that if the sampling trajectories are directed radially at a constant velocity, then Eq. [8], which we will refer to as the *simplified Jacobian determinant* or SJD, reduces, appropriately, to the Rho filter.

The reparameterized Fourier integral can now be written as

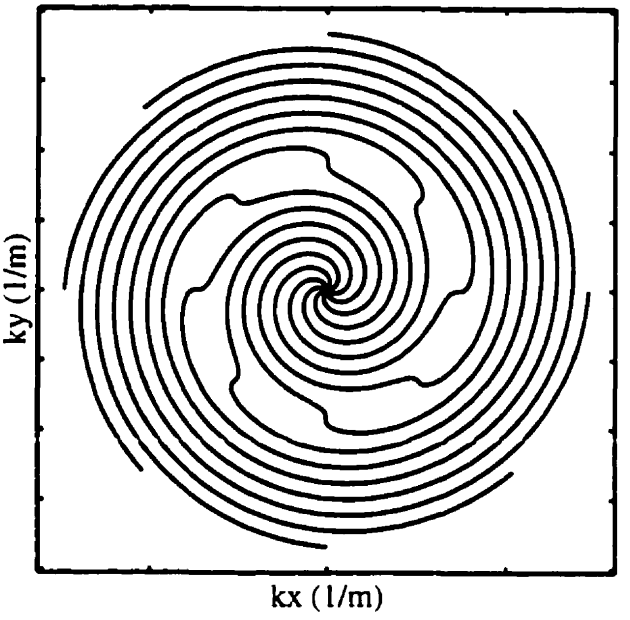

FIG. 1. Interleaved spiral trajectories with constant radial velocity but which include a segment of low angular velocity. The resulting band of low angular sampling density increases the number of interleaves required to avoid aliasing but does not affect the Jacobian determinant for the spiral-Cartesian transformation, which in this case (constant radial velocity) is identical to the Rho filter.

$$I(\vec{x}) = \frac{\gamma}{2\pi}\int\int_{K_s} F_s(t,\beta)e^{2\pi i(\vec{k}(t,\beta)\cdot\vec{x})}|\vec{k}(t)| \cdot |\vec{g}(t)| \cdot |\cos(\vec{k}'(t),\vec{k}(t))|dt\, d\beta \quad [9]$$

For spiral MRI using a gradient waveform $\vec{g}(t)$ repeated over N interleaves, Eq. [9] may be approximated by the following double summation:

$$I(\vec{x}) \approx \left(\frac{\gamma\Delta t}{2\pi N}\right)\sum_{m=1}^{M}\sum_{n=1}^{N} F_{mn}e^{2\pi i(\vec{k}_{mn}\cdot\vec{x})}D_m \quad [10]$$

where

$$D_m = |\vec{k}_m| \cdot |\vec{g}_m| \cdot |\cos(\vec{g}_m,\vec{k}_m)| \quad [11]$$

In the above expression, Δt is the temporal sampling interval, M is the number of samples per interleaf, F is the $M \times N$ matrix of samples, and D_m is the value of Eq. [8] at the mth time point along an arbitrary interleaf. If the spiral trajectory undergoes abrupt changes in direction, we have found the following discrete form of the SJD to be more accurate:

$$D_m = \begin{cases} 0 & \text{if } m = 1 \\ |\vec{k}_m| \cdot ||\vec{k}_m| - |\vec{k}_{m-1}|| & \text{for } m > 1 \end{cases} \quad [12]$$

where the delimiters $|\cdot|$ indicate the Cartesian magnitude of the enclosed vector or the absolute value of a scalar argument.

Fourier Inversion Using Gridding

Equation [10] represents the reconstruction of an image by direct summation of its nonuniformly sampled Fourier components, a method that is rarely used due to its high computational cost. A more common approach is to interpolate the nonuniform samples onto a Cartesian grid (i.e., gridding) and take advantage of the FFT algorithm. The gridding method described by Jackson *et al.* (7) is based on the following series of operations:

$$F_{SCS} = ((F \cdot S_s) * C) \cdot S_c \qquad [13]$$

where F_{SCS} denotes the gridded data, F is the object's Fourier transform, S_s is an array of two-dimensional delta functions representing the spiral sampling distribution, C is the gridding kernel, and S_c represents the uniformly spaced Cartesian grid. The above operations lead to an image intensity distribution I_{SCS}, which can be represented as

$$I_{SCS} = ((I * s_s) \cdot c) * s_c \qquad [14]$$

where I is the desired image (the inverse Fourier transform of F), and s_s, c, and s_c are the inverse Fourier transforms of S_s, C, and S_c, respectively. The multiplication by c in Eq. [14] can be corrected by performing the appropriate division in the spatial domain, as described in ref. 7, but the image blurring by s_s must be removed by multiplicative filtering in the spatial frequency domain. Jackson suggests dividing Eq. [13] by $(S * C)$, which he calls the *area density function*, to correct for blurring by s_s. However, as s_s is the impulse response function associated with spiral sampling, it can be computed by setting $F_s(t, \beta)$ in Eq. [9] equal to an array of 2D delta functions, representing the locations of the spiral samples in the (t, β) plane, divided by Eq. [8]. This array of weighted delta functions is the spiral parameterization of the transfer function S_s. Equation [11] therefore provides the appropriate spiral sample weighting factors to remove blurring of the image by s_s in gridding.

Non-Ideal Conditions

Equations [7] through [12] were obtained by assuming that the shape of the unrotated spiral trajectory does not vary in rotated interleaves, and that its radial component increases monotonically with time. Here we examine the consequences of violating these assumptions, and the implications of the above theory for single-shot spiral acquisition.

Intersecting Trajectories

The theory described thus far pertains to interleaved spirals in which two copies of the trajectory, rotated by an arbitrarily small angle, intersect or coincide only at the origin. Some spiral trajectories may not behave in this way; they may instead give rise to adjacent interleaves that cross at one or more points in addition to the origin. For this to occur, the radial velocity of the trajectories must be equal to, and possibly less than, zero over some interval. This velocity component occurs as a factor in the Jacobian determinant for spiral sampling, which must therefore also pass through zero and possibly change sign at some point, indicating the non-invertibility of the spiral-Cartesian transformation over such regions. The effects of convergent spiral interleaves on the SJD are illustrated in Fig. 2, and the implications for density compensation strategies are discussed below.

First we will consider intervals on which the radial velocity of the trajectory is zero. The commensurate Jacobian determinant, also zero, reflects the theoretically infinite sampling density that results from the mapping of multiple rotation angles onto a single point in the Cartesian plane. In a continuous implementation of the Fourier integral, such degeneracy does not prevent the corresponding frequency components from appearing appropriately in the result because arbitrarily close frequencies contribute with (arbitrarily) high density and non-zero Jacobian determinant values. This is not true of discrete implementations, in which the ensemble of frequencies sampled *around* a point of degeneracy must serve as an approximation to the excluded frequency. This results in an error that becomes more apparent as the sampling interval is increased. The high temporal sampling rates typically employed in spiral MRI result in considerable tolerance for such convergence and the resultant errors are minimal if accurate density compensation is performed.

An analogous condition, not associated with the radial velocity, invariably exists at the origin where all trajectories converge. Intensity cupping artifacts and DC errors in images formed using radial or spiral sampling distributions stem from this degeneracy of the polar-Cartesian transformation, and are attenuated by decreasing the radial or, in the case of spirals temporal, sampling interval.

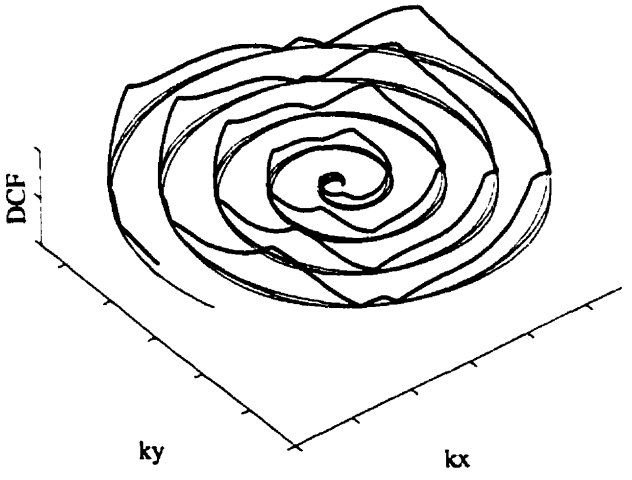

FIG. 2. Jacobian determinant for intersecting spiral trajectories. Three adjacent spiral interleaves are shown plotted in the (k_x, k_y) plane, and the Jacobian determinant that corresponds to the middle trajectory is plotted as a heavier, fourth line whose height above the (k_x, k_y) plane is proportional to the DCF value. It can be seen that the Jacobian determinant goes to zero where the adjacent interleaves intersect. The short, positive segments of the Jacobian determinant between zero crossings correspond to trajectory segments with a slightly negative radial velocity. They are positive because the DCF is defined here as the absolute value of the Jacobian determinant. The trajectories were generated using the trapezoidal gradient waveforms shown in Fig. 4j.

The DCF also plays a role in determining the prominence of these artifacts.

Segments of the trajectory with a *negative* radial velocity are more problematic from a mathematical standpoint. These represent truly retrograde progressions of the spiral path back towards the origin and, unlike the factor of zero observed in the previous case, the value of the Jacobian determinant obtained during such excursions leads to inaccuracies in continuous integration as well as in discrete summation. The simplest approach to accurate density compensation around retrograde portions of a trajectory, which constitute superfluous coverage of k-space, is to set the sample weighting factors to zero along the redundant segments, as shown schematically in Fig. 3. A strength of purely numerical density estimation methods is that they generally do not depend on invertibility of the sampling transformation.

Variable Trajectory Shape

In some cases the shape of a trajectory will vary as it is rotated about the origin, due to static field inhomogeneities, variable eddy-current effects, and imbalance between gradient amplifier channels. If there is significant warping of the intended circularly symmetric sampling distribution, it may be necessary to compute the full Jacobian determinant, or FJD, for the spiral-Cartesian transformation by numerically evaluating the partial derivatives of k_x and k_y with respect to t and β:

$$\mathrm{FJD} = \begin{vmatrix} \dfrac{\partial k_x}{\partial t} & \dfrac{\partial k_x}{\partial \beta} \\ \dfrac{\partial k_y}{\partial t} & \dfrac{\partial k_y}{\partial \beta} \end{vmatrix} \qquad [15]$$

This expression can be approximated from discretely sampled trajectories, with minimal computational load, using finite differences. The DCF obtained when the FJD is calculated for a sampling distribution with constant trajectory shape is virtually identical to that obtained using the SJD.

An alternative approach is to view the warping as a transformation T_w applied to an underlying radially symmetric sampling distribution. The appropriate density compensation function is then the product of the Jacobian determinants of T_w and the symmetric spiral-Cartesian transformation. If the Jacobian determinant of T_w is a slowly varying function of position in k-space, then its contribution to blurring in the spatial domain will be negligible and the density compensation function can be based solely on the unwarped trajectories. This is likely to be the case when T_w is primarily due to field inhomogeneities or imbalance between gradient channels, leading to the surprising result that the *undistorted* trajectories constitute more appropriate input to Eq. [11] in such cases. For example, distortion that compressed a radially symmetric sampling distribution by one half along the k_y axis would result in a *uniform* increase in sampling density over the k-space domain, by a factor of two, which could be completely neglected. Rather than computing the DCF based on the distorted trajectories, one would compute it based on the original ones. Note that although a compression of this sort would result in significant portions of the trajectory with negative radial velocity, these would not necessarily lead to degeneracy of the sampling transformation, because of the elliptical, rather than circular, symmetry of the distribution.

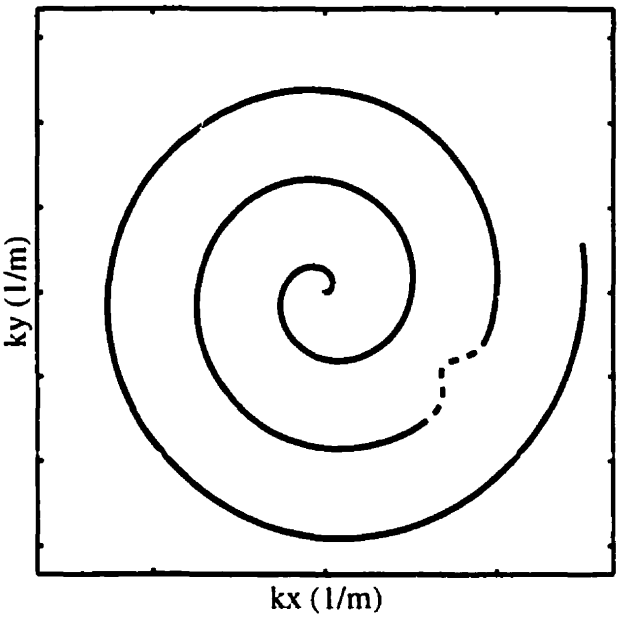

FIG. 3. Radially redundant segment of a spiral trajectory. The dashed portion of the trajectory shown above represents a segment that must be removed to restore invertibility to the spiral-Cartesian sampling transformation. This can be accomplished by setting the DCF to zero over the indicated region.

Single Shot Trajectories

We have assumed thus far that interleaved spiral sampling is performed. Single-shot spiral sampling is also a potentially important mode of acquisition, and it is worth examining whether Eq. [11] is applicable as a DCF in this case.

A spiral trajectory which completes m turns will cross an arbitrary axis through the origin 2 m times. If n interleaves are performed, the number of crossings increases to 2 mn. For a given spiral trajectory shape which reaches a maximum k-space radius k_{max}, n is generally chosen such that

$$n \geq \frac{\mathrm{FOV}}{m \cdot k_{max}} \qquad [16]$$

where FOV is the desired field of view.

Inspection of Eq. [11] reveals that the Jacobian determinant of the spiral to Cartesian transformation depends only on the radial velocity component of the spiral trajectory. Equation [16] can therefore be satisfied by decreasing n while increasing the angular velocity, without changing the radial distribution of sampling density. In single-shot spiral acquisition this is performed by setting n equal to one and the suitability of Eq. [11] for density compensation is not affected.

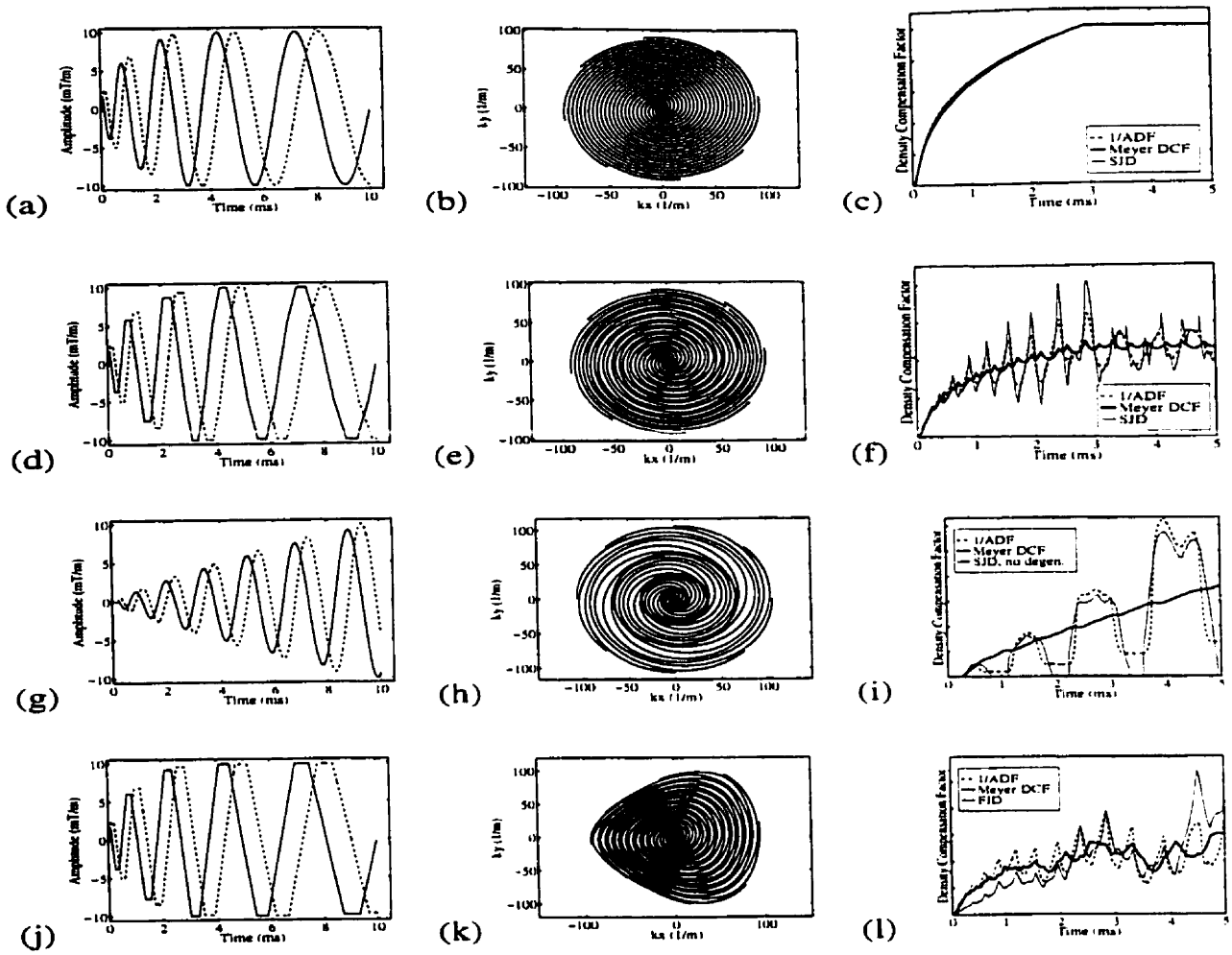

FIG. 4. Gradient waveforms, *k*-space trajectories, and DCFs used in simulations. (a–c) Sinusoidal gradient waveforms, corresponding interleaved trajectories, and DCFs, respectively. (d–f) Sixteen-point trapezoidal gradient waveforms, interleaved trajectories, and DCFs. (g–i) Measured gradient waveforms, interleaved trajectories, and DCFs. (j–l) Twelve-point trapezoidal gradient waveforms before distortion, interleaved trajectories following distortion, DCFs for first (distorted) interleaf. Solid (—) and dashed (····) lines in gradient waveform plots represent the g_x and g_y channels, respectively. For clarity, only the central portions of 8 of the 20 interleaves actually used are shown in the *k*-space trajectory plots.

Alternate Density Compensation Functions

Equation [11] is different from other density compensation expressions that we have examined for interleaved spiral sampling. Meyer *et al.* have described a function of the following form (2):

$$D_2(t) = |\tilde{g}(t)| \cdot |\sin(\tilde{k}'(t), \tilde{k}(t))| \qquad [17]$$

Note that this expression is the product of the radial coordinate of a trajectory and its *angular* velocity, whereas the SJD is the product of the radial coordinate and radial velocity. For an expression to be suitable for use as a general DCF, it should be equivalent to the Rho filter when applied to a radial sampling distribution. Equation [17] does not exhibit this property.

Spielman *et al.* have used the following approximation for sampling density (14):

$$\text{sampling density} \approx \frac{\theta'(t)}{\rho'(t)} \qquad [18]$$

$$= \frac{1}{D_3(t)} \qquad [19]$$

where $\rho(t)$ and $\theta(t)$ are the polar *k*-space coordinates of the spiral trajectory at time *t*. The corresponding DCF, $D_3(t)$, is equivalent to Eq. [11] if the angular velocity is constant, but otherwise it includes an additional, variable, factor of $\theta'(t)$. Due to its dependence on angular velocity, Eq. [18] is related to the relative number of interleaves needed with a given trajectory, and was used, effectively, to estimate interleaving requirements in (14). Nevertheless, the function $D_3(t)$ fails to approach the Rho filter in the case of radial sampling, becoming infinite instead, and is therefore not suitable for use as a general density compensation function.

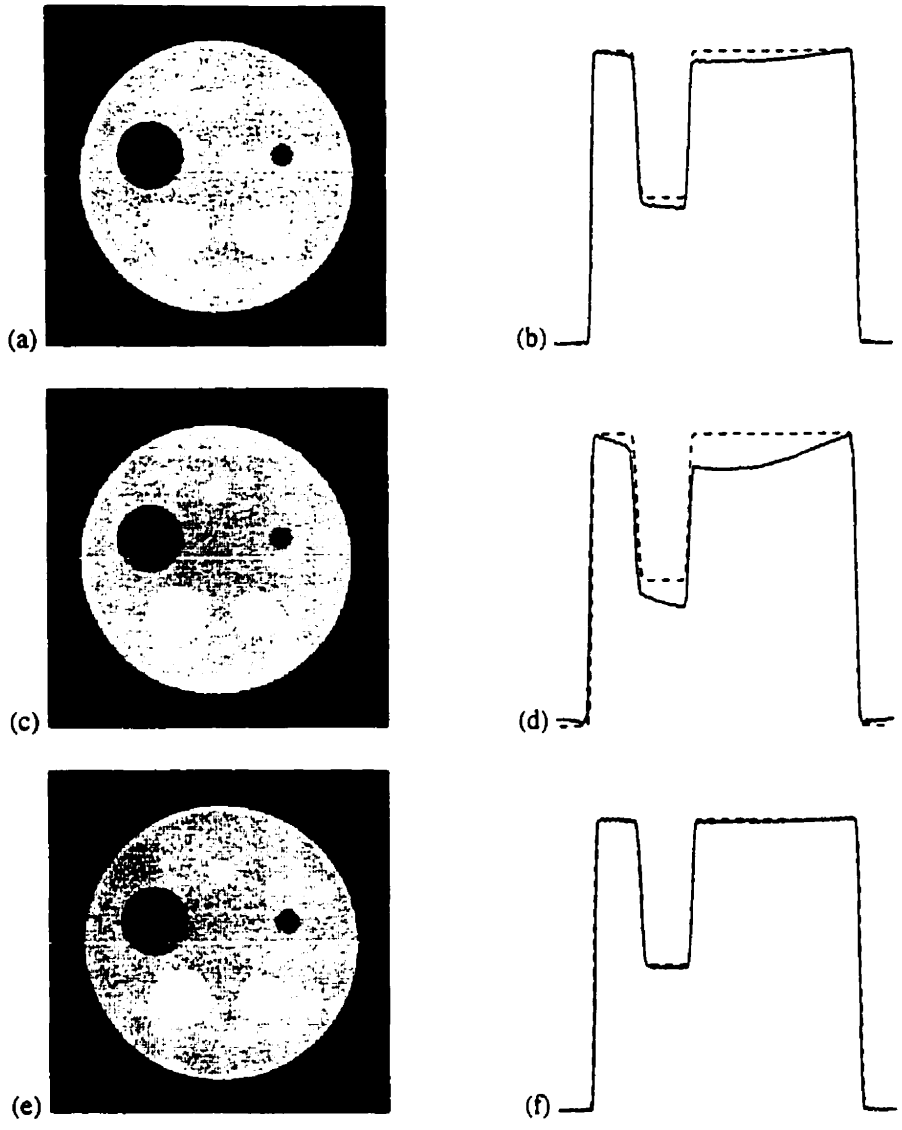

FIG. 5. Images and intensity profiles from simulations using sinusoidal gradient waveforms and different DCFs. (a, b) Density compensation function of Meyer *et al.* (c, d) Reciprocal of ADF. (e, f) Simplified Jacobian determinant. All images are windowed to show full range of intensity values. Dashed white lines on images indicate path of intensity profiles, dashed lines on profiles represent ideal contour, solid profile lines are simulation result.

In their paper on gridding reconstruction (7), Jackson *et al.* introduced the area density function, or ADF. This function was defined as the convolution of the gridding kernel C with the spiral sampling distribution S_s. The reciprocal of the ADF can be evaluated at all of the points along an interleaf to give the following density compensation function:

$$D_A(t) = \frac{S_s}{(S_s * C)} \qquad [20]$$

This non-Cartesian convolution must be evaluated numerically, at significantly greater computational expense than the other, analytic, expressions. It can be shown that, as the temporal and angular sampling intervals are decreased, $D_A(t)$ approaches the Jacobian determinant of the spiral-Cartesian transformation convolved with the kernel C. Use of a narrower kernel and smaller sampling increments in S_s would therefore result in more accurate density compensation. In the case of radial sampling, $D_A(t)$ is equal to the Rho filter convolved with C. Unlike the other expressions mentioned here, the shape of the area density function depends on the number of interleaves used, a property that is not desirable in DCFs employed as reconstruction filters.

METHOD

Spiral data acquisition was simulated using a numerical phantom for which the Fourier transform could be evaluated analytically at points lying on a given set of interleaved spiral trajectories. The phantom consisted of a set of discs of different radii and intensities superimposed and then smoothed with a Gaussian kernel. An analytic expression for the Fourier transform of the phantom was derived, based on the positions, radii, and intensities of the different discs, as well as the characteristics of the Gaussian smoothing kernel. This approach was chosen to avoid problems of sampling a non-analytic phantom along arbitrary trajectories. The slight Gaussian smoothing was included to suppress ringing artifacts associated with the finite sampling extent in k-space. We do not consider windowing functions, which can be applied as a second multiplicative filter, and have been described elsewhere (21). Image reconstruction was performed by gridding and fast-Fourier inversion as described in ref. 7 using the ADF reciprocal (Eq. [20]), and also with the DCF of Meyer *et al.* (Eq. [17]), the SJD (Eq. [11]), and the FJD (Eq. [15]).

Acquisition and reconstruction parameters used in the simulations were as follows: Twenty spiral interleaves of 2048 samples each were used to generate the images shown below. The maximum k-space radius of all trajectories was 210 m^{-1}, supporting a nominal resolution of 2.4 mm. The spiral samples were interpolated onto a 256 × 256 Cartesian k-space grid with a spacing of 1.95m^{-1}, reflecting a 512-mm field of view in the spatial domain. The desired field of view was actually 256 mm (the radius of the analytical phantom being slightly less than this), and the factor of two oversampling in the spatial frequency domain was performed to reduce the

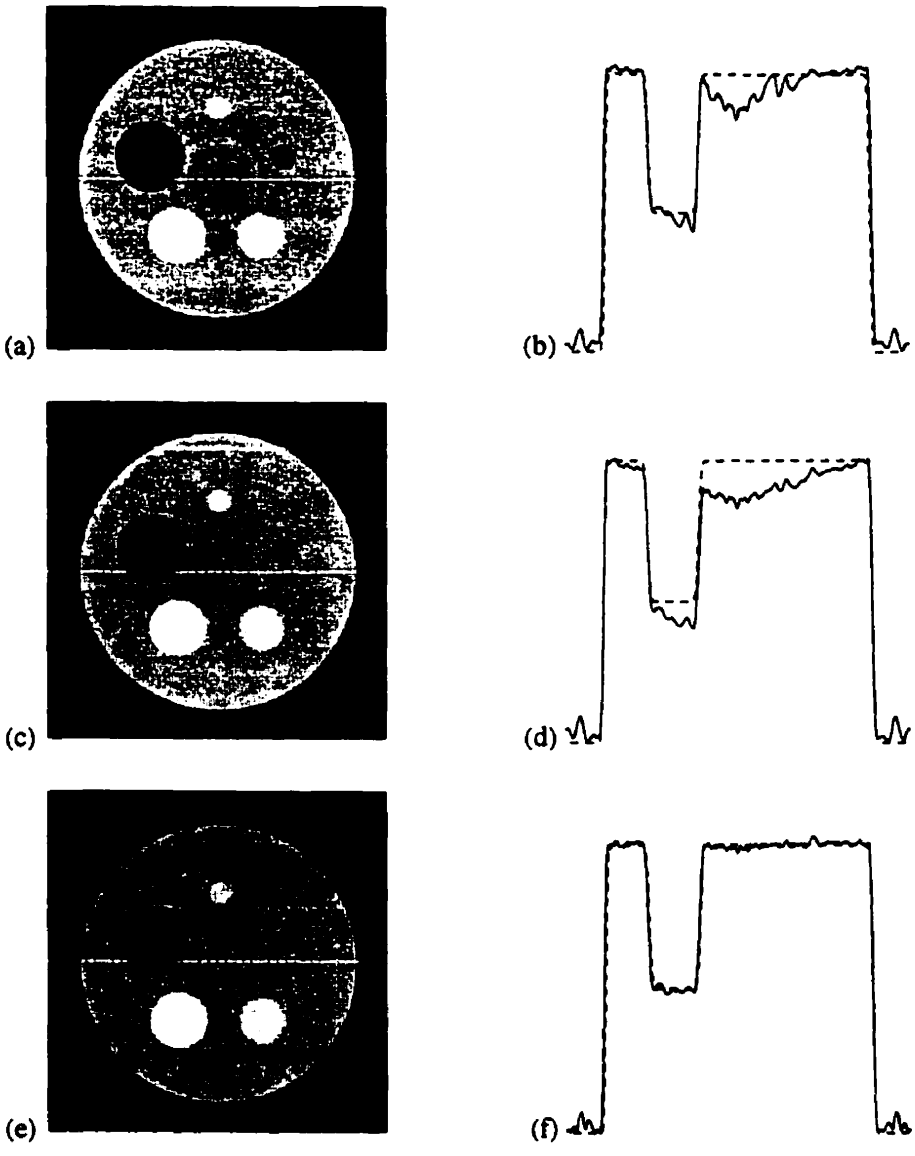

FIG. 6. Images and intensity profiles from simulations using sixteen-point trapezoidal gradient waveforms, constant trajectory shape, and different DCFs. (a, b) Density compensation function of Meyer *et al.* (c, d) Reciprocal of the area density function. (e, f) Simplified Jacobian determinant.

aliasing contribution from the convolution kernel used in gridding, a Kaiser-Bessel kernel with the parameters described as optimal in ref. 7. Following FFT inversion of the gridded data, the outer portions of the field of view were discarded and the resultant 128 × 128 complex matrices were displayed as modulus images.

Four sets of sampling conditions were employed. First, we tested the different density compensation functions under ideal conditions. Sinusoidal gradient waveforms (Fig. 4a) optimized to give a constant linear velocity spiral trajectory to within the amplitude and slew rate constraints of a typical MRI system were used in these experiments, resulting in a relatively uniform, smoothly varying sampling density distribution (Fig. 4b).

In the second series of DCF comparisons, sixteen-point trapezoidal approximations to the sinusoidal waveforms described above were used (Fig. 4d). The trajectory's shape was held constant over all interleaves and it had a monotonically increasing radial coordinate, but the sampling density achieved varied in a complex fashion over k-space (Fig. 4e).

In the third set of experiments, we tested the various DCFs using a measured k-space trajectory that also allowed us to evaluate the effects of intersecting trajectories. The trajectory was generated on a Philips Gyroscan S-15HP MRI scanner with unshielded gradients, and measured using the method of Takahashi and Peters (9). Distortion of the gradient waveforms, which are shown in Fig. 4g, caused neighboring interleaves to cross periodically as shown in Fig. 4h. This provided an opportunity to evaluate the strategy proposed above for dealing with non-invertible sampling transformations, and an additional reconstruction was performed in which radially redundant trajectory segments were assigned zero DCF values.

The fourth set of simulations tested the DCF's on sampling distributions consisting of intersecting spiral trajectories whose shape was variable with interleaf rotation angle. The intersecting trajectories (Fig. 2), generated using 12-point trapezoidal gradient waveforms, were distorted into a noncircularly symmetric form by applying the following transformation:

$$\begin{aligned} k_x &\rightarrow k_x \\ k_y &\rightarrow \left(\frac{k_x}{500} + 1\right) k_y \end{aligned} \qquad [21]$$

The resultant set of trajectories is shown in Fig. 4k. In these simulations, the full version of the Jacobian determinant (Eq. [15]) was employed. To test the theory that the radially symmetric trajectories, if known, constitute more appropriate input than the asymmetric ones to the SJD under such conditions, additional reconstructions were performed using the spiral trajectories both before and after distortion by the above transformation (Eq. [21]) as input to Eq. [11].

Computation times for the DCFs described here, on an SGI Challenge with a 150 MHz R4400 processor

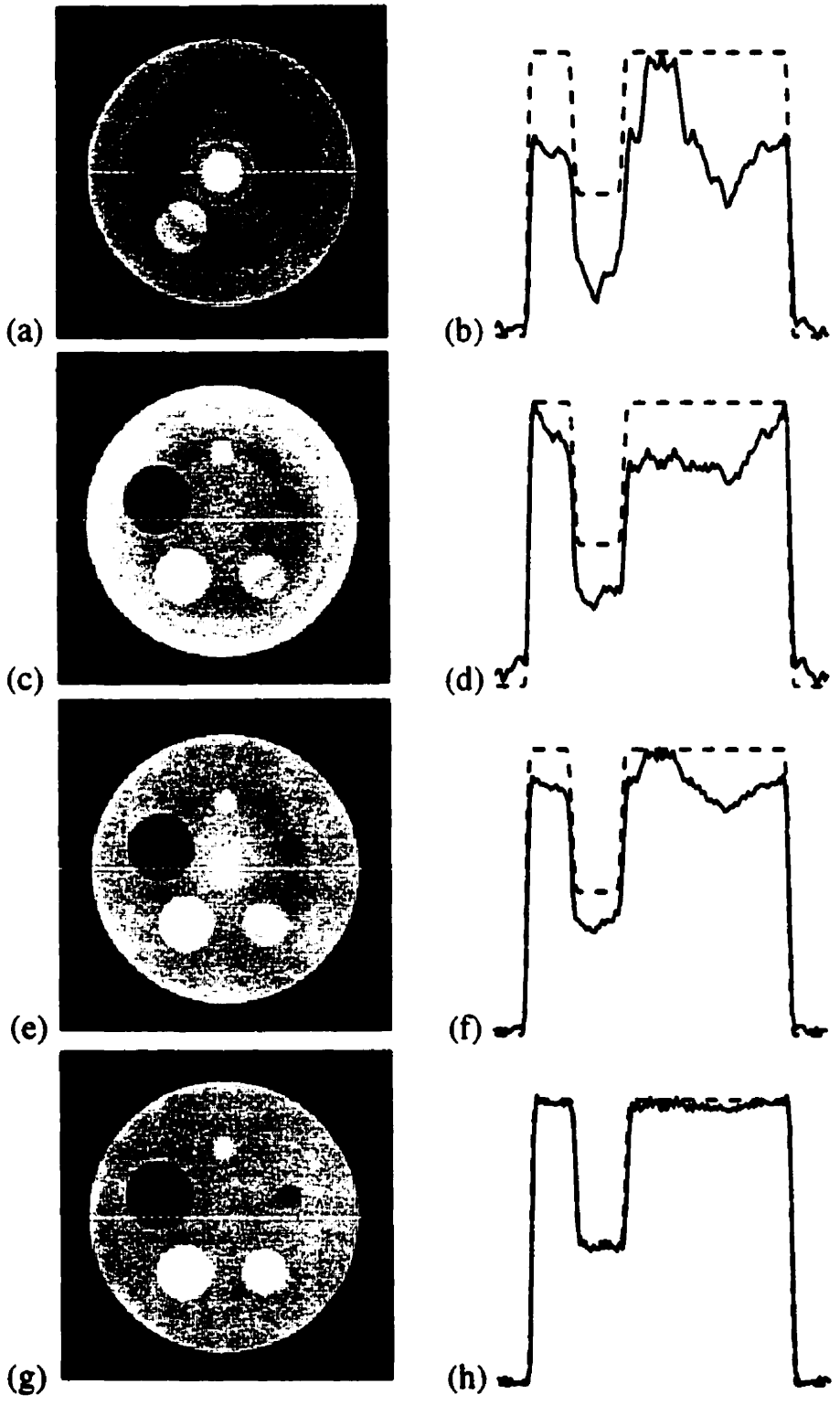

FIG. 7. Images and intensity profiles from simulations using measured gradient waveforms, constant trajectory shape, and different DCFs. (a, b) Meyer's density compensation function. (c, d) Reciprocal of the area density function. (e, f) Simplified Jacobian determinant (g, h) Simplified Jacobian determinant with degenerate trajectory segments removed.

(specfp92 = 99), ranged from less than one second for the SJD, the FJD, and Meyer's DCF, to over 10 min for the ADF reciprocal.

RESULTS AND DISCUSSION

Density Compensation Functions

Figure 4c shows density compensation functions computed for the sinusoidal gradient waveforms (Fig. 4a). The different DCFs vary smoothly and exhibit similar behavior. Meyer's DCF and the reciprocal of the ADF are virtually identical, and the Jacobian determinant deviates very little from these. For clarity, only the first half of the trajectory is represented here. The initial, increasing, portion of a given DCF represents the slew-rate limited period of the gradient waveforms. Neither Meyer's DCF nor the SJD (and the closely related ADF reciprocal) vary over the constant linear velocity portion because both the radial and angular velocities are inversely proportional to the radius in this region.

Figure 4f shows density compensation functions for the trajectories produced by the 16-point trapezoidal gradient waveforms (Fig. 4d). The Jacobian determinant and the reciprocal of the ADF reflect the striking irregularity of the sampling density achieved with these. The ADF reciprocal exhibits the low-pass filtering effect of its convolution kernel, however, and the DCF of Meyer *et al.* does not respond at all to the higher frequency, high amplitude, oscillations.

Figure 4i shows DCF's for the measured *k*-space trajectory (Fig. 4h). The crossing trajectories used in this simulation resulted in extremely large concentrations of samples around the regions of intersection, with much lower density in the intervening areas. Note that the Jacobian determinant-derived DCF has been set to zero along segments where the sampling transformation is degenerate, in particular where the radial velocity and hence the Jacobian determinant are negative. Examination of the figure reveals that signifi-

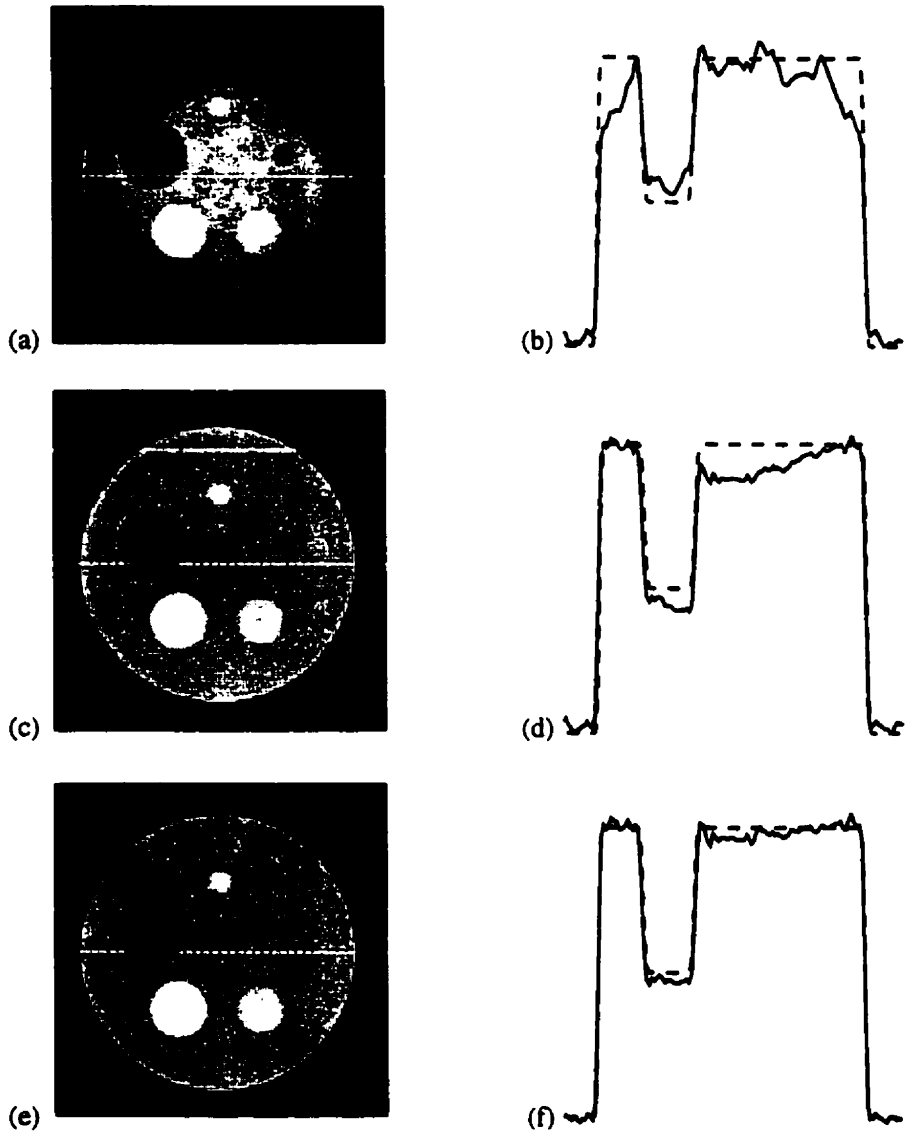

FIG. 8. Images and intensity profiles from simulations using intersecting, variable shape trajectories and different DCFs. (a, b) Meyer's DCF. (c, d) ADF reciprocal. (e, f) Full Jacobian determinant.

cant portions of the trajectory have been subjected to such exclusion. The finite sampling used to generate the ADF, and the blurring effects of the convolution kernel, prevent the corresponding DCF from responding accurately to the regions of extremely high relative sampling density that occur with this trajectory. The DCF of Meyer *et al.* again shows no response to the sharp fluctuations in sampling density, reflecting only the general trend of decreasing density at larger *k*-space radii.

Figure 4l shows DCF's for an interleaf of the distorted, variable shape trajectories (Fig. 4k). Again, the Jacobian determinant (the FJD in this case) and the reciprocal of the ADF show similar fluctuations, with differences resulting from the blurring effect of the convolution kernel on the ADF. The DCF of Meyer *et al.* seems to track the low frequency oscillations in the ADF reciprocal more closely than the Jacobian determinant does, but it does not follow the higher frequency features shared by the ADF reciprocal and the FJD. The correspondence in low frequency features between the ADF reciprocal and the Meyer DCF may reflect their sensitivity to modulations in the angular velocity, and hence the angular sampling density, of the spiral interleaves. As stated above, variations in angular sampling density should not affect the DCF, and the Jacobian determinant does not respond to these. No attempt was made to identify and remove redundant trajectory segments from the FJD here, due to difficulties introduced by the lack of circular symmetry. The degeneracy observed with these gradient waveforms was less severe than that encountered in the measured *k*-space trajectory, however, and hence more tolerable.

Images

Figure 5 shows images and corresponding intensity profiles generated by sampling the numerical phantom's Fourier transform using the sinusoidal gradient waveforms (Fig. 4a) and reconstructing with the different DCFs (Fig. 4c). Intensity nonuniformity (cupping) was observed in images reconstructed using the DCF of Meyer *et al.* and the ADF reciprocal, but this artifact was significantly reduced when the Jacobian determinant was used. Increasing the temporal sampling rate also attenuated the cupping artifact, but increasing the number of interleaves had no effect. This observation supports the hypothesis that, as a reconstruction filter, the DCF reflects only the radial, and not the angular, characteristics of the sampling distribution.

Figure 6 shows images and intensity profiles generated using the 16-point trapezoidal gradient waveforms (Fig. 4d) and the different DCFs (Fig. 4f). Ring-shaped artifacts and intensity cupping were observed when the Meyer DCF and the ADF reciprocal were employed in reconstruction. These features are presumably due to inaccurate compensation for the sharply fluctuating sampling density achieved with the trapezoidal waveforms. The artifacts were greatly diminished when the SJD was used, however.

Figure 7 shows images and intensity profiles generated using the measured *k*-space trajectory (Fig. 4h) and the

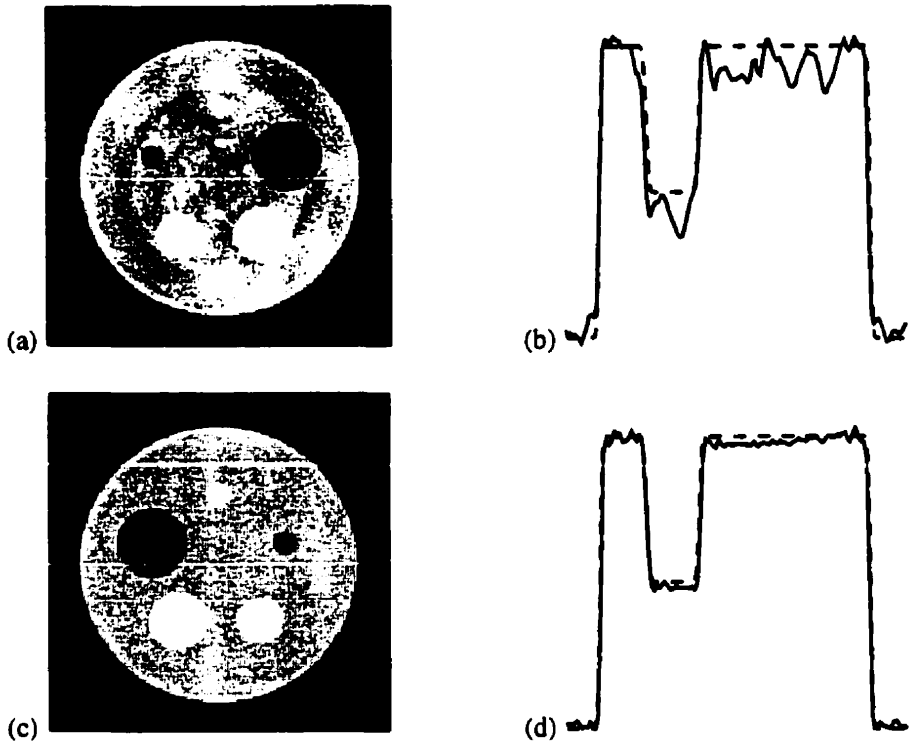

FIG. 9. Images and intensity profiles from simulations using intersecting, variable shape trajectories, and different input to the SJD. (a, b) SJD based on distorted trajectories. (c, d) SJD based on undistorted, radially symmetric, trajectories.

various DCFs (Fig. 4i). Meyer's DCF and the ADF reciprocal caused the corresponding images (Figs. 7a and 7c) to exhibit severe degradation. The image reconstructed using the simplified Jacobian determinant, and including degenerate portions of the trajectory, was more accurate than the preceding examples, but still contained artifacts (Figs. 7e and 7f). When the SJD with degenerate segments set to zero was used, these were almost completely eliminated, as shown in Figs. 7g and 7h.

Images and profiles reconstructed from samples acquired in the final set of simulations, using the intersecting, variable shape trajectories (Fig. 4k) and the corresponding DCFs (Fig. 4l), are shown in Fig. 8. When Meyer's DCF was used, the resultant image exhibited prominent artifacts near the edges of the phantom. The image produced with the ADF reciprocal did not contain any visually objectionable features, but the intensity profile shows that there is significant intensity cupping. The image reconstructed using the full Jacobian determinant contains the least artifact. Figure 9 shows images and profiles reconstructed from the same simulated data, but using the SJD derived from the spiral trajectories either before (Figs. 9a and 9b) or after (Figs. 9c and 9d) the distortion eliminated their radial symmetry. The image produced using the undistorted trajectory as input to the SJD contains relatively little artifact while its counterpart, in which the SJD was based on the distorted trajectory, is considerably worse. This is consistent with the prediction made earlier in the paper.

To verify that similar results would be obtained for phantoms consisting of noncircularly symmetric functions, all simulations were repeated with a numerical phantom identical to the one shown above but with the discs replaced by squares. The simulations were also repeated with different fields of view and resolutions, and using various numbers of interleaves and temporal sampling rates. In all cases, the trends demonstrated in the results shown above were reproduced. Substitution of the FJD for the SJD in radially symmetric sampling distributions yielded identical results. Simulations were also performed in which the discrete Fourier transform, in the form of Eq. [10], was evaluated numerically. Images reconstructed using this approach were visually indistinguishable from those reconstructed using gridding and fast Fourier inversion. Simulated thermal noise added to the complex data samples did not give rise to any notable phenomena, other than an increased noise level, in images reconstructed with the various DCFs.

CONCLUSIONS

Calculation of the Jacobian determinant for the various conditions simulated in this study revealed that surprisingly sharp variations in sampling density can occur when nonideal gradient waveforms are used. The close correspondence observed between the Jacobian determinant and the numerical ADF reciprocal, which took considerably longer to compute, confirmed that the acute fluctuations observed in the analytic function under certain conditions reflected real variations in sampling density.

We have shown that variable *k*-space sampling density results in blurring of the image by the inverse Fourier transform of the density distribution, which is generally undesirable as a point-spread function. We have also demonstrated that the Jacobian determinant for the transformation between Cartesian coordinates and the spiral sampling parameters can be used as a reconstruction filter that corrects such blurring by weighting the *k*-space samples in inverse proportion with the local sampling density. This approach can easily be extended to three-dimensional trajectories, which can be parameterized in terms of time varying spherical or cylindrical coordinates.

The gradient systems on current, commercially available, MR scanners are commonly capable of producing

arbitrary, distortion free, waveforms. We have shown that even under such ideal conditions, reconstruction accuracy is improved using the Jacobian determinant for density compensation. The simplified form of this DCF, expressed as Eq. [11], allows its efficient computation in terms of readily available sequence data, namely, the gradient and k-space trajectory waveforms.

On experimental MRI systems, and whenever the gradient hardware is pushed towards its limits, the sampling distributions achieved are likely to exhibit characteristics of the less ideal trajectories that have been investigated here. We have demonstrated that when trapezoidal or distorted gradient waveforms are used, the Jacobian determinant leads to a significant reduction in the level of artifact observed compared with the other DCFs investigated. We have also proposed an effective solution to the problem of density compensation for intersecting trajectories: the removal of redundant segments.

The full Jacobian determinant, which can be used in cases where the trajectory shape varies with interleaf rotation angle, was introduced as a DCF. The FJD gave identical results to the SJD for radially symmetric sampling distributions, and permitted accurate image reconstruction even when, in combination with intersecting trajectories, severe distortion resulted in pronounced asymmetry. If more acute trajectory crossing is combined with variable trajectory shape, however, problems may arise due to difficulties in identifying and removing degenerate trajectory segments in the absence of circular symmetry. Under such conditions the ADF reciprocal, or some other numerical DCF, may be more useful. Reducing the width of the convolution kernel used to generate the ADF will enhance the accuracy of reconstructions performed using this approach.

In addition to providing a means of generating reconstruction filters, the Jacobian determinant formalism presented in this paper is potentially useful in the design of spiral trajectories and their optimization for speed and sampling uniformity.

ACKNOWLEDGMENTS

The authors thank Atsushi Takahashi, Ph.D., for the measured k-space trajectory data, and Gérard Crelier, Ph.D., for helpful comments on the manuscript.

REFERENCES

1. C. Ahn, J. Kim, Z. Cho, High-speed spiral-scan echo planar NMR imaging—I *IEEE Trans. Med. Imaging* **MI-5**, 2–7 (1986).
2. C. H. Meyer, B. S. Hu, D. G. Nishimura, A. Macovski, Fast spiral coronary artery imaging. *Magn. Reson. Med.* **28**, 202–213 (1992).
3. G. H. Glover, A. T. Lee, Motion artifacts in fMRI: comparison of 2DFT with PR and spiral scan methods. *Magn. Reson. Med.* **33**, 624–635 (1995).
4. D. C. Noll, J. D. Cohen, C. H. Meyer, W. Schneider, "Spiral k-space MR imaging of cortical activation," *J. Magn. Reson. Imaging*, vol. 5, pp. 49–56, 1995.
5. G. B. Pike, C. H. Meyer, T. J. Brosnan, N. J. Pelc, "Magnetic resonance velocity imaging using a fast spiral phase contrast sequence," *Magn. Reson. Med.* vol. 32, pp. 476–483, 1994.
6. P. Irarrazabal, D. G. Nishimura, "Fast three dimensional magnetic resonance imaging," *Magn. Reson. Med.* vol. 33, pp. 656–662, 1995.
7. J. I. Jackson, C. H. Meyer, D. G. Nishimura, A. Macovski, "Selection of a convolution function for Fourier inversion using gridding," *IEEE Trans. Med. Imaging*, vol. 10, pp. 473–478, 1991.
8. J. O'Sullivan, A fast sinc function gridding algorithm for Fourier inversion in computer tomography. *IEEE Trans. Med. Imaging* **MI-4**, 200–207 (1985).
9. A. Takahashi, T. Peters, "Compensation of multi-dimensional selective excitation pulses using measured k-space trajectories," *Magn. Reson. Med.* vol. 34, pp. 446–456, 1995.
10. D. M. Spielman, J. M. Pauly, "Spiral imaging on a small-bore system at 4.7T," *Magn. Reson. Med.* vol. 34, pp. 580–585, 1995.
11. J. Liao, J. Pauly, N. Pelc, MR imaging using piecewise spiral trajectory. *in* "Proc., ISMRM, 4th Annual Meeting, 1996," p. 390.
12. J. G. Pipe, A. Haj-Ali, An approximation to spiral imaging using trapezoidal waveforms and collapsing spirals. *in* "Proc., ISMRM, 4th Annual Meeting, 1996," p. 391.
13. O. Heid, "Archimedian spirals with Euclidean gradient limits. *in* "Proc., ISMRM, 4th Annual Meeting, 1996," p. 114.
14. D. M. Spielman, J. M. Pauly, C. H. Meyer, "Magnetic resonance fluoroscopy using spirals with variable sampling densities," *Magn. Reson. Med.* vol. 34, pp. 388–394, 1995.
15. J. Liao, N. Pelc, "Image reconstruction of generalized spiral trajectory. *in* "Proc., ISMRM, 4th Annual Meeting, 1996," p. 359.
16. C. J. Hardy, H. E. Cline, P. A. Bottomly, "Correcting for nonuniform k-space sampling in two-dimensional NMR selective excitation," *J. Magn. Reson.* vol. 87, pp. 639–645, 1990.
17. M. Soumekh, Band-limited interpolation of unevenly spaced data. *IEEE Trans. Acoustics, Speech, Signal Processing* **36**, 110–122 (1988).
18. M. Soumekh, "Reconstruction and sampling constraints for spiral data," *IEEE Trans. Acoustics, Speech, Signal Processing*, vol. 37, pp. 882–891, 1989.
19. R. D. Hoge, R. Kwan, G. B. Pike, "Density compensation functions for Fourier inversion of data sampled along interleaved spiral trajectories. *in* "Proc., ISMRM, 4th Annual Meeting, 1996," p. 358.
20. R. Bracewell, A. Riddle, "Inversion of fan-beam scans in radio astronomy," *Astrophys. J.* vol. 150, pp. 427–434, 1967.
21. F. J. Harris, "On the use of windows for harmonic analysis with the discrete Fourier transform," *Proc. IEEE*, vol. 66, pp. 51–82, 1978.